Universidad Técnica Federico Santa María
Departamento de Ingeniería Eléctrica
Santiago, Chile

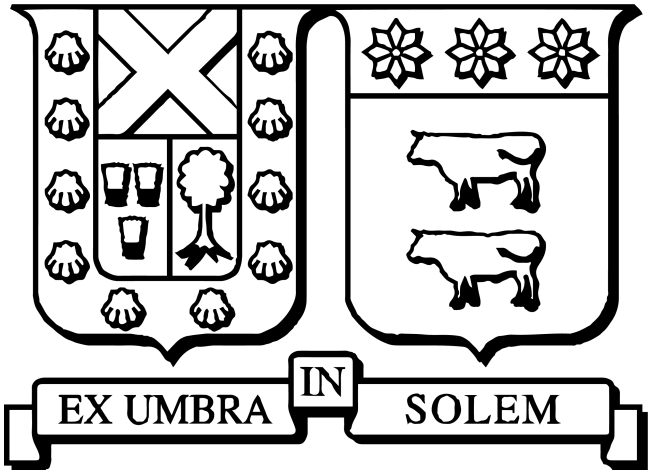

Propuesta y validación de un modelo eléctrico-térmico para módulos fotovoltaicos bifaciales bajo condiciones controladas de irradiancia y temperatura en laboratorio

VALENTINA PAZ GONZÁLEZ BECERRA
2024

Requisito parcial para obtener el título de:
Magíster en Ciencias de la Ingeniería Electrica

Profesor Guía:
Dr. Patricio Valdivia Lefort

Santiago, 30 de julio de 2024

Universidad Técnica Federico Santa María
Departamento de Ingeniería Eléctrica
Santiago, Chile

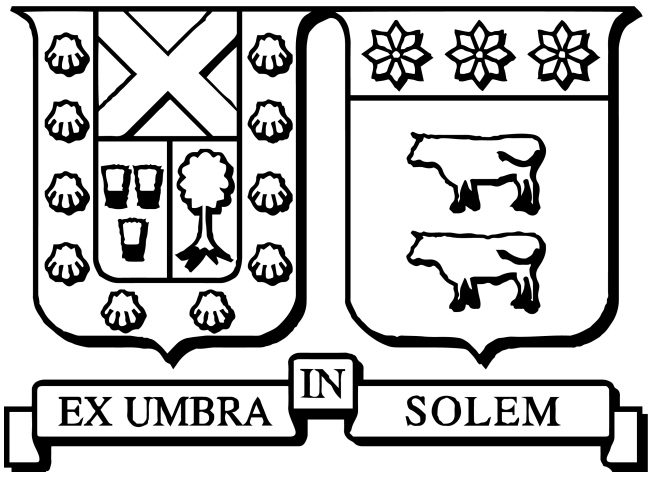

Proposal and validation of an electrical-thermal model for bifacial photovoltaic modules under controlled irradiance and temperature conditions in laboratory

VALENTINA PAZ GONZÁLEZ BECERRA
2024

Acknowledgements

I would like to extend my heartfelt gratitude to everyone who supported me, offered their companionship, and encouraged me to take on challenges. Special thanks to my family, friends, and significant one for their unwavering support.

This work was made possible through the financial support of ANID-Fondecyt-11220697 and the Scientific Research Initiation Program (PIIC) of the Universidad Técnica Federico Santa María. Thank you for enabling this research.

Contents

List of Figures

List of Tables

Abstract

Bifacial photovoltaic (bPV) modules, leveraging both front and rear irradiance, offer enhanced efficiencies over traditional monofacial modules. However, the accurate modeling and validation of bPV modules remain under-researched. This work addresses this gap by proposing a comprehensive model for bPV modules, detailing its development and validation through three key studies. The first study focuses on characterizing bPV modules, employing IV curves and diagnostic tests to assess module conditions. The second study evaluates and compares three electrical models using indoor IV curves, identifying key parameters affecting IV curve estimation. The third study introduces an electrical-thermal model, integrating a hybrid thermal model and open-access irradiance estimation software. The electrical model demonstrates strong estimation accuracy, with a percent error below 3% at the maximum power point using indoor IV curves. However, real-condition simulations reveal higher errors due to effects such as shadowing and irradiance misestimation. The findings underscore critical factors influencing bPV module performance, offering valuable insights for future research and development.

Chapter 1

General Introduction

Bifacial photovoltaic (bPV) modules represent a promising advancement in solar technology due to their ability to harness both front and rear irradiance for energy production, leading to improved efficiencies. Evaluating the potential production of bPV modules in a specific location requires careful assessment of the local ambient conditions. While numerous models have been developed and extensively studied for monofacial modules, there remains a significant gap in research concerning the accurate modeling and validation of bPV modules.

This work aims to address this gap by proposing a comprehensive model for bPV modules, detailing each step of its development and validation.

Hypothesis:

"It is possible to propose an electrical-thermal model for bifacial photovoltaic modules with greater precision regarding its scope and limitations if the data used come from high-quality measurements, such as the results obtained with the Eternalsun TCLF equipment."

And the following objectives:

- General objective: Propose an electrical-thermal model for bifacial photovoltaic modules based on fitting models found in the literature, using IV curves obtained under controlled irradiance and temperature conditions in a solar simulator.
- Specific objectives:
  - Conduct a review of the state-of-the-art regarding electrical and thermal models for bifacial photovoltaic modules.
  - Generate a baseline of IV curves for PERC+, HJT, and n-PERT bifacial photovoltaic modules under different irradiance and temperature conditions in the laboratory.
  - Evaluate the performance of bifacial photovoltaic module models from the literature and compare them with the experimental data obtained for the various modules under study.
  - Propose a model that can match the real behavior of bifacial photovoltaic modules under controlled temperature and irradiance conditions in the laboratory.
  - Compare and validate the proposed model based on controlled indoor measurements, with illumination on both sides of the module, and outdoor measurements.

Three key articles form the basis of this research:

1. **Characterization of bPV Modules**: The first article outlines the fundamentals of accurate measurement using IV curves and other diagnostic tests essential for assessing the condition of the study object. Techniques such as thermography and electroluminescence are used to categorize different kinds of images based on detected faults. IV curves are analyzed to identify different shapes that indicate various issues, operational conditions, or faults.

2. **Evaluation of Electrical Models**: The second article focuses on electrical models, where three different models are evaluated and compared using indoor IV curves. The most effective model is further analyzed to identify the parameters that most significantly impact IV curve estimation, with findings indicating that saturation current is a critical factor in the single diode model.

3. **Proposed Electrical-Thermal Model**: The third article presents an electrical-thermal model. This model estimates irradiance using open-access software and integrates a hybrid thermal model derived from two existing literature models. The electrical component of the model combines the best features of previously proposed models. The electrical model is evaluated using experimental indoor IV curves and validated with outdoor measurements under continuous monitoring. The thermal model and estimated irradiances are compared with outdoor experimental measurements. Results demonstrate a strong estimation capability for the electrical model when it is evaluated with indoor measurements, with a percent error not exceeding 3% at the maximum power point, a critical factor in production prediction. However, when all models are combined to estimate production under real conditions, various effects, such as shadowing from frames and irradiance misestimation, lead to higher estimation errors.

The proposed methodology, experimental setup, and results highlight several influential factors affecting bPV module performance, providing valuable insights for future research and development in this field. The combination of controlled indoor conditions and outdoor validation enables a clearer identification of factors affecting estimation accuracy, thereby enhancing the reliability and applicability of the proposed model.

Chapter 2

Characterization of the electrical behavior of a bifacial photovoltaic solar module obtained through static and transient analyses

Note

This article was submitted to WCPEC-8 proceedings [1], carried out in 2022.

Abstract

In the last 18 years PV solar power has increased from 0 to 500 GWp approximately as indicated by International Energy Agency Photovoltaic Power Systems Program IEA PVPS [2]. However, an issue that has been left aside is the maintenance of the constituent elements of a solar PV plant, this mainly because the elements are still under warranty. In particular, one of the fundamental players in a solar PV plant is the Photo Voltaic Solar Module PVSM, which usually has a guarantee of around 20 years. However, it has been proven that in practice a large number of modules have presented unexpected failures, e.g., power degradation faster than what the manufacturer considered when defining the warranty. Considering an average annual degradation of 1%, it would be expected that within the first 10 years, the PV modules of a PV plant present a 10% degradation in their performance. In this work it is carried out a characterization of the electrical behavior of a bifacial photovoltaic solar module obtained through static and transient analyses operating under no-fault and fault conditions at controlled conditions using the Flasher IV A+A+A+ Solar Simulator of Eternalsun. Later, the response of photovoltaic solar modules, for their healthy and faulty operation, were studied. As a result, it is obtained a characterization of the electrical behavior of bifacial photovoltaic solar module under no- fault and fault conditions at controlled level.

2.1 Introduction

The Chilean PV industry started in 2014 with a progressive insertion of Photovoltaic solar Plants, starting with 1.2%, and by 2022 there is already 20% of penetration [3]. Solar energy is one of the most promising in our country since, according to data from the Ministry of Energy, the Great North of Chile would receive the largest amount of average daily solar radiation, estimating that an area

of 20 [km^2] of photovoltaic panels could meet the energy demand of the entire country [4]. Given the conditions of desert in the great north of Chile, a technology that is especially promising is the bifacial, since it takes advantage of the radiation reflected from the ground to illuminate the rear face of the modules and thus increase the generation, making a more effervescent.

Together with the development of technology, it is necessary to create techniques that allow evaluating the performance of this, it is here where the need to generate methodologies of characterization. In the case of monofacial modules, there are a considerable number of methodologies recorded in the literature given its settlement and stability over time, since that this type of device has a long history, however, for new technologies, such as bifacials, there are more challenges associated with new behaviors that must be studied, such as their performance in different scenarios, degradation mechanisms, failures etc.

The characterization of photovoltaic modules can be carried out using different methods, among them is the characterization with electrical variables from IV curves, optical characterization, characterization by electroluminescence, among others. The present study will specifically address the characterization by means of electrical variables, electroluminescence and thermography. The characterization, in addition to providing information on the current performance of the measured device, allows detection of possible degradation or failures.

The degradation of photovoltaic modules is a problem that has been present in the industry for a long time, and understanding this process allows manufacturers to improve the materials and processes used in the production of these devices [5]. Some degradation mechanisms are mentioned in [6]:

2.1.1 Packaging material degradation

This mechanism occurs when the materials that protect the cell are damaged. Some examples of this degradation are the breakage of the glass that covers the modules (Fig. 2.1), blocking diode failure, potting discoloration (Fig. 2.2), delamination (Fig. 2.3) and cracking.

Figure 2.1: Glass breakage in a module [5]

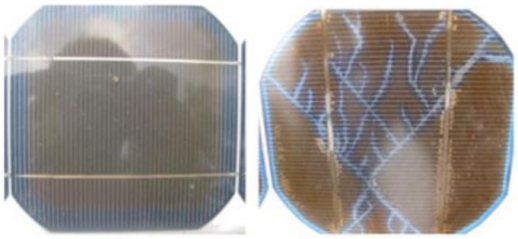

Figure 2.2: Blocking diode failure, potting discoloration [5]

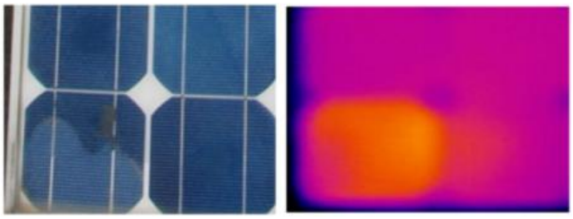

Figure 2.3: Delamination in a module (left) and infrared image of the area (right) [5]

2.1.2 Moisture intrusion

The humidity that reaches the module from the rear face or through the edges of the sheets causes corrosion (Fig. 2.4) and increases leakage currents. it attacks metallic components in the case of c-Si modules, while in modules thin film attacks the semiconductor layers, causing losses in their electrical performance.

Figure 2.4: Corrosion in interconnections and metallic contacts of two different modules [5]

In this work it is carried out a characterization of the electrical behavior of a bifacial photovoltaic solar module obtained through static and transient analyses operating under no-fault and fault conditions at controlled conditions using the Flasher IV +AAA Solar Simulator of Ethernalsun. Later, the response of photovoltaic solar modules, for their healthy and faulty operation, were studied.

2.1.3 IV curve abnormalities

The shape of the IV curves allows to identify anomalies in a photovoltaic cell. The standard IEC 62446-1 [5] contains some keys for the interpretation of the different forms that these curves can present

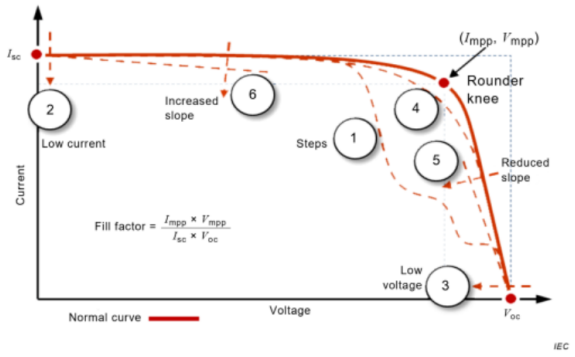

Figure 2.5: Some of the variations that IV curves can have [5]

2.1.3.a Steps or crevices

They can indicate faults between the different areas of the measured device. This deviation indicates that the blocking diode turned on, so some current is being redirected, bypassing some internal cells protected by the diode. This can occur due to partial shading, dirt or soiling of the module, damaged cells, or shorted blocking diode.

2.1.3.b Curve with low current

To identify that the current is lower than expected, the reference is rated short-circuit current. Some causes of this decrease may be uniform dirt, shadow fringing, degradation, poor sensor calibration of irradiance, measurement problems, or irradiances that are too low. 1.3. Curve with low voltage: To identify that the voltage is lower than expected, the reference is rated open circuit voltage. Some causes can be the diodes in conductor shunt or shorted, potential induced degradation (PID),significant and uniform shading throughout the cell, no correspondence with the actual temperature of the device and the value at which the curve is plotted.

2.1.3.c Curve with soft knee

Rounding of the knee of the IV curve may be a manifestation of the process module aging. This applies to curves that have changed their shape, since there are some technologies that have this form intrinsically and not necessarily corresponds to deterioration.

2.1.3.d Reduced slope in vertical leg

Corresponds to the slope that includes the section from the point of maximum power (where Vmpp is located) and the open circuit voltage (Voc). This slope is influenced by the series resistance of the module, where the higher the resistance, the lower slope incline. Some Causes of Increased Series Resistance can be damage to the wiring or faults in the interconnections of modules or substrings, which can be caused by corrosion, degradation, or factory errors. In this case, thermographic inspection can be a useful tool when it comes to identify high-resistance faults.

2.1.3.e Greater slope in horizontal leg

This variation may be related to low parallel resistances or parallel current fluxes, differences in the short-circuit current of the cells of a module or string (mismatch), shading or punctual soiling. Shunt current corresponds to deviations due to localized defects in the cell or in the interconnections, which can cause localized hot spots that can be identified through thermographic inspection.

2.2 Setup

To carry out the characterization of the bifacial photovoltaic modules, three different techniques were utilized: IV curves, electroluminescence and thermography; the equipment used for each case is detailed as follow:

2.2.1 PV Modules

The main element for the measurement is the test object, in this case two types of bifacial modules.

2.2.1.a Risen RSM72 Bifacial Modules

For the measurement, a total of 10 Risen RSM72 bifacial modules PERC+ were used, their data nominal values are presented in Table 2.1

Table 2.1: Specifications of the Risen RSM72 bifacial modules [7].

Parameter	Value
Dimensions (mm)	1984x992x25
Pmax (W)	370
Vmpp (V)	39.60
Impp (A)	9.35
Voc (V)	48.15
Isc (A)	9.90
Tolerance Isc	±3%
Tolerance Voc	±5%
Bifaciality	75%

Also, three mini bifacial modules of heterojunction technology (HJT) coming from the CEA INES laboratory were used. Its nominal data is specified in Table 2.2.

Table 2.2: Specifications of BOM CEA INES bifacial mini modules.

Parameter	BOM3-09	BOM3-09B	BOM1-16
Pmax (W)	19.216	19.047	18.990
Vmpp (V)	2.352	2.329	2.340
Impp (A)	8.172	8.179	8.117
Voc (V)	2.925	2.911	2.918
Isc (A)	8.828	8.829	8.776
FF (%)	74.42	74.12	74.15

2.2.2 IV curves: TCLF

The Temperature Controlled Lab Flasher (TCLF) solar simulator is a device developed by Eternalsun Spire, its purpose is to perform indoor characterization measurements of photovoltaic modules from IV curves, allowing measurements to be made under standard conditions STC, but also under controlled conditions of both temperature and irradiance.

Figure 2.6: Temperature Controlled Laboratory Flasher (TCLF)

The Flasher Spire measures photovoltaic modules under AM 1.5G conditions following the ASTM G173 standard [8]. Their technical specifications are found in Tables 2.3 and 2.4.

Table 2.3: TCLF General specifications.

Dimensions max. module	2140 x 13540 mm
Effective test area	2100 x 1300 mm
Classification	A+A+A+ (IEC 60904-9)

Table 2.4: TCLF light source specifications

Lamp type	SLP filtered Xenon tube
Pulse duration (ms)	110
Pulse type	Single pulse
Spectral range nm	$300 - 1200$
Spectral Match (%)	< 12.5 (A+)
Irradiance non-uniformity (%)	< 1 (A+)
STI-LTI (%)	0.10 (A+)
Irradiance range (W/m^2)	$100 - 1200$
Time between flashes (s)	< 20
Guaranteed lamp life	200000 flashes
Typical Lamp Life	> 400000 flashes

2.2.3 Electroluminiscence

The electroluminescence measurement is performed on all modules (N°1 − N°13). The maximum current supplied for RISEN RSM72 PV modules was 6 A. In the case of the mini bifacial modules, the maximum current used was lower than I_{sc} since having a transparent structure, the light emitted by the reverse reflected off the supporting wall, contaminating the measurement results; consequently, the level of current chosen to be able to appreciate in a good way the emitted spectrum, and at the same time decrease the effect of reflection was 1 A.

In both cases images captured of both, the front face and the rear face of the modules, were always preventing the connections to interfering with the measurement. From this test, only the capture of images was performed at the current level indicated previously, since in this way it was possible to obtain as much information as possible to qualitative analysis. The connection used for this test is showed in Fig. 2.7.

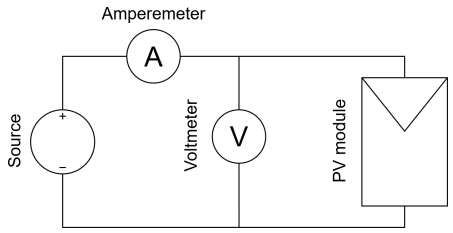

Figure 2.7: Connection circuit for the electroluminescence test.

Table 2.5: Technical specifications of the power source used for the test of electroluminescence

Brand	Ele-tech
Model	HY5020E
Dimensions (mm)	1984x992x25
P_{max} (W)	1000
Voltage (V)	0-50
Current (A)	0-20

Table 2.6: Technical specifications of the camera, lens and filter used for electroluminescence assay.

Brand	Nikon
Model	D750
Sensores (mm)	CMOS of 26 mpx.
Filtered wavelenghts (nm)	< 850

2.2.4 Thermography

The last test carried out is the capture of IR images of the modules. Are used two different connections depending on the type of module being worked on, in the case of Risen RSM72 bifacial modules, these are connected according to Fig. 2.8

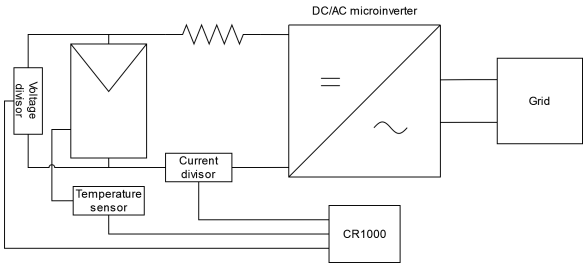

Figure 2.8: Risen RSM72 bifacial photovoltaic module connection diagram.

On the other hand, in the case of the bifacial mini modules, the PV tests were connected with a rheostats as indicated in Fig. 2.9. When connected only a mini module, the generated current was around 1 A, for this reason a connection of modules in series, to increase the voltage at the terminals. Connecting the three mini bifacial modules in series, and using the minimum resistance value of the rheostats, a current value of 97 A was obtained.

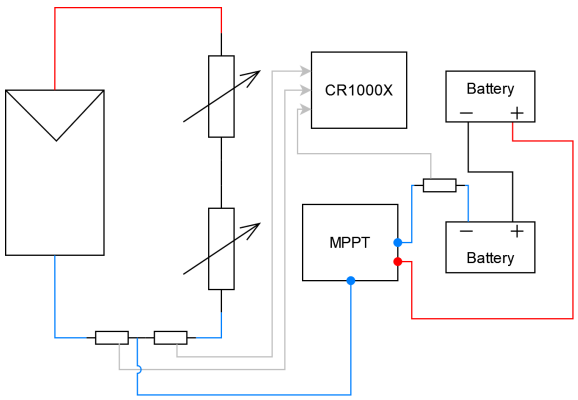

Figure 2.9: Connection diagram of the BOM CEA INES mini bifacial photovoltaic modules.

Brand	Fluke
Model	Ti400
Lens	FLK-LENS/TELE2
CDVI (mrad)	1.31
Minimal focus distance (cm)	15
Focus system	Automatic

Table 2.7: Specifications of the thermal imaging camera used for the thermography test.

2.3 Methodology

To characterize bifacial photovoltaic modules, the following tests are proposed to make: I-V curves, electroluminescence, thermography, and other such visual inspection [5].

2.3.1 IV curves

2.3.1.a Measurement at constant temperature of 25°C

After the visual inspection, the measurement of IV curves is carried out with the solar simulator TCLF. For each module, both front and back lighting are tested, using temperature correction at 25°C and varying the irradiance level from 100 to 1000 Wm^{-2}, with a step of 100 Wm^{-2} between each measurement. With the data obtained, the IV and PV curves are plotted both with illumination front and rear for irradiance levels of 100 − 500 − 1000 Wm^{-2} of all the modules that correspond to the same type, that is, the first group contains modules from 1 to 10, corresponding to Risen RSM72 bifacial modules and the second group from 11 to 13, corresponding to bifacial mini modules BOM CEA INES. From the IV curves, the data is processed to obtain:

- Graph of electrical variables (I_{sc}, V_{oc} and P_{max}) as a function of irradiance, for the front face and back surface
- Bifaciality coefficients
- BiFi, $P_{max,STC}$, $P_{max,BiF\text{-}i100}$ and $P_{max,BiF\text{-}i200}$

2.3.1.b Temperature controlled measurements

Once the IV curves corrected at 25°C have been obtained, the tests are carried out with control temperature at 25 − 50 − 75°C, and a fixed irradiance of 1000 Wm^{-2}. From the Risen RSM72 bifacial modules, modules N°1, N°8 and N°10 were chosen. From the BOM CEA INES bifacial mini modules, N°11 was chosen. With the data obtained, a graph of electrical variables (I_{sc}, V_{oc} and P_{max}) is made depending on the temperature. For module N°10, the test of both rise and fall in temperature is recorded, therefore, temperatures of 50−25°C are also added to the original points.

2.4 Results

2.4.1 IV curves

IV and PV curves are plotted at irradiance levels of 100, 500 and 1000 Wm^{-2}, which represent a low, intermediate, and high level, and thus observe if there are changes in the shape of the curves depending on this factor. In this section are only included the graphs for the irradiance level of 1000 Wm^{-2}.

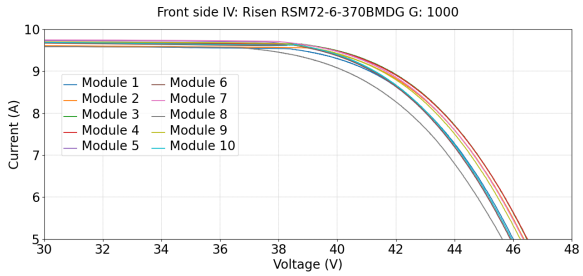

Figure 2.10: IV curves for the 10 Risen RSM72 bifacial modules at an irradiance of 1000 Wm^{-2} on the front face.

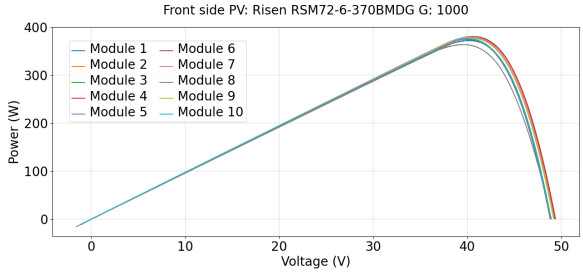

Figure 2.11: PV curves for the 10 Risen RSM72 bifacial modules at an irradiance of 1000 Wm^{-2} on the front face.

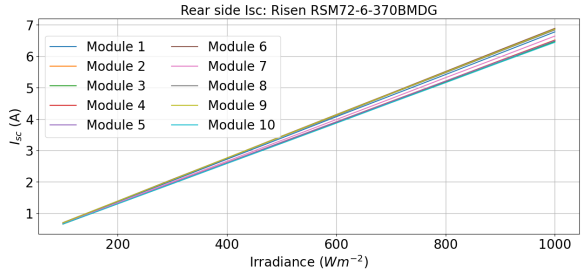

Figure 2.12: Short circuit current of the 10 Risen RSM72 bifacial modules for irradiances from 100 to 1000 Wm^{-2} on the rear face.

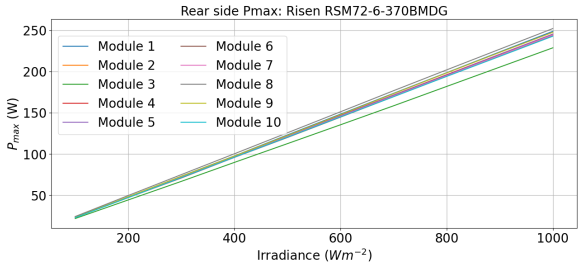

Figure 2.13: Short circuit current of the 10 Risen RSM72 bifacial modules for irradiances from 100 to 1000 Wm^{-2} on the rear face.

When the irradiances are low, the dispersion is not appreciable, however, as the irradiance level increases, the change in slopes is noticeable. Minor slopes are associated with modules N°3, N°5, and N°10, at an intermediate point finds module N°7, and the largest slopes are associated with modules N°1. In the same way as for the Risen RSM72 bifacial modules, for BOM CEAN INES PV modules, the graphics are included of IV and PV curves for the irradiance level of 1000 Wm^{-2}.

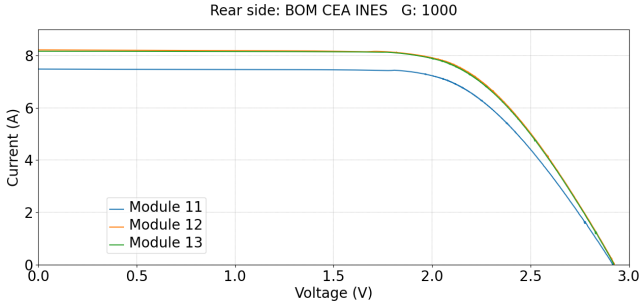

Figure 2.14: IV curves for the 3 bifacial mini modules at an irradiance of 1000 Wm^{-2} on the rear face

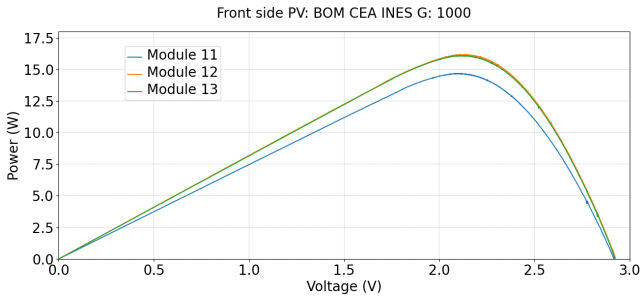

Figure 2.15: PV curves for the 3 bifacial mini modules at an irradiance of 1000 Wm^{-2} on the rear face

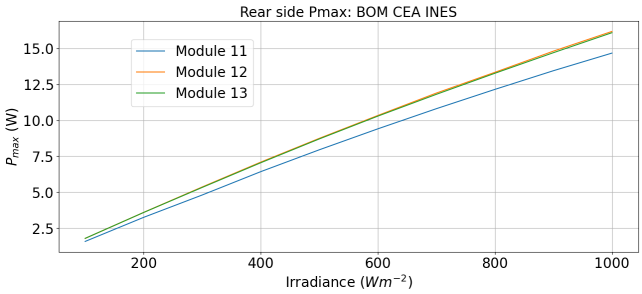

Figure 2.16: Maximum power of the 3 mini bifacial modules for irradiances from 100 to 1000 Wm^{-2} on the rear face.

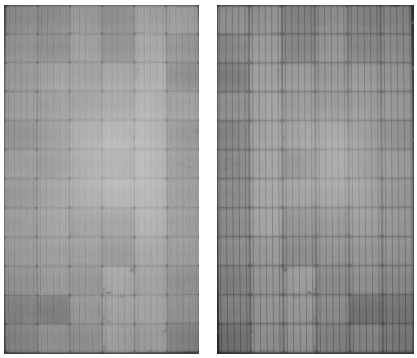

Figure 2.17: Electroluminescence results performed on bifacial module N°1 a) front face (b) rear face

2.4.2 BiFi

BiFi corresponds to the slope of the linear regression of the maximum power in function of the irradiance of the rear face of the module, this corresponds to the slope of the first points obtained in Fig. 2.13. In this case, the levels of irradiance of 100, 200 and 300 Wm^{-2}, given the recommendations of the IEC standard TS 60904-1-2:2019 [6]. The values of BiFi, $P_{\mathrm{max,STC}}$, $P_{\mathrm{max,BiF\text{-}i100}}$ and $P_{\mathrm{max,BiF\text{-}i200}}$ are presented in Table 2.8.

Module	BiFi	$P_{\mathrm{max,STC}}$	$P_{\mathrm{max,BiF\text{-}i100}}$	$P_{\mathrm{max,BiF\text{-}i200}}$
1	0.2478	-1.5619	23.2201	48.0022
2	0.2449	-1.5229	22.9644	47.4516
3	0.2256	-0.9794	21.5785	44.1364
4	0.2447	-1.2942	23.1798	47.6537
5	0.2433	-1.1149	23.2113	47.5374
6	0.2387	-0.7622	23.1059	46.9740
7	0.2434	-1.4954	22.8416	47.1787
8	0.2544	-1.4001	24.0361	49.4722
9	0.2496	-1.9960	22.9633	47.9225
10	0.2432	-1.6505	22.6696	46.9898

Table 2.8: BiFi obtained for each Risen RSM72 bifacial module and their respective $P_{\mathrm{max,STC}}$, $P_{\mathrm{max,BiF\text{-}i100}}$ and $P_{\mathrm{max,BiF\text{-}i200}}$

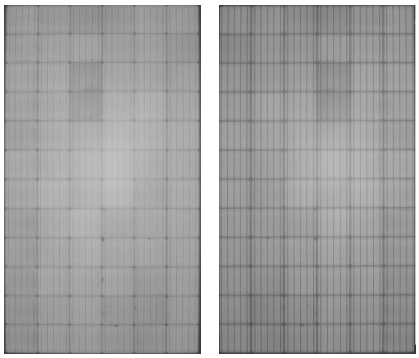

Figure 2.18: Electroluminescence results performed on bifacial module N°10 a) front face (b) rear face

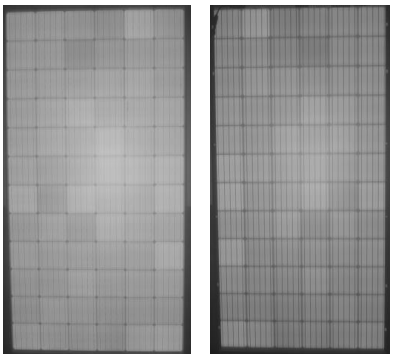

Figure 2.19: Electroluminescence results performed on bifacial module N°8 a) front face (b) rear face

2.4.3 Electroluminescence

Images obtained in the electroluminescence measurement for RISEN RSM72 PV Modules are shown in Fig. 2.17

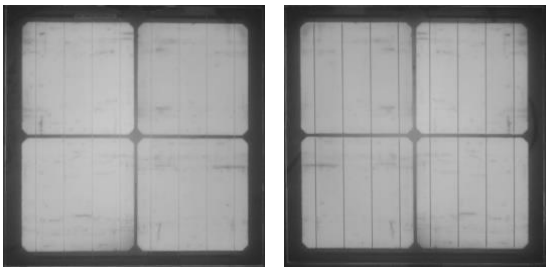

Figure 2.20: Electroluminescence results performed on bifacial module N°11 a) front face (b) rear face

The front face of the bifacial mini module BOM CEA INES N°11 shows a series of dark spots similar to stripes, which are observed both from the front and back (Fig. 2.20). These spots can be associated with the decrease in time of life of the minority carriers, since its structure resembles the impurities seen in Fig. 2.15, as well as cell contamination. Fig. 2.14, where line-shaped defects appear. The light emitted by the cells looks uniform, without appreciable differences. Electroluminescence shows no indication of the delamination mentioned on visual inspection.

2.4.4 Thermography

The images obtained in the thermography are analyzed based on the numbering showed in Table 2.8. Modules N°1, N°2, N°3, N°4, N°6 and N°7 was found positioned vertically, while the modules N°5, N°8. N°9 and N°10 were positioned horizontally.

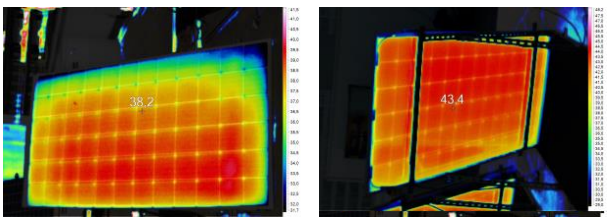

Figure 2.21: Results of thermography performed on bifacial module N°1.

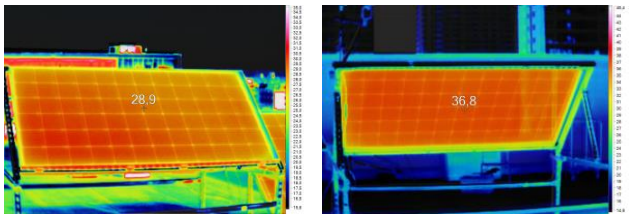

Figure 2.22: Results of thermography performed on bifacial module N°8.

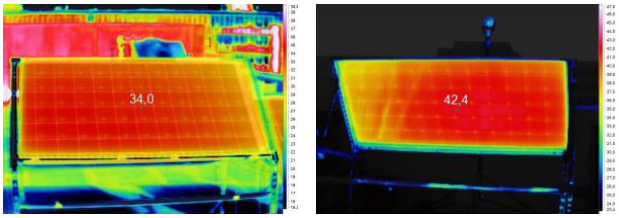

Figure 2.23: Results of thermography performed on bifacial module N°10.

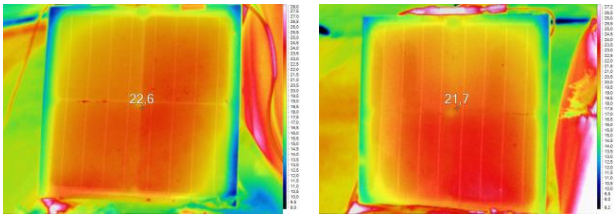

Figure 2.24: Results of thermography performed on bifacial module N°11.

2.5 Discussion

At 1000 Wm^{-2} the difference in performance can be seen clearly, in particular, the IV curve of module N°8 is less pronounced when it approaches the knee, which according to [9] can occur due to processes aging of the module and is consistent considering that the module has been in operation. As for the others, module N°1 appears within the minor maximum power levels, even reaching lower powers than in the case of module N°10, which has been previously exposed. The other curves have tightened to the previously mentioned behaviors for the irradiance levels of 100 and 500 Wm^{-2}.

As the irradiance level varies, in Fig. 2.12, the short-circuit current increases linearly. Qualita-

tively, it is observed that for the front face the value of I_{sc} does not vary much. The module that showed higher short-circuit currents when illuminated from its front face was the module N°10, while the one that reached the minors was the module N°8. In this case, no particular behavior is observed that differentiates the exposed modules of the unexposed. On the other hand, when the lighting is done on the back a clear separation is observed in the short-circuit current levels reached.

In the case of BOM CEA INES MODULES, it can be identified an abnormality in module N°11, probably caused by a delamination, which is confirmed with the IV curves and thermography test. Table 2.8 shows that the minimum BiFi value corresponds to module N°3, result that is evident when observing Fig. 2.13, since this is the one that has the lower peak power levels when lit from the back. On the other hand, the module that had the best maximum power performance was the N°8, and it coincides with the highest BiFi value. This quantitative result also allows corroborating some performances that had been previously observed on the charts, for example, the highest BiFi value corresponds to module N°6. For EL test, Fig. 2.17 shows the electroluminescence results of module N°1. In general, the first thing that is most evident is the difference in illumination of the cells, where the most illuminated is column E, contrasting with column F since it is darker. Some cells that are also particularly dark are (1,B), (2,B), (1,D), (2,D) and (11,B), which according to [10] could be due to a decrease of the lifetime of the minority carriers of the semiconductor.

In the case of module N°8 (Fig. 2.19) dark spots are observed on the edges of the last cells of columns D and E. Due to the color of the stains could be associated with type C cracking, which is associated with the disconnection of regions from the rest of the circuit, and therefore, decreasing the power performance, which was seen clearly in Fig. 2.10, where this module had the lowest performance when increasing the irradiance level of the front face. In addition, darker cells are observed, such as (3,C) and (4,C), which show faded black spots. All finds viewed by the front face are also replicated when observing the spectrum emitted by the back face. An important detail is that, although the modules that present cracks show a low in power performance, this is only apparent when lit from the face front, since on the back the behavior is totally different, reaching even to observe that the module N°8 reaches the highest levels of maximum power. In module N°10 (Fig. 2.18) some more noticeable darkening are observed in cells (2,C), (7,B) and (8,C), which can be caused by the decrease in lifetime of minority carriers. Module N°10, during thermography test, shows uniform temperature distributions, without anomalies on its front face, in the case of its rear face a fringe pattern with a lighter color (Fig. 2.23), which is attributable to reflections metal structure product.

Fig. 2.24 module N°11 has some hot spots in the area of the junction between cells (1,A) and (2,A). Hot spots evidenced fit with the areas that have presence of dirt on the surface. On the other hand, temperature distribution on the rear face of the module shows an increment in the cells of the second row, which is consistent with identified delamination. Also, the rear side shows some hot spots between cells (1,A) and (1,B), as well as at the junction between cells (1,B) and (2,B), which fits with the presence of dirt on the surface.

As a synthesis, a block diagram is made with the routines carried out and diagnoses based on the findings that can be evidenced, showed in Fig. 2.25. This considers the test suite was i) IV curves ii) electroluminescence iii) thermography.

2.6 Conclusions

The main contribution of this work is the creation of a methodology for the characterization for bifacial photovoltaic modules from three tests: plotting curves IV, electroluminescence and thermography, in addition to the detection of anomalies through complementary visual inspection. Within this, one of the points of greatest emphasis was the use of the TCLF equipment, a solar simulator specialized in the characterization of photovoltaic devices from IV curves in the laboratory.

Later, a guide was generated with procedures for measurement with and without temperature control. One of the main advantages that this device showed is the fast data acquisition, the possibility of working under standardized conditions, and finally the possibility of controlling the variables of temperature and irradiance. Regarding the characterization based on electrical variables, it was observed that the IV curves were clear in showing abnormalities in three main cases i) the presence of delamination ii) cracking iii) shading. In the case of delamination, there was a noticeable decrease in the short-circuit current of the affected device, while the cracking was shown to from the smoothing of the knee of the curve, which in the PV characteristic is evidenced as a decrease in the maximum power point. Finally, the shading generated current steps, decreasing the maximum power performance of the devices. This phenomenon was observed on the rear face of all Risen bifacial modules RSM72. With extracted parameters from the IV curves, graphs were made based on the irradiance for both the front and back face. These charts help complement the information provided by the IV curves, showing that the decreases more noticeable in the slope for the case of I_{sc} and P_{max} (BiFi) are related to degradation.

Regarding the electroluminescence tests, these provided key information to identify type A and B cracking modes, but they did not serve to detect delamination or scratches on the surface of the modules. This assay also showed cells more darkened, which could be associated with shorter lifespans of carriers minority. Contrasting these latter patterns, no marked relationship was observed between the existence of dimmer cells and the shape of the IV curves. IR image capture enabled identification of hot spots for the case of Risen RSM72 modules. The latter did not show significant variations in their IV curves, however, considering the recommendations of the standard, a follow-up of these points to prevent this type of anomaly from becoming security risk. In the case of the mini modules, this essay provided information very important for the identification of overheating in some specific cells and the junction box. In addition, with thermography it was possible to identify by means of a high temperature zone the presence of delamination in module N°11, which reaffirms that the different tests can be complemented to obtain a characterization full of modules.

Finally, it can be affirmed that carrying out the three proposed tests provides a characterization complete, since each brings a different perspective that can complement the results obtained. On the one hand, electroluminescence tests and thermography help to identify the degradation mechanisms present in the devices measured, which complement the diagnosis through IV curves, where it is observed the performance of the modules when exposed to light.

2.7 Aknowledgements

We acknowledge our funding institution ANID (FONDECYT PROYECT N°11220697).

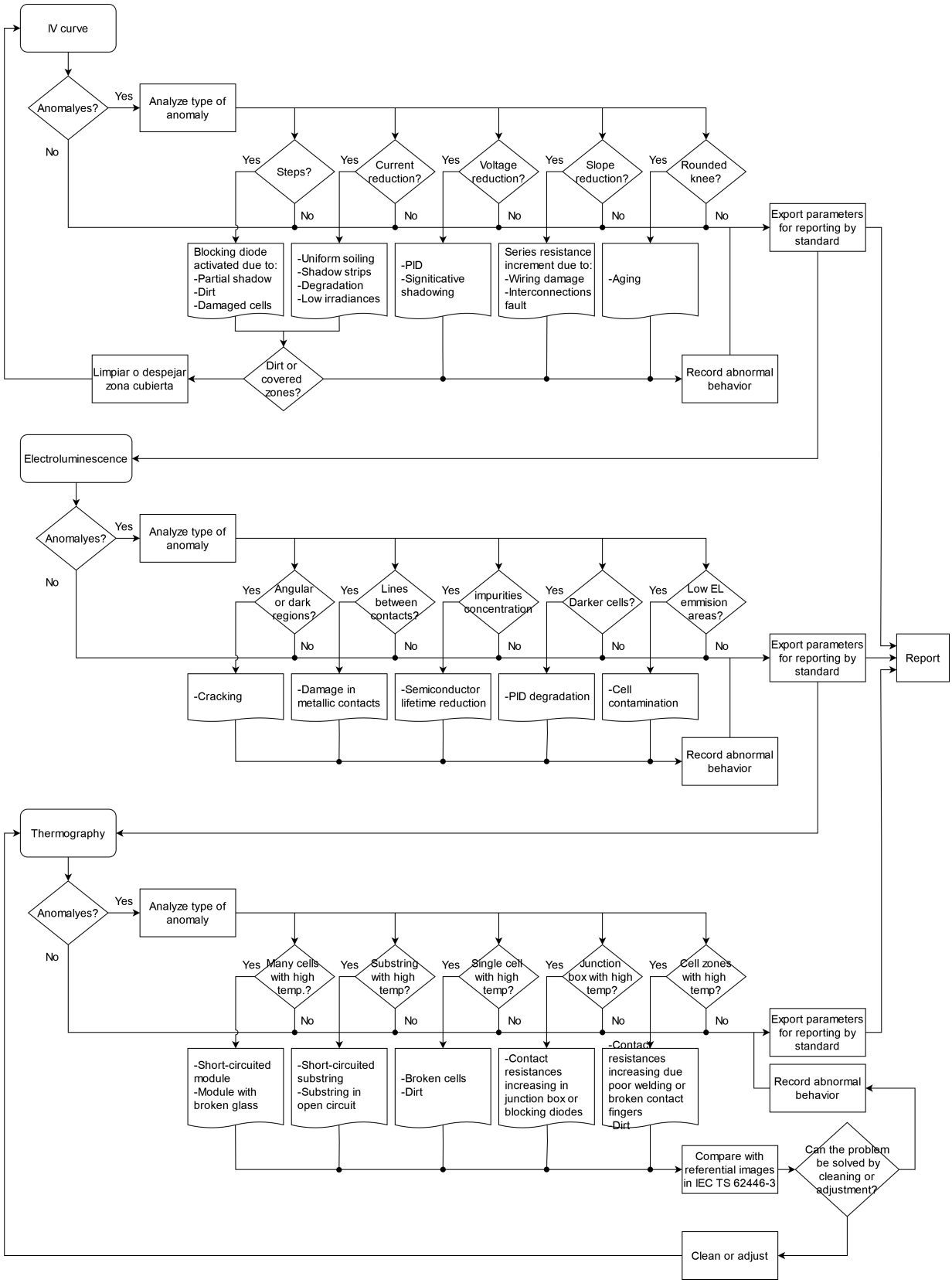

Figure 2.25: Block diagram with the measurement methodology and its possible diagnoses.

Chapter 3

Electrical model analysis for bifacial PV modules using real performance data in laboratory

Note

This article was submitted to a journal on May 5th, 2024. As it is still under review, the content may undergo changes.

Abstract

The new PV technologies, such as bifacial modules, brings the challenge of analyzing the response of numerical models and their fit to actual measurements. Thus, this study explores various models available in the literature for simulating the IV curve behavior of bifacial photovoltaic modules. The analysis contains traditional models, such as single and double-diode models, and empirical or analytical methodologies. Therefore, this paper proposes and implements a model performance assessment framework. This framework aims to establish a common basis for comparison and verify the applicability of each model by contrasting it with experimental data under controlled conditions of irradiance and temperature. The study utilizes bifacial modules of PERC+, HJT, and n-PERT technologies, tracing IV curves using a high-precision A+A+A+ solar simulator and conducting two sets of laboratory illumination measurements: single-sided and double-sided. In the first case, each face of the module is illuminated separately, while in the latter, the incident frontal illuminating light is reflected on a reflective surface. Experimental data obtained from these measurements are used to evaluate three different approximations for bifacial IV curve models in the case of double-sided illumination. The employed model for single-sided illumination is a single-diode model. The evaluation of various models revealed that shadowing from frames and junction boxes contributes to an increase in the error of modeled IV curves. However, among the three evaluated bifacial electrical models, one exhibited superior performance, with current errors approaching approximately 20%. To mitigate this discrepancy, a proposed methodology highlighted the significance of accurately estimating I_o, suggesting its potential to reduce errors.

Keywords: PV models, bifacial module, experimental data

3.1 Introduction

Bifacial photovoltaic (PV) technology, in contrast to its monofacial counterparts, offers the unique capability of harnessing solar energy from both the front and rear sides of the PV module. This technology increased

significance and is projected to capture a substantial 70% market share by 2030 [11]. The advantages of adopting bifacial PV technology over monofacial systems are diverse and compelling. First, the ability to capture light from both sides leads to notable gains in energy production [12, 13, 14]. Bifacial PV systems exhibit enhanced energy yield by leveraging reflected light from the ground, surrounding surfaces, and even the sky. Second, the deployment of bifacial modules, even with a simple arrangement, contributes to a reduction in the levelized cost of energy. However, this cost reduction can be further optimized by utilizing increased albedo, emphasizing the importance of considering the reflective properties of the installation area [15]. Last, bifacial PV technology demonstrates its value of climate change since it could offer higher power outputs for future irradiance scenarios than monofacial PV, making them a promising choice for sustainable energy generation [16]. In this scenario, it is important to have reliable tools that can accurately predict the energy production of PV modules or arrangements under different environmental conditions. Since different locations have their unique temperature levels, irradiance, humidity, and other factors, it is essential to consider these variables when modeling energy production. For that purpose, several electrical, thermal, and optical models have been developed to represent the behavior of PV devices. Considering that bifacial PV technology is relatively new, it is necessary to conduct more research to determine if current models are good enough to represent its behavior or if new modeling approaches are required to lead to more accurate predictions of energy production.

The electrical output of a PV device can be simulated using diverse models. One commonly employed approach is based on the single diode formulation [17, 18, 19, 20, 21, 22], which incorporates five parameters: photocurrent (I_{ph}), diode ideality factor (η), diode saturation current (I_{s}), series resistance (R_{s}), and shunt resistance (R_{sh}) [23]. However, as the single-diode model inherently assumes a monofacial setup, adjustments are required to accommodate the contribution of both faces of a bifacial device. The initial approximation to transform the monofacial model into a bifacial representation involves introducing an equivalent I_{ph}. This equivalent current is derived from the combination of front and rear irradiances [24, 25, 26]. An alternative representation proposed in [27, 25] for bifacial devices involves adapting the single diode model by connecting two circuits in parallel. In this configuration, one branch represents the frontal face with its respective parameters. In contrast, the other branch represents the rear. The addition of the currents generated in both branches yields I_{pv}. Studies have indicated that the configuration utilizing the equivalent current source exhibits superior performance compared to the parallel configuration [25]. In certain cases, the single-diode model has been further simplified by disregarding resistive effects and eliminating series and shunt resistances [28]. Another formulation extensively used for monofacial PV devices is the double diode model [29, 30], which has also been adapted to analyze of bifacial PV devices. This model has demonstrated remarkable accuracy under standard test conditions (STC) and in various temperature and irradiance conditions [31, 32]. The topology of the model closely resembles that of the single-diode model, with an additional diode included in parallel. Incorporating an additional diode into the two-diode model introduces two new parameters, resulting in a formulation with seven parameters. These parameters include photocurrent (I_{ph}), diode ideality factors (n_1, n_2), diode saturation currents (I_{s1}, I_{s2}), series resistance (R_{s}), and shunt resistance (R_{sh}). Some authors have applied this formulation to bifacial PV devices [33, 34]. Other formulations beyond the single and double diode models have been proposed. In [35], two monofacial electrical models are utilized. The first is an analytical model proposed by Eduardo *et al.* [36], while the second is an empirical model proposed by King *et al.* [37]. Both models demonstrated effective performance for non-real-time monitoring, particularly in clear sky conditions, with the analytical model exhibiting greater accuracy compared to the empirical model.

In fact, several electrical models have been proposed to represent the behavior of bifacial PV modules. Table 3.1 offers a comprehensive overview of how these models have been validated. Outdoor measurements emerge as the primary method utilized. However, some studies employ simulations to delve into specific aspects or scenarios. While validation methods predominantly rely on energy output and power to compare model and experimental results, the analysis of the IV curve is equally crucial. It provides valuable insights into the fit of the selected parameters and reveals any disparities between experimental data and the proposed model. In summary, the validation of the proposed electrical model to represent bifacial technology have relied on outdoor data or simulations, which may lack the control necessary for robust analysis. The limitations of outdoor measurements, such as less control over irradiance distribution and module temperature, underscore the necessity for alternative validation methods.

This article assesses existing electrical models for bifacial PV technology by utilizing high-quality data obtained in an indoor solar simulator. By conducting evaluations in a controlled environment, this research seeks to

provide a comprehensive understanding of the performance of various electrical models for bifacial PV modules based on an accurate and reliable assessments. The high-quality experimental data consists in a set of IV curve of several PV modules of different manufacturers and technologies under controlled irradiance and temperature conditions, which are obtained in a A+A+A+ Eternalsun sun simulator. Controlled conditions of irradiance are very important since the PV modules are sensitive to spectral distribution of solar irradiance [38], and specifically, the presence of clouds difficult its prediction [39]. Having a controlled ambient helps to avoid the errors coming from the optical model and the different noise sources related to clouds, reflections, and shadowing.

This research seeks to identify the most accurate electrical model for bifacial PV technology. By comparing the simulated results of different models against meticulously collected indoor data, the research aims to discern which model best captures the complex behavior of bifacial modules. Additionally, the study aims to assess the sensitivity of the best electrical models to variations in electrical parameters, providing insights into the factors that significantly impact model accuracy. This study is structured into several key sections. It begins with a concise review of the indoor characterization of bifacial PV devices, followed by an examination of proposed bifacial models found in existing literature. The methodology section provides a detailed exposition of the experimental setup and the associated data processing methodologies. Subsequent sections present the results obtained from both single-sided and double-sided measurements. Finally, the study culminates with comprehensive conclusions drawn from the synthesis of gathered data and the analyses conducted throughout the investigation.

3.2 Characterization of bifacial PV devices

Characterization of PV devices provides relevant information regarding their performance, including max power rating, efficiency, estimation of annual energy yield, sizing of system components, and determination of product value [40]. Standard IEC 60904-1-2 [41] provides recommended electrical parameters for reporting and the corresponding measurement methods for bifacial PV devices. This overview will center on two types of illumination: single and double-sided. Specifically, the emphasis will be on indoor measurements, focusing on laboratory tests.

3.2.1 Single-sided illumination

When measuring IV curves on bifacial devices, one consideration is to illuminate only one side. The standard IEC 60904-1-2 specifies that the limit of irradiance on the non-illuminated side should be less than 3 Wm^{-2}. There are multiple methods available to achieve this requirement:

- Use a non-reflective material behind the non-illuminate side.
- Limit the exposure of the module illuminating with a source of the size of the module.
- Cover the non-illuminated side with a black surface.

Liang *et al.* [42] investigated the considerations outlined in the standard and devised an experimental setup comprising two distinct darkrooms. They aimed to generate varying background reflections to examine their impact on characterization results. Their findings revealed that the non-uniformity of irradiance influences two parameters: fill factor and maximum power. Moreover, irradiances exceeding 3 Wm^{-2} were found to introduce uncertainties to the maximum power measurements. It is important to carefully consider the conditions under which the rear surface is exposed during single-sided characterization to minimize the effects of reflections and non-uniform irradiance. Implementing the recommended methods from the standard is crucial in addressing these issues. Razongles *et al.* [43] examined parasitic reflections occurring when the bifacial module is positioned away from the black screen surface to mitigate the effects above. They suggested placing a black screen directly on the back of the module to minimize reflections.

Table 3.1: Proposed validation methods.

Validation method	Ref	Proposed model	Evaluation method	PV device	Technology	Measurement conditions
Outdoor measurement	[27]	Parallel single diode	IV curve	Cell	Not reported	Temperature: 25-55°C. Irradiance: 1000 W/m^2.
				Module	Not reported	Albedo: 0.16. Irradiance: 900 ± 20 W/m^2.
Outdoor measurement	[33]	Double diode	Annual bifacial gain and energy output	Cell	N-type	Vertical east-west orientation. Two different albedo.
Outdoor measurement	[34]	Single and double diode	IV curve	Module	N-type	Frontal irradiance at 1000 W/m^2 while rear irradiance varies between 0% and 30%.
Outdoor measurement	[25]	Single diode traditional and parallel configuration	Power and cumulative energy	Module	Not reported	Daily performance estimation, considering summer and winter days.
Outdoor measurement	[35]	Analytical and empirical	DC power	Monofacial and bifacial PV array	PERC	Variation in albedo levels Different levels of temperature and irradiance depending on weather conditions.
Simulation	[26]	Single diode	Energy yield	Module	Not reported	Daily and yearly performance estimation, considering sunny and cloudy days.
Simulation	[28]	Single diode	IV curves for monofacial and bifacial module	Module	Not reported	STC condition: 25°C and 1000 W/m^2. 20°C and 800 W/m^2.

3.2.2 Double-sided illumination

In the case of double-sided illumination, it is crucial to accurately measure both frontal and rear irradiances and develop a method to illuminate both faces consistently. There are various arrangements and measurement techniques. For instance, Lagunas *et al.* [44] utilized a 10ms pulse class-A flash simulator to illuminate the device, with two glasses and mirrors positioned at a 45° tilt from the direction of the light pulse. A mesh was employed to control rear face light. Irradiance was measured using a reference cell, while current and voltage were gauged using probes. This setup enabled distinct irradiance levels on each side of the PV device. Different scenarios were examined to compare the IV curve behavior when the device was illuminated separately from each side or simultaneously. Results revealed that simultaneous illumination from both sides led to a lower maximum power point than the sum of currents obtained under separate illumination conditions.

Zhang *et al.* [45] comprehensively compared one-sided and two-sided illumination. Their experimental setup involved a light source directed towards a bifacial cell, and a white smooth plate capable of reflecting incident light. The same configuration was used for single-sided measurements, albeit with adjustments made to the distance between the laminates and the light source. They evaluated three different types of bifacial cells: n-type, p-type, and HJT. In contrast to the findings of Lagunas *et al.*, they observed that two-sided illumination resulted in higher levels of maximum power points than to one-sided illumination.

Finally, Razongles *et al.* [43] implemented two indoor setups. The first is implemented for large modules, where two identical Eternal Sun sun simulators were ubicated at each device surface. With this configuration the irradiance can be totally controlled for both surfaces. The second setup utilized an aluminum-mirror arrangement specifically designed for 4-cell modules. This setup is very similar to the proposal of Lagunas *et al.*, using a mesh as a filter to control the irradiance on the rear face.

Across the various presented setups, several commonalities emerge. Firstly, each setup utilizes reference cells to measure irradiances accurately. Additionally, there is a consistent practice of attenuating incident light on the rear face of the setup, emulating the albedo effect. These methodological consistencies serve as foundational pillars for the forthcoming exposition of our proposed setup, to be detailed in the Methodology section.

3.3 Bifacial electrical models

Previously, various models were discussed to elucidate the approaches adopted by different authors representing the electrical characteristics of bifacial PV modules. Among these models, the single-diode model (SDM) stands as a conventional choice. It is depicted in Eq. (3.1), where the current sources symbolize both the frontal and rear sides of the bifacial module. Fig. 3.1 shows a schematic representation of this model.

$$I_{\mathrm{pv}} = I_{\mathrm{ph,f}} + I_{\mathrm{ph,r}} - I_{\mathrm{s}} \left[\exp\left(\frac{V_{\mathrm{pv}} + I_{\mathrm{pv}} \cdot R_{\mathrm{s}}}{N_{\mathrm{s}} \cdot V_{\mathrm{t}} \cdot n} \right) - 1 \right] - \frac{(V_{\mathrm{pv}} + I_{\mathrm{pv}} \cdot R_{\mathrm{s}})}{R_{\mathrm{sh}}} \tag{3.1}$$

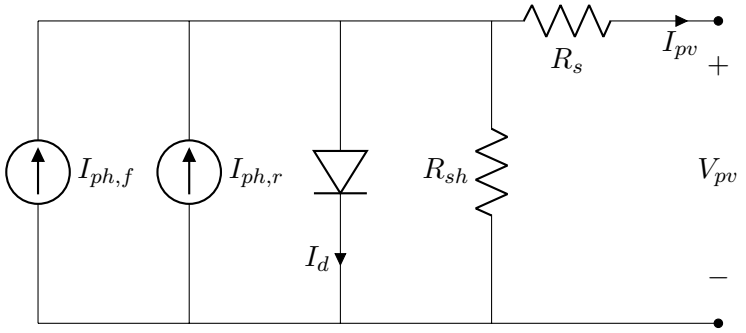

Figure 3.1: Single diode model adapted for bifacial PV devices.

An alternative representation of the single diode model employs two parallel branches, each corresponding to one side of the module. This configuration is illustrated in Fig. 3.2. The resultant current, denotated by I_{pv} in

Eq. (3.2) is the sum of Eq. (3.3) and Eq. (3.4).

$$I_{\mathrm{pv}} = I_{\mathrm{f}} + I_{\mathrm{r}} \tag{3.2}$$

$$I_{\mathrm{f}} = I_{\mathrm{ph,f}} - I_{\mathrm{s,f}} \left[\exp\left(\frac{V_{\mathrm{pv}} + I_{\mathrm{f}} \cdot R_{\mathrm{s,f}}}{N_{\mathrm{s}} \cdot V_{\mathrm{t,f}} \cdot n} \right) - 1 \right] - \frac{V_{\mathrm{pv}} + I_{\mathrm{f}} \cdot R_{\mathrm{s,f}}}{R_{\mathrm{sh,f}}} \tag{3.3}$$

$$I_{\mathrm{r}} = I_{\mathrm{ph,r}} - I_{\mathrm{s,r}} \left[\exp\left(\frac{V_{\mathrm{pv}} + I_{\mathrm{r}} \cdot R_{\mathrm{s,r}}}{N_{\mathrm{s}} \cdot V_{\mathrm{t,r}} \cdot n} \right) - 1 \right] - \frac{V_{\mathrm{pv}} + I_{\mathrm{r}} \cdot R_{\mathrm{s,r}}}{R_{\mathrm{sh,r}}} \tag{3.4}$$

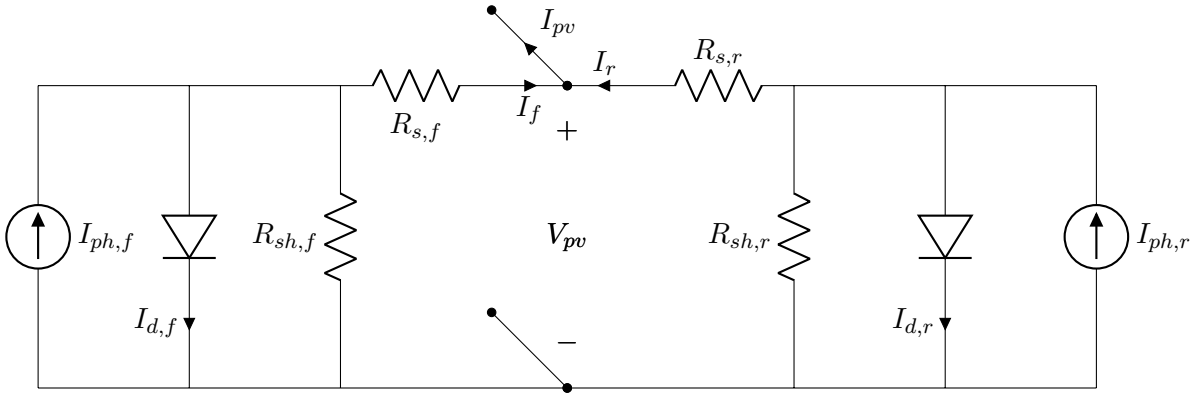

Figure 3.2: Paralell configuration of the single diode model for bifacial PV devices.

Another commonly employed model is the double-diode model (DDM), as depicted in Eq. (3.5). This formulation introduces an additional diode-current, necessitating the inclusion of two additional terms for I_{o} and n. A visual representation is found in Fig. 3.3.

$$I_{\mathrm{pv}} = I_{\mathrm{ph,f}} + I_{\mathrm{ph,r}} - I_{\mathrm{s1}} \left[\exp\left(\frac{V_{\mathrm{pv}} + I_{\mathrm{pv}} \cdot R_{\mathrm{s}}}{N_{\mathrm{s}} \cdot V_{\mathrm{t}} \cdot n_1} \right) - 1 \right] - I_{\mathrm{s2}} \left[\exp\left(\frac{V_{\mathrm{pv}} + I_{\mathrm{pv}} \cdot R_{\mathrm{s}}}{N_{\mathrm{s}} \cdot V_{\mathrm{t}} \cdot n_2} \right) - 1 \right] - \frac{V_{\mathrm{pv}} + I_{\mathrm{pv}} \cdot R_{\mathrm{s}}}{R_{\mathrm{sh}}} \tag{3.5}$$

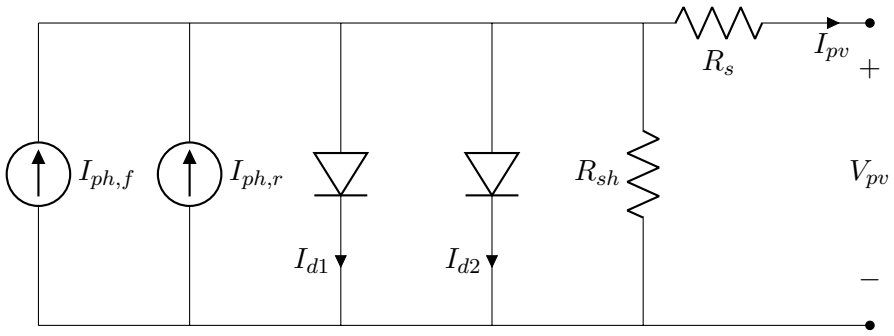

Figure 3.3: Double diode model adapted for bifacial PV devices

3.3.1 The bifacial representation

As previously discussed, various models derive the IV curve and energy production for bifacial PV devices. Regardless of the specific model used, a crucial consideration lies in how these models effectively represent the bifacial nature of the device. Following parameter estimation, decisions must be made regarding each element

in the circuit. In the work of [33], for instance, they proposed rescaling the parameters I_{ph}, I_{s1}, I_{s2}, and R_s for both the front and rear faces while neglecting R_{sh}. This rescaling process is accomplished by incorporating the respective frontal and rear irradiances, as shown in Eqs. (3.6) and (3.7).

$$I_{ph(f+r)} = \frac{I_{f,sc} \cdot G_f + I_{r,sc} \cdot G_r}{G_{STC}} \tag{3.6}$$

$$X = \frac{X_f \cdot G_f + X_r \cdot G_r}{G_f + G_r} \tag{3.7}$$

Where the term X represents I_{s1}, I_{s2}, and R_s. It is important to note that $I_{r,sc}$ is not a parameter found in datasheets. Furthermore, calculating $I_{s1,r}$, $I_{s2,r}$, and $R_{s,r}$ requires data for the rear face, which can be obtained from measurements.

In [34], both single and double-diode models were implemented. For parameter calculation, they conducted a two-stage optimization process. The current source is determined using the bifaciality factor ($\phi_{I_{sc}}$), as shown in Eq. (3.8):

$$I_{ph(f+r)} = I_{ph}(1 + \phi_{I_{sc}}) \tag{3.8}$$

Subsequently, a new series resistance, denoted as R_{add}, is introduced to R_s, resulting in a combined series term of $R_s + R_{add} \cdot \phi_{I_{sc}}$. The mathematical representation of the single-diode model is depicted in Eq. (3.9). To incorporate the double-diode model, it simply needs to add the term corresponding to the second diode.

$$I_{pv} = I_{ph}(1 + \phi_{I_{sc}}) - I_{s1}\left[\exp\left(\frac{V_{pv} + I_{pv} \cdot (R_s + R_{add} \cdot \phi_{I_{sc}})}{N_s \cdot V_t \cdot n_1}\right) - 1\right] - \frac{V_{pv} + I_{pv} \cdot (R_s + R_{add} \cdot \phi_{I_{sc}})}{R_{sh}} \tag{3.9}$$

In other studies, such as [26], a single-diode model is implemented by considering only the frontal face parameters. As given by Eq. (3.10), the adjustments for bifacial representation involve rescaling the irradiances for the I_{ph} term when parameter extraction is performed under non-STC conditions.

$$I_{ph} = \frac{G_E}{G_{ref}}(I_{ph,ref} + \alpha(T - T_{ref})) \tag{3.10}$$

Here, G_E is the equivalent irradiance obtained from Eq. (3.11).

$$G_E = G_f + G_r \cdot \phi \tag{3.11}$$

The subscript "ref" refers to standard test conditions (STC), α represents the temperature coefficient for I_{sc}, and ϕ denotes the bifaciality factor.

In the case of [35], the bifacial behavior is quantified by the "bifacial gain of irradiance", defined in Eq. (3.12).

$$BG_g = 100 \cdot \frac{G_r}{G_{POA}}(1 - \eta_{loss}) \tag{3.12}$$

Notably, the authors applied the model to outdoor experimental data, hence the usage of G_{POA}, representing the irradiance in the plane of the array, and η_{loss}, indicating the loss of power due to non-homogeneity in the rear irradiance.

3.3.2 Models evaluation

After reviewing the presented models and their respective validations, three have been chosen for a comprehensive evaluation of their performance using experimental data under controlled irradiance and stable temperature conditions. The selection criteria are based on their replicability and the diverse modeling approaches employed. The chosen models are as follows:

- **Gu *et al.*** [26] The single-diode model requires 5 parameters. The estimation method the authors proposed for these parameters is implemented as described by Eqs. (3.13) to (3.17).

$$V_{\mathrm{t,ref}} = \frac{\beta \cdot T_{\mathrm{ref}} - V_{\mathrm{oc,ref}}}{\frac{N_s \cdot T_{\mathrm{ref}} \cdot \alpha}{I_{\mathrm{ph,ref}}} - 3 \cdot N_s - \frac{E_g \cdot N_s}{K \cdot T_{\mathrm{ref}}}} \tag{3.13}$$

$$I_{\mathrm{ph,ref}} \approx I_{\mathrm{sc,ref}} \tag{3.14}$$

$$I_{\mathrm{s,ref}} = I_{\mathrm{sc,ref}} \cdot \exp\left(\frac{-V_{\mathrm{oc,ref}}}{N_s \cdot V_{\mathrm{t,ref}}}\right) \tag{3.15}$$

$$R_{\mathrm{sh,ref}} = \frac{(V_{\mathrm{mp,ref}} - I_{\mathrm{mp,ref}} \cdot R_{\mathrm{s,ref}})(V_{\mathrm{mp,ref}} - N_s \cdot V_{\mathrm{t,ref}})}{(V_{\mathrm{mp,ref}} - I_{\mathrm{mp,ref}} \cdot R_{\mathrm{s,ref}})(I_{\mathrm{sc,ref}} - I_{\mathrm{mp,ref}}) - N_s \cdot V_{\mathrm{t,ref}} \cdot I_{\mathrm{mp,ref}}} \tag{3.16}$$

$$I_{\mathrm{mp,ref}} = I_{\mathrm{ph,ref}} - I_{\mathrm{s,ref}}\left[\exp\left(\frac{V_{\mathrm{mp,ref}} + I_{\mathrm{mp,ref}} \cdot R_{\mathrm{s,ref}}}{N_s \cdot V_{\mathrm{t,ref}}}\right) - 1\right] - \frac{(V_{\mathrm{mp,ref}} + I_{\mathrm{mp,ref}} \cdot R_{\mathrm{s,ref}})[(V_{\mathrm{mp,ref}} - I_{\mathrm{mp,ref}} \cdot R_{\mathrm{s,ref}})(I_{\mathrm{sc,ref}} - I_{\mathrm{mp,ref}}) - N_s \cdot V_{\mathrm{t,ref}} \cdot I_{\mathrm{mp,ref}}]}{(V_{\mathrm{mp,ref}} + I_{\mathrm{mp,ref}} \cdot R_{\mathrm{s,ref}})(V_{\mathrm{mp,ref}} - N_s \cdot V_{\mathrm{t,ref}})} \tag{3.17}$$

  Once the 5 parameters are calculated, they are adjusted to their actual irradiance and temperature conditions. The photocurrent (I_{ph}) is defined in Eq. (3.10), while the remaining parameters are computed using equations Eqs. (3.18) to (3.21):

$$I_{\mathrm{s}} = I_{\mathrm{s,ref}} \cdot \left(\frac{T}{T_{\mathrm{ref}}}\right)^3 \cdot \exp\left[\frac{q \cdot E_g}{k}\left(\frac{1}{T_{\mathrm{ref}}} - \frac{1}{T}\right)\right] \tag{3.18}$$

$$R_{\mathrm{s}} = R_{\mathrm{s,ref}} \tag{3.19}$$

$$R_{\mathrm{sh}} = \frac{G_{\mathrm{ref}}}{G_E} \cdot R_{\mathrm{sh,ref}} \tag{3.20}$$

$$V_t = \frac{T}{T_{\mathrm{ref}}} \cdot V_{\mathrm{t,ref}} \tag{3.21}$$

- **Janssen *et al.*** [33] Utilizes a double-diode model, where initially 7 parameters have to be estimated. However, based on the author's considerations, 3 parameters are assumed: $R_{\mathrm{sh}} = \infty$, $n_1 = 1$ and $n_2 = 2$. Then, to obtain the first diode saturation current, the formulation proposed by [46] is employed, given by Eq. (3.22).

$$I_{\mathrm{s1,ref}} = \frac{I_{\mathrm{sc}} + \alpha \cdot (T - T_{\mathrm{ref}})}{\exp\left(\frac{V_{\mathrm{oc}} + \beta \cdot (T - T_{\mathrm{ref}})}{n_1 \cdot V_{\mathrm{t}}}\right) - 1} \tag{3.22}$$

  On the other hand, the second diode saturation current is calculated by Eq. (3.23).

$$I_{\mathrm{s2,ref}} = \left(\frac{T^{\frac{2}{5}}}{3.77}\right) I_{\mathrm{s1}} \tag{3.23}$$

Finally, the series resistance is calculated by Eq. (3.19). Just I_{ph} and $I_{\mathrm{s,i}}$ are transformed to its original ambient conditions, the first is done by applying Eq. (3.6), and the second is accomplished by the application of Eq. (3.24).

$$I_{\mathrm{s(i)}} = I_{\mathrm{s(i),ref}} \cdot \left(\frac{T_{\mathrm{k}}}{T_{\mathrm{ref}}}\right)^3 \cdot \exp\left(\frac{qE_{\mathrm{g}}}{n_{\mathrm{i}}k}\left(\frac{1}{T_{\mathrm{ref}}} - \frac{1}{T_{\mathrm{k}}}\right)\right) \tag{3.24}$$

- **Bhang *et al.*** [27] Proposed a single-diode model with a parallel configuration, resulting in the estimation of 10 parameters, 5 for the frontal face and the other 5 for the rear. A W-Lambert parameter estimation is employed to obtain it, utilizing the measured values at STC for both faces. Finally, the parameters are corrected utilizing Eqs. (3.10) and (3.18) to (3.20).

3.4 Methodology

3.4.1 Setup

This section describes the equipment utilized for measurements, beginning with PV bifacial modules and then proceeding to the sun simulator.

3.4.1.a Bifacial modules

Table 3.2 displays the various modules subjected to measurement. Different technologies were employed, with a predominant use of PERC+ and HJT. The last column indicates the specific test to be conducted, which will be elucidated in the subsequent sections. It is worth mentioning that GOPV PSDA6, HET GO 25 and n-PERT modules are frameless, whereas Risen, Trina, and SunPower modules are equipped with frames.

Table 3.2: Modules utilized for IV curve tracing with the sun simulator.

Module	Pmax (W)	Technology	Test
Risen RSM72-6-370BMDG	370	PERC+	SS, DS
GOPV PSDA 6	393	HJT	SS
HET GO 25	355	HJT	SS
n-PERT	348	n-PERT	SS
Trina TSM-490DEG18MC.20(II)	490	PERC+	DS
SunPower SPR-P6-500-COM-S-BF	500	PERC+	SS, DS

3.4.1.b Solar simulator

The Eternalsun sun simulator (A+A+A+ class) is employed to illuminate and trace IV curves for the selected modules. The sun simulator utilizes a single long-pulse filtered xenon tube lamp in the bottom chamber. Consequently, the module and reference cell must be oriented towards the bottom to receive the light. The irradiance levels can be controlled within 100 to 1200 Wm^{-2}.

The upper chamber is mobile, allowing it to be lowered to cover the module completely, preventing the entry of external light. The interior of the upper chamber is black, eliminating any reflection of the emitted light. Once the upper chamber is lowered, temperature control is possible within a range of 10 to 75°C.

A reference cell is connected to measure irradiance, and within the interior of the bottom chamber, there is another cell named the "monitor cell", which measures both irradiance and temperature.

Temperature measurement employs two instruments: the first utilizes four T-type thermocouples, primarily when tracing IV curves at different temperatures, as it allows temperatures above 100°C. The second is an IR thermal sensor, allowing temperature measurements up to approximately 49°C.

3.4.2 Measurement

The following sections describe the two tests conducted, the first one using single-sided illumination and the second one with double-sided illumination.

3.4.2.a Single-sided illumination (SS)

The PV modules listed in Table 3.2 underwent the tracing of their IV curves at STC conditions, as depicted in Fig. 3.4. For temperature measurement, four T-type thermocouples are affixed to the module using aluminum foil tape following the method outlined in the standard IEC 60891.

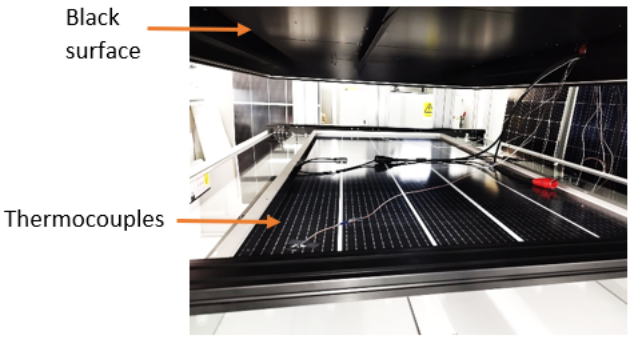

Figure 3.4: Solar simulator setup for single-sided measurement.

3.4.2.b Double-sided illumination (DS)

For this measurement, a 90% reflective film is employed to cover the surface of the upper chamber. This arrangement allows for the light emitted from the bottom to be partially reflected by this surface, thereby illuminating the rear face of the bifacial module.

As the reflected light onto the rear surface is not uniform, it becomes crucial to measure the irradiance across the surface of the modules. The modules were virtually divided into nine sections, marked by the red X symbols in Fig. 3.6. The resulting irradiance distributions are named "irradiance matrix". Irradiance measurements were conducted with a reference cell positioned in each section. Additionally, an extra point is included below position 2C, which is the reference cell's position after irradiance measurement. This adjustment helps prevent shadowing on the rear face during IV curve tracing.

With this configuration, the upper chamber remains lifted to maintain reflection onto the surface. In this case, temperature cannot be controlled. However, frontal irradiance can also be regulated, affecting the rear irradiance. The module is exposed to irradiances ranging from 100 to 1000 Wm^{-2}, in 100 Wm^{-2} increments. For every data point, the rear irradiance is measured in the position below 2C.

3.4.3 Data processing and model approach

The processing will be divided into two parts, each corresponding to a different test. Among the seven models listed in Table 3.1, three have been chosen for their replicability, a selection process that will be detailed further below.

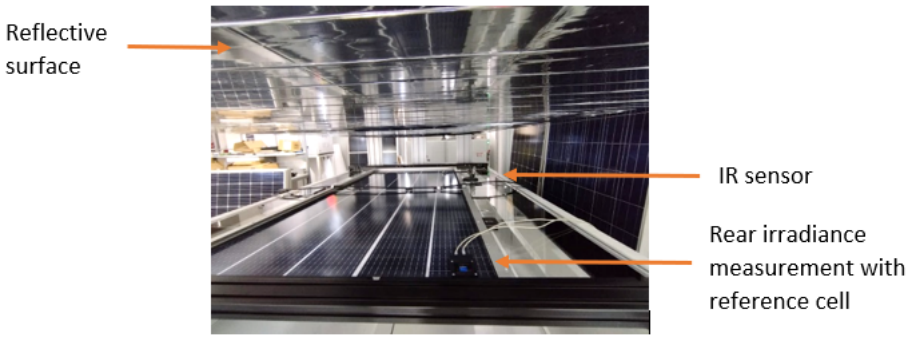

Figure 3.5: Solar simulator setup for double-sided measurement.

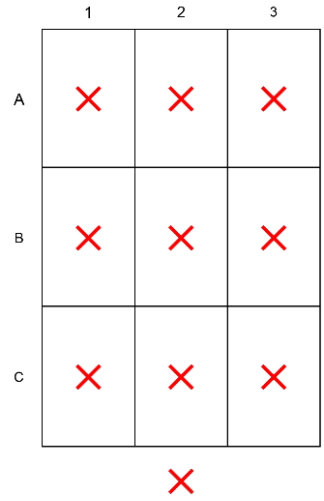

Figure 3.6: Rear irradiance measuring points to evaluate uniformity in the surface of the module.

3.4.3.a Single-sided illumination measurement (SS)

In this measurement, the frontal and rear faces are tested to obtain their respective IV curves for STC conditions. It is important to note that the bifacial models previously discussed cannot be applied here, as two IV curves are traced separately. The primary objective of this test is to examine the behavior of each module face independently and to observe any potential differences between them.

In this scenario, the single-diode model is applied to analyze each IV curve. The standard test condition (STC) measured points (I_{sc}, V_{oc}, I_{mpp}, and V_{mpp}) are employed for both the frontal and rear faces. Subsequently, these data points are inputted into the 5-parameter model for each face of the module. Following parameter acquisition, the models are used to simulate the IV curves. The comparison between the simulated and experimental IV curves involves calculating percent errors for voltage values, considering I_{sc} for current and P_{max} for power. Fig. 3.7 summarizes every step of this measurement.

3.4.3.b Double-sided illumination measurement (DS)

In this case the measured irradiances in Fig. 3.6 are used to determine the minimum irradiance value under the assumption that this value limits the short-circuit current, given that each cell operates as a miniature current source [47]. This minimum value, along with the STC measured points, serves as input for evaluating the proposed models by [26], [27] and [33].

Once the irradiances are measured, the reference cell is located under the 2C position, and IV curves are traced

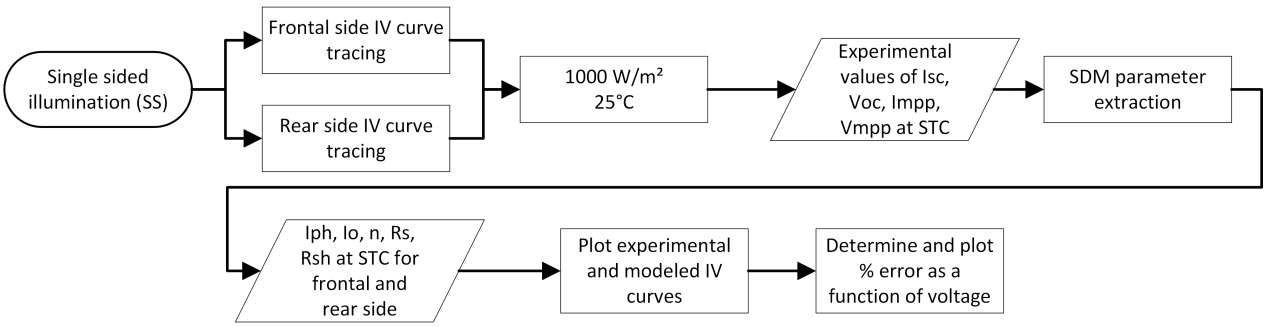

Figure 3.7: Single-sided illumination measurement explanation scheme.

in the range from 100 to 1000 Wm^{-2} for the frontal side. The data used for evaluating the models is the STC data corresponding to I_{sc}, V_{oc}, I_{mpp}, and V_{mpp}, previously obtained by the single-sided illumination measurement.

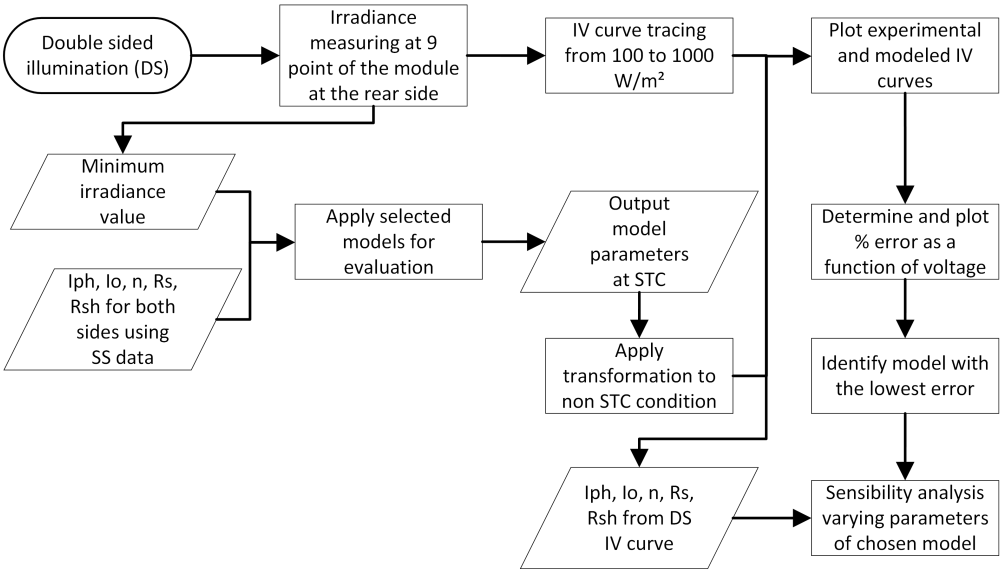

Figure 3.8: Double-sided illumination measurement explanation scheme.

Analogous to SS measurements, percent errors are calculated by comparing experimental and modeled data to ascertain the model with the best performance. Once this model is identified, it undergoes comparison with direct parameter extraction using IV curves under DS illumination. Subsequently, a sensitivity evaluation is conducted to determine which parameters have the most significant impact on IV curve tracing.

3.5 Results and discussion

The results are divided into two sections: single-sided and double-sided measurements. The best model from the double-sided measurements is then chosen for further parameter evaluation.

3.5.1 Single-sided illumination measurement

IV curves for the five modules under STC conditions are modeled with SDM and contrasted with experimental data. Figs. 3.9 to 3.11, 3.13 and 3.14 display both frontal and rear IV curves for each module (left) and illustrate

the differences between the estimated and measured values across the complete IV curve (right). These differences are particularly pronounced near the maximum power point. The module which presents the most appreciable differences between estimated and modeled current is SunPower, reaching a percentage error close to 20% on the rear side, while the smaller differences are found in HET GO 25, with a maximum error in its rear side slightly superior to -2.5%.

When the rear side is illuminated at 1000 Wm^{-2}, the shadowing effect caused by the frames becomes apparent. This effect manifests as steps in the IV curve, leading to corresponding steps in the difference between the model and experimental data. In certain instances, such as with the SunPower module, additional shadowing occurs due to the connection box, leading to more pronounced steps along the IV curve and a significant disparity near the maximum power point. This effect could explain the behavior detailed previously, when the rear side reached the maximum differences. While this behavior may not significantly affect maximum power estimation in tilted configurations, it could pose challenges in vertical east-west orientations since the sun illuminates directly both sides.

In cases where shadowing effects are minimal, such as HET GO25, HJT GOPV PSDA 6 and nPERT modules, both frontal and rear face IV curves exhibit smaller errors, and the error plots behave very similar along the curve. Errors in current do not exceed $\pm 5\%$ at the maximum difference point, indicating a high level of agreement between the experimental data and the model.

It is evident when comparing IV curve for frame or frameless modules, where the most affected was the SunPower, whose rear side was affected to the level of reaching errors close to 20%. For frameless modules, the higher error levels were reached in the maximum power point. Finally, when shadowing effects are minimal V_{oc} for frontal and rear sides are very close, like modules HET GO 25 or HJT GOPV PSDA 6, while clear differences appears in the modules SunPower, Risen and n-PERT.

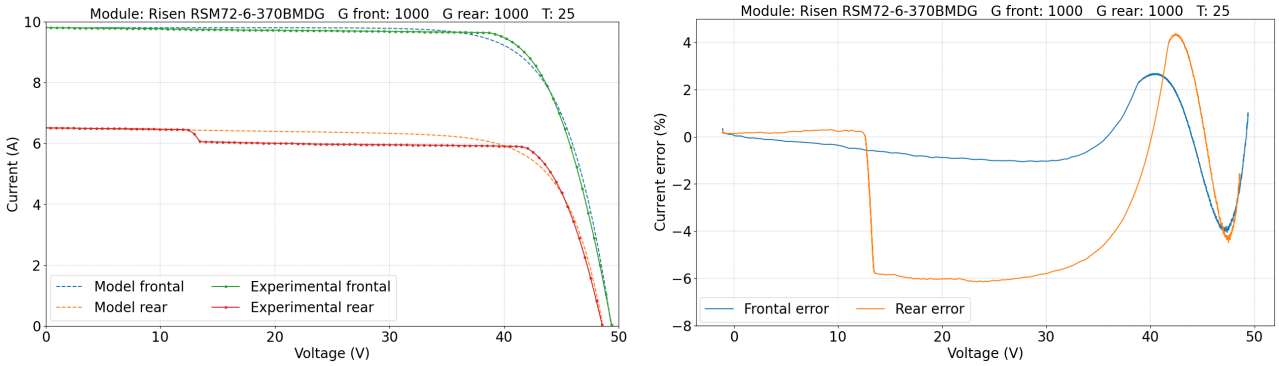

Figure 3.9: IV curves for frontal and rear faces of Risen RSM72-6-370BMDG (left) and current difference between experimental data and model results (right).

3.5.2 Double-sided illumination measurement

For this dataset, the three models (Gu *et al.*, Janssen *et al.* and Bhang *et al.*) are evaluated and compared with experimental data. IV and PV curves are traced, and their respective differences are plotted to identify which one exhibits the minimum and maximum deviations from the experimental data, as seen in Figs. 3.15 to 3.17.

SunPower and Risen modules' frontal and rear faces were separately tested in the SS measurement. Although both exhibited a gap due to the shadowing effect, their IV curves aligned well in the I_{sc} and V_{oc} regions, with the most significant deviations observed near the maximum power point, which can be seen in the error plots. However, in the bifacial IV and PV curves, while the estimation of I_{sc} closely matched the actual data, deviations appeared as the curves approached the maximum power point and Voc region. Power and current differences between experimental and modeled data were evident for the two mentioned modules, and depending on the evaluated model, this differences can reach values near 100%, which is the case of Bhang *et al.* model.

When comparing the current and power differences, it was observed that the single-diode model proposed by Gu

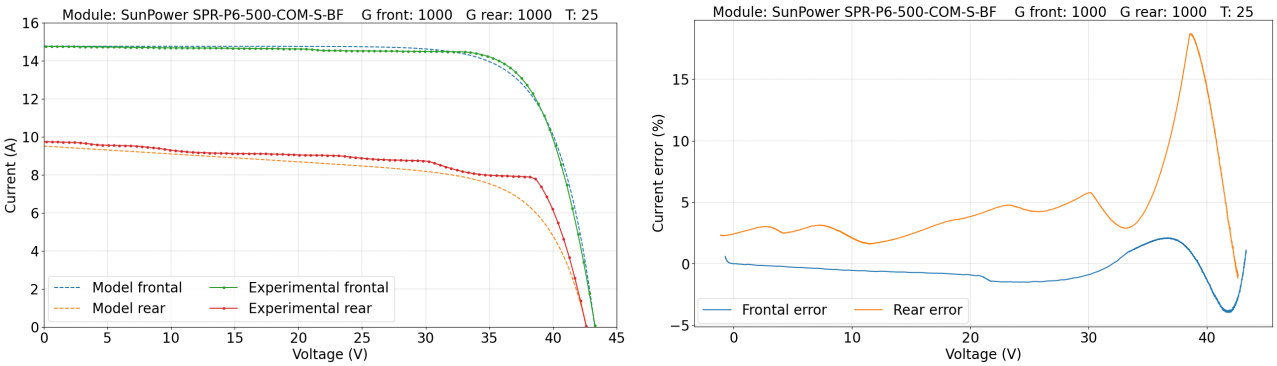

Figure 3.10: (IV curves for frontal and rear faces of SunPower SPR-P6-500-COM-S-BF (left) and current difference between experimental data and model results (right).

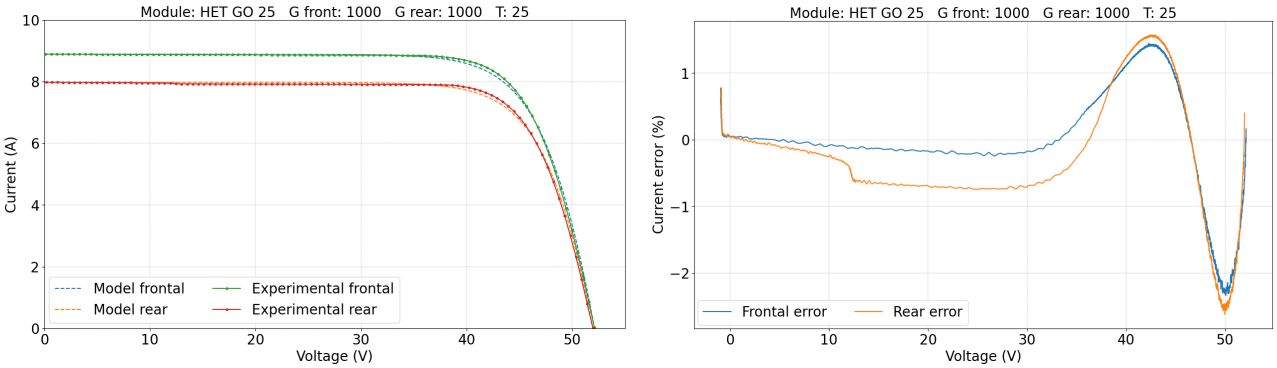

Figure 3.11: IV curves for frontal and rear faces of HET GO25 (left) and current difference between experimental data and model results (right).

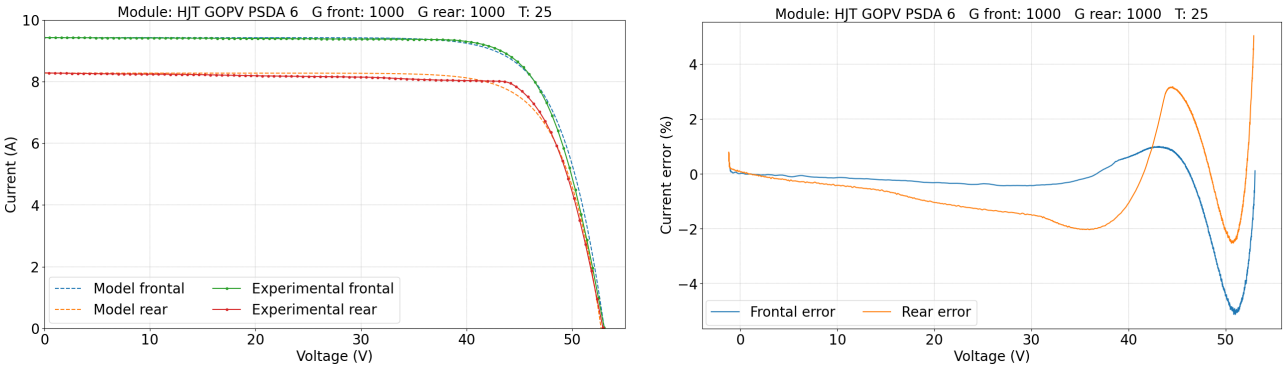

Figure 3.12

Figure 3.13: IV curves for frontal and rear faces of HJT GOPV PSDA 6 (left) and current difference between experimental data and model results (right).

et al. provided the closest representation of the complete IV curve, which can be seen from the error plots, where the maximum difference is close to 30%. It was followed by Janssen *et al.*'s double diode model with parameter escalation by irradiances, which tends to have more differences while approaching to maximum power point and V_{oc} region. Finally, the parallel single diode model showed poor performance as it tended to underestimate P_{max} and V_{oc}, generating the higher differences at the end of the IV curve caused by the poor voltage estimation.

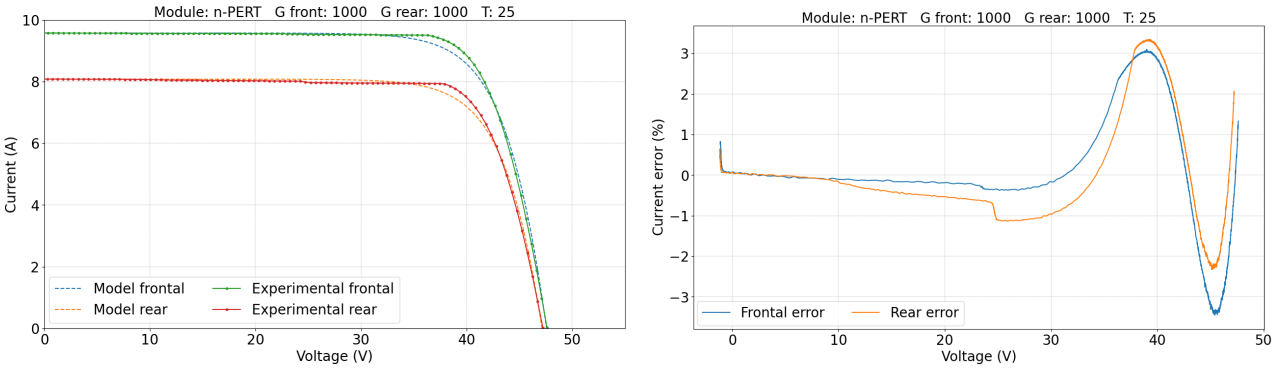

Figure 3.14: IV curves for frontal and rear faces of n-PERT (left) and current difference between experimental data and model results (right).

From the analyzed behavior when the frontal face is illuminated at 1000 Wm^{-2}, it is noted that the maximum power point and Voc are the two critical points for comparing each model and its fitting with experimental data. To observe what happens at other irradiance points, the difference between modeled and experimental Pmax, and the difference between the current in the last data point of the plot, is calculated, showed in Figs. 3.18 to 3.20. The results showed that the best fit for the remaining points is still the proposed model by Gu *et al.*

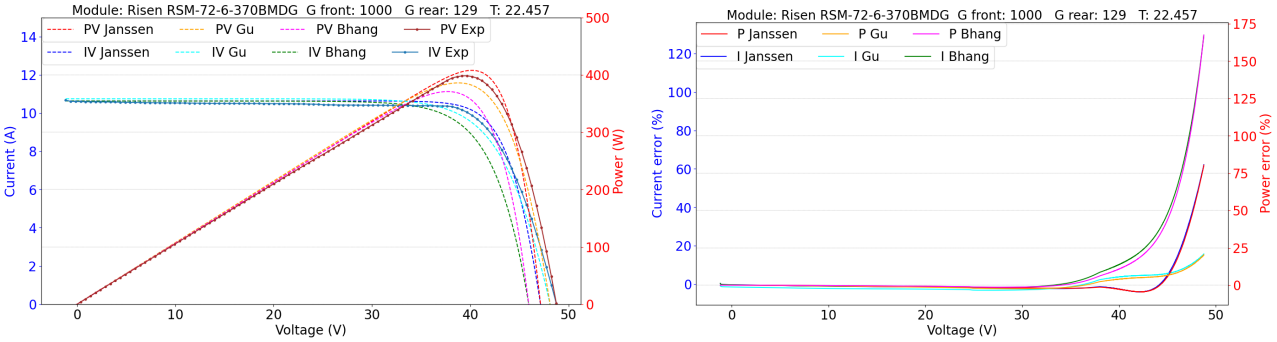

Figure 3.15: IV and PV curves for experimental and modeled data (left) and current and power differences between each model and experimental data (right), illustrated for module Risen RSM72-6-370BMDG.

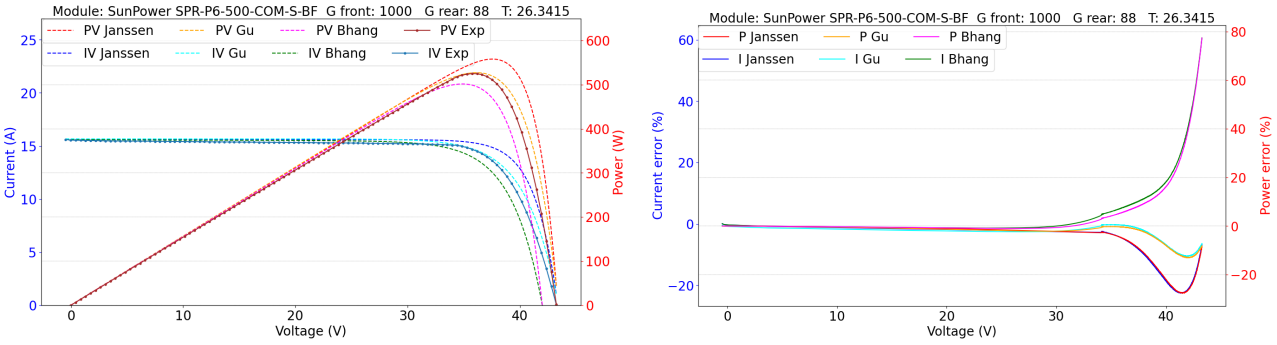

Figure 3.16: (a) IV and PV curves for experimental and modeled data (left) and current and power differences between each model and experimental data (right), illustrated for module SunPower SPR-P6-500-COM-S-BF.

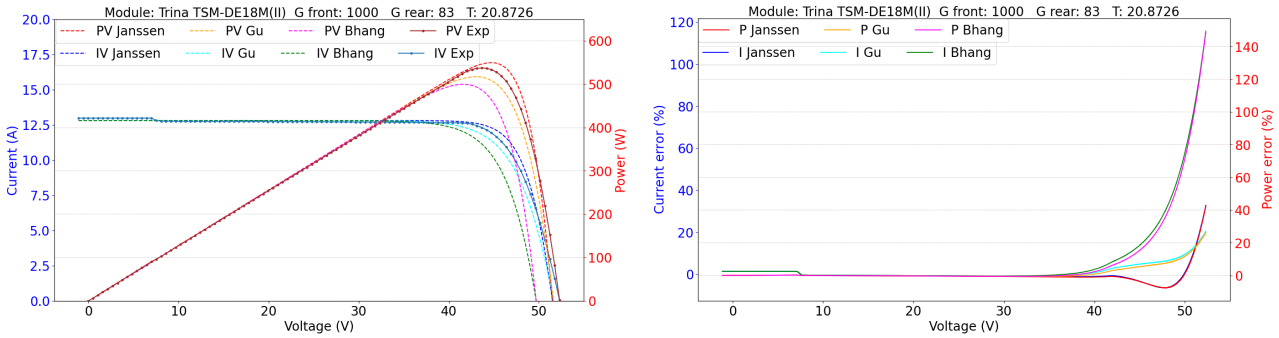

Figure 3.17: IV and PV curves for experimental and modeled data (left) and current and power differences between each model and experimental data (right), illustrated for module Trina TSM-DE18M(II).

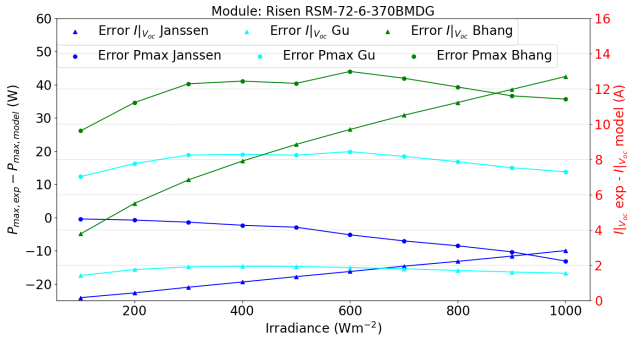

Figure 3.18: Difference between (a) Pmax and (b) current at the last data series point for experimental and modeled data for the Risen RSM-72-6-370BMDG module.

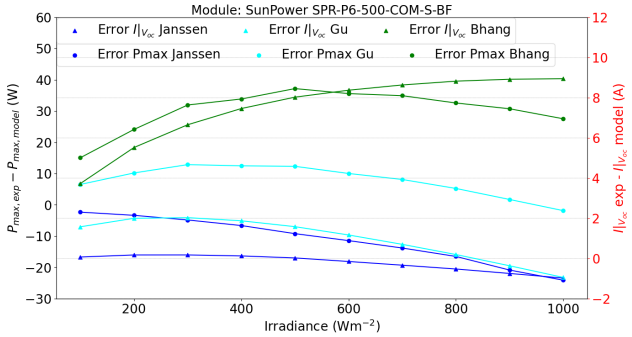

Figure 3.19: Difference between (a) Pmax and (b) current at the last data series point for experimental and modeled data for the SunPower SPR-P6-500-COM-S-BF module.

3.5.2.a Parameters evaluation

Finally, for a comparison with the parameters calculated from each employed model and the actual IV curve, direct parameter extraction is conducted using experimental data obtained from DS measurements. The obtained parameters are shown in Table 3.3. Since Bhang *et al.* model utilizes each set of parameters directly estimated, it will not be analyzed in this section.

Gu *et al.* and Janssen *et al.* use SDM and DDM respectively, each obtained parameter is compared with the corresponding model parameter estimation. Each parameter obtained from direct extraction is evaluated in the IV curve and its respective error when compared with experimental data is calculated and presented in

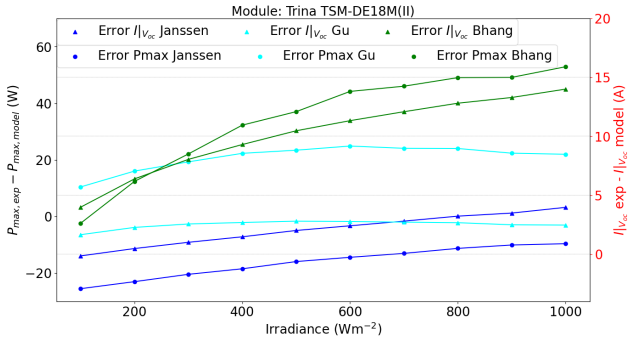

Figure 3.20: Difference between (a) Pmax and (b) current at the last data series point for experimental and modeled data for the Trina TSM-DE 18M(II) module.

Table 3.3: Parameters obtained from every bifacial model employed and compared with direct extraction using SDM and DDM.

Module	Model	I_{ph}	I_{o1}	I_{o2}	R_s	R_{sh}	n_1	n_2
Risen	SDM parameter extraction	10.5943	$8.9835 \cdot 10^{-7}$	-	0.1415	inf	1.62	-
	Gu et al.	10.7488	$9.3922 \cdot 10^{-7}$	-	0.1638	inf	1.61	-
	DDM parameter extraction	10.5943	$2.4945 \cdot 10^{-7}$	$6.4410 \cdot 10^{-7}$	0.1415	inf	1.50	2.20
	Janssen et al.	10.6366	$4.7612 \cdot 10^{-11}$	$1.2335 \cdot 10^{-10}$	0.1285	-	1.00	2.00
Sun Power	SDM parameter extraction	15.5432	$1.2338 \cdot 10^{-6}$	-	0.0120	inf	1.42	-
	Gu et al.	15.6654	$1.1825 \cdot 10^{-6}$	-	0.0146	inf	1.43	-
	DDM parameter extraction	15.5432	$8.7542 \cdot 10^{-7}$	$2.2680 \cdot 10^{-6}$	0.0200	inf	1.40	2.20
	Janssen et al.	15.5987	$1.0311 \cdot 10^{-9}$	$2.6716 \cdot 10^{-9}$	0.0122	-	1.00	2.00
Trina	SDM parameter extraction	12.9789	$4.7242 \cdot 10^{-7}$	-	0.0223	inf	1.65	-
	Gu et al.	12.8143	$8.2291 \cdot 10^{-8}$	-	0.0817	inf	1.50	-
	DDM parameter extraction	12.9789	$2.7752 \cdot 10^{-7}$	$7.1500 \cdot 10^{-7}$	0.0223	inf	1.60	2.20
	Janssen et al.	12.8116	$7.1552 \cdot 10^{-12}$	$1.8538 \cdot 10^{-11}$	0.0759	-	1.00	2.00

Figs. 3.21 to 3.23. It is evident that the errors for both models decreased considerably, considering that Gu *et al.*'s model reached percent errors above 20% and with direct parameter extraction does not exceed 10%. In the case of Janssen *et al.*'s model, using their approximations to obtain the DDM parameters they reached error higher than 75% in the worst case, while the direct DDM extraction, as well as the SDM extraction, does not exceed 10%.

Gu *et al.* and Janssen *et al.* used different methods, SDM and DDM respectively, to get certain parameters. Each parameter obtained was compared with what the models predicted. Then, these parameters are used to trace the modeled IV curve. Then, the percent error for modeled and experimental IV curves are calculated, shown in Figs. 3.21 to 3.23. When direct extraction is applied errors decreased significantly compared to the models' predictions, considering that Gu *et al.*'s model reached percent errors above 20% and with direct parameter extraction does not exceed 10%. In the case of Janssen *et al.*'s model, using their approximations to obtain the DDM parameters they reached error higher than 75% in the worst case, while the direct DDM extraction, as

well as the SDM extraction, does not exceed 10%.

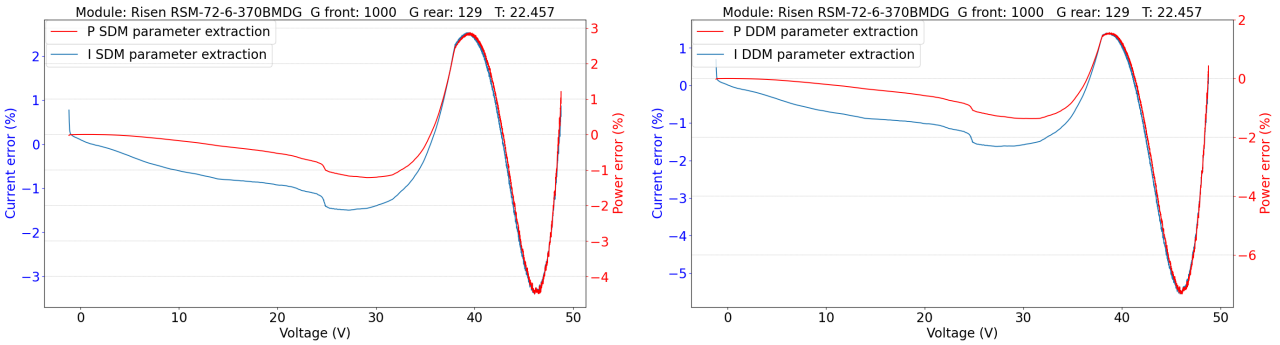

Figure 3.21: IV and PV curves percent error for direct parameter extraction for SDM (left) and DDM (right) for module Risen RSM72-6-370BMDG, considering parameters showed in Table 3.3.

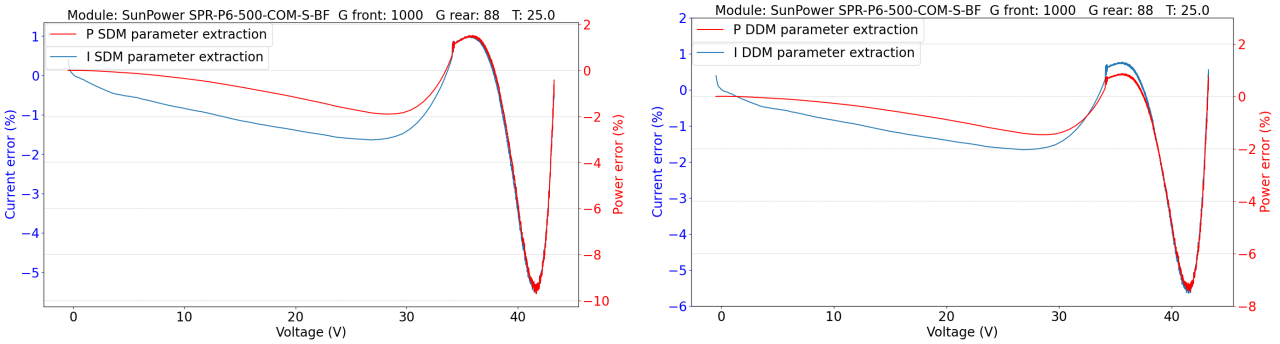

Figure 3.22: IV and PV curves percent error for direct parameter extraction for SDM (left) and DDM (right) for module SunPower SPR-P6-500-COM-S-BF, considering parameters showed in Table 3.3.

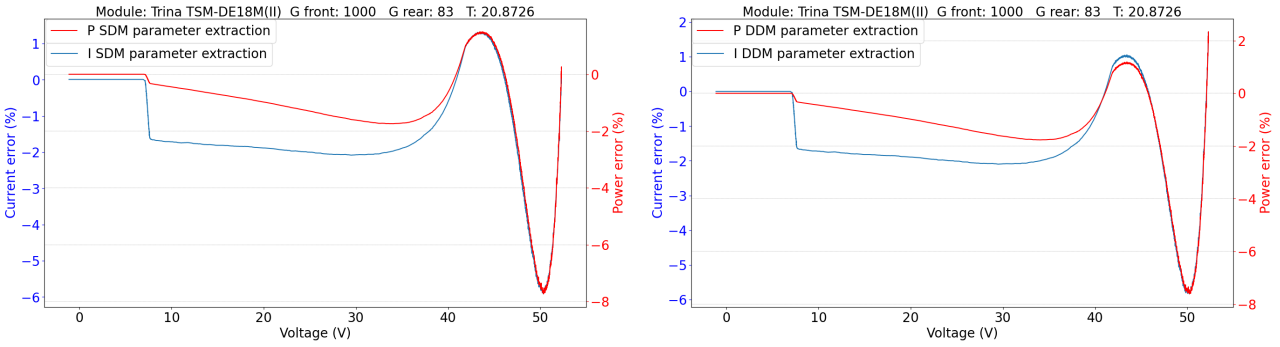

Figure 3.23: IV and PV curves percent error for direct parameter extraction for SDM (left) and DDM (right) for module Trina TSM-DE18M(II), considering parameters showed in Table 3.3.

From the comparison, it seems that the principal problem associated at Janssen *et al.*'s model is their parameter estimation for n_1 and n_2, since they are assumed instead of being calculated. Another difference is the value of I_{o1} and I_{o2}, with 4 magnitude orders of difference. The photocurrent also shows differences, however, they are minimal compared to the effects caused by the use of the other parameters.

On the other hand, since Gu *et al.*'s model is the one that presents the best performance, it will be subjected to a sensibility analysis of its parameters to identify which one has the greatest impact on its error.

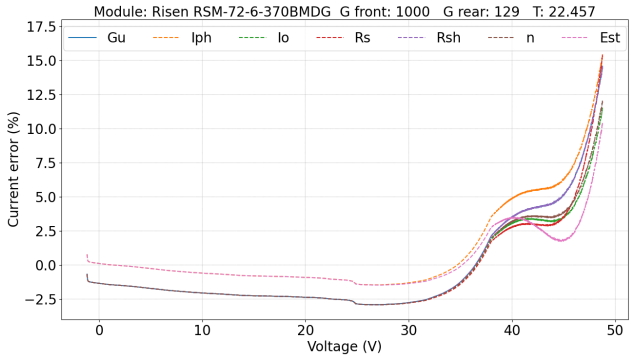

Figure 3.24: Current error when obtained parameters are changed for the estimated SDM parameters for module Risen RSM-72-6-370BMDG.

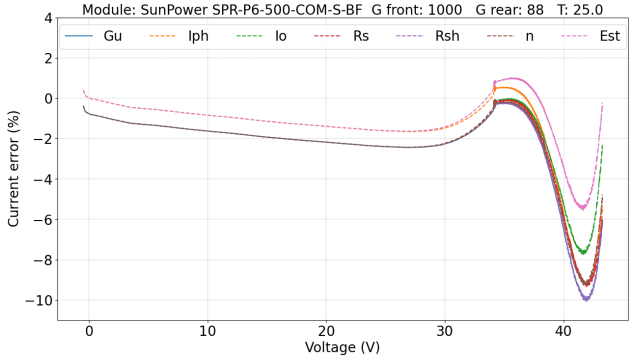

Figure 3.25: Current error when obtained parameters are changed for the estimated SDM parameters for module SunPower SPR-P6-500-COM-S-BF.

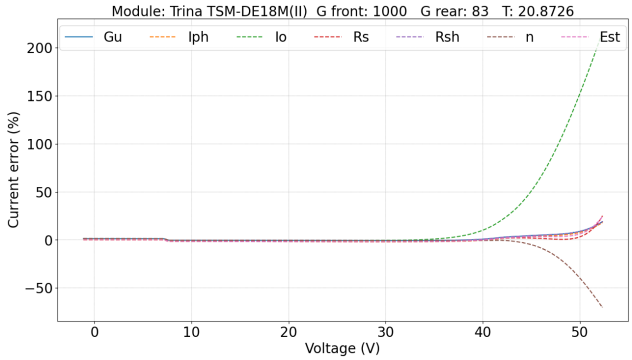

Figure 3.26: Current error when obtained parameters are changed for the estimated SDM parameters for module Trina TSM-DE18M(II).

Figs. 3.24 to 3.26 illustrate various scenarios wherein each parameter, as derived through the method delineated by Gu, is contrasted with those acquired via SDM parameter extraction from experimental IV curve analysis. The designation “Gu” denotes parameters obtained without any alterations, while “Iph” signifies parameters obtained with the substitution of photocurrent values sourced directly from parameter extraction. Similar designations, namely “Io”, “Rs”, “Rsh”, and “n” denote scenarios wherein all parameters remain consistent with those obtained through Gu’s method, except for the specific parameter indicated in the legend, which is substituted with its SDM-extracted counterpart. Notably, the designation “Est” denotes the error observed when all parameters are derived exclusively through SDM parameter estimation.

The figures presented in Figs. 3.24 and 3.25 highlight that the most accurate results were achieved through SDM parameter estimation using experimental IV curves. The influence of I_{ph} variations is most pronounced at the onset of the IV curve, which accounts for the near-zero errors observed in the "Iph" and "Est" cases. Conversely, the "Gu" and "Rsh" scenarios exhibit similar behavior, as they both utilize identical parameters due to R_{sh} resulting in ∞. Subsequently, the most effective substitution leading to minimized errors post SDM parameter estimation involves replacing I_{o}.

The case obtained in Fig. 3.26 behaves differently compared to the previous ones since the replacement of I_{o} and n generated errors that resulted higher than 50% for the case of n and even higher than 200% for the case of I_{o}. Those differences can be caused principally for the impact that those two parameters have in the shape of IV curve, which can be generate differences in V_{oc}.

3.6 Conclusions

The evaluation conducted with SS illumination highlights the significant impact of shadowing induced by frames or junction boxes, not only resulting in elevated errors in current but also manifesting as disparities in V_{oc} when comparing frontal and rear IV curves.

Among the array of models scrutinized in existing literature, the assessment focused on three proposals aimed at determining the optimal fit for IV and PV curves of bifacial PV modules: a single-diode model, a parallel single-diode model, and a double-diode model. Chosen primarily for their replicability, these models were subjected to a meticulous methodology encompassing parameter treatment advocated by each respective author, spanning both frontal and rear sides of the modules to derive the final IV curve. Our evaluation unveiled that the model proposed by Gu et al. yielded the lowest errors, approximately 20% in the worst case. However, efforts to mitigate these errors through direct parameter extraction with SDM revealed notable disparities between estimations. Notably, the parameter with the most pronounced impact was Io, which demonstrated the potential to reduce errors if accurately calculated, as evidenced in the case of SunPower modules, where errors decreased from approximately 10% to 7.5%. Conversely, inaccurate determination of Io, as observed in the case of Trina modules, resulted in errors exceeding 200% when directly extracted I_{o} was replaced.

This research significantly contributes to the literature by offering an evaluation of existing models using data collected under controlled conditions, thereby reducing uncertainty in irradiance and temperature. Furthermore, this analysis identifies the parameters and their respective effects, shedding light on the parameter with the most substantial impact on the curve.

This study suggests two potential avenues for future research. Firstly, there is a need for the evaluation of the same models under outdoor conditions, encompassing diverse temperatures and non-uniform irradiance patterns. Such research would provide insights into model performance under real-world environmental variations. Secondly, there is an opportunity for the development of a novel approach to accurately estimate the requisite parameters, with the aim of minimizing errors in model predictions. This endeavor would contribute to advancing the accuracy and reliability of PV module modeling techniques.

3.7 Aknowledgements

The authors express their gratitude for the financial support from ANID-Fondecyt-11220697. Also, there is financial support from the Scientific Research Initiation Program (PIIC) of the Universidad Técnica Federico Santa María.

Chapter 4

Electrical-Thermal Model for Bifacial Photovoltaic Modules: Comprehensive Validation in Indoor and Outdoor Environments

Note

This article has not yet been submitted to any journal, so it could undergo changes after the publication of this work.

Abstract

This study focuses on enhancing the representation of electrical and thermal models for bifacial photovoltaic modules. Various approaches in existing literature propose improvements, such as incorporating rear irradiance, adjusting resistive parameters and diode currents, and adding series resistances. However, experimental evidence supporting these approaches is often insufficient to demonstrate advantages and address specific limitations. Moreover, most studies concentrate solely on the maximum power point without analyzing the full IV curve, which can reveal shading-induced steps on the IV curve due to the rear side frame in most commercial photovoltaic modules. An electrical-thermal model for bifacial modules is proposed, employing a single diode model for the electrical component. To capture bifacial behavior, parameters for both frontal and rear sides are integrated using rescaling based on irradiances, including ambient condition corrections to derive IV curves and assess power output. For the thermal component, two approaches are employed, culminating in a hybrid model that offers more precise temperature estimates across various conditions. Irradiance estimation utilizes Bifacial Radiance software. Validation of the proposed model involves two main tests. The first employs laboratory measurements using a type A+A+A+ solar simulator to generate IV curves under controlled conditions. Additionally, an outdoor setup includes a vertically oriented, east-west facing bifacial module that continuously monitors irradiance, temperature, voltage, and current. The proposed electrical model showed excellent accuracy in indoor measurements, with maximum current errors of about 3% at peak power, crucial for outdoor evaluations. However, factors like reflections, clouds, and shadows from module frames can significantly impact results.

Keywords: Bifacial module, PV modeling, outdoor measurement, indoor measurement

4.1 Introduction

Bifacial photovoltaic (bPV) technology offers several advantages over traditional monofacial photovoltaic (mPV) technology, leading to increased power generation. bPV modules capture sunlight from both the front and back surfaces, significantly boosting overall electricity production. This technology performs particularly well under high albedo conditions, as the reflectance of white tiles, white pebbles, desert sand or snow on the ground can contribute to power generation [48, 49, 50]. Additionally, bPV modules provide greater flexibility in terms of installation direction and location.

Key factors influencing bPV energy production include tilt angle, elevation, ground albedo, and azimuth angle [51, 52, 53]. Studies have shown that bifacial modules can outperform monofacial ones when normalized for Standard Test Conditions (STC) on the front side, especially in tilted configurations similar to traditional solar panels [54]. Based on the research conducted by [55], bPV shows advantages into different scenarios, considering sunny and cloudy days, and especially under low irradiances.

To achieve realistic estimations of energy production, various models have been developed to represent the bifacial behavior, encompassing optical, thermal, and electrical aspects. The primary challenge in optical modeling for bPV is accurately representing rear-side irradiance. Two main methods have been developed for this purpose: the view factor model and the ray tracing model [56]. The view factor model has been extensively studied [57, 58, 26], while the ray tracing model, primarily used in software such as RADIANCE [59], TracePro [60], and Ray Optics [61], has been examined by [25].

Thermal modeling is also crucial, as it plays a significant role in estimating efficiency due to the inverse linear correlation between temperature and efficiency. Research indicates that the temperature of bPV devices tends to be higher than that of mPV under high irradiance and lower under low irradiance [55]. Although higher irradiance results in higher temperatures, the energy yield in bPV is greater due to increased short-circuit current levels [62]. Aly et al. [63] developed a thermal model that considers irradiance, ambient temperature, wind speed, and installation characteristics to estimate cell temperature, assuming that only PV cells absorb incident irradiance while other layers do not.

These models are essential for recreating the environmental conditions to which the module is exposed, providing critical input information for accurately estimating power output through the electrical model. The electrical model's accuracy in calculating maximum power output is crucial for efficient plant sizing and production optimization. In the literature, most models are based on traditional mPV formulations, such as single- and double-diode models, with adaptations to represent bifacial behavior [26, 34, 33, 27, 28, 64]. These models focus on various features, from IV curves to maximum power output.

The characterization of bifacial photovoltaics has garnered extensive attention due to the added complexity of generating electricity from both sides of the module exposed to light. Measurement methods vary, ranging from indoor setups with sun simulators to outdoor exposure conditions. Indoor procedures typically employ single side and double side illumination methods. In the former, each side is illuminated separately, with the opposite side covered to prevent parasitic reflections, as discussed in [43]. The latter method uses two sun simulators simultaneously for commercial modules, or employs mirror arrangements for mini modules composed of four cells.

Indoor studies emphasize the importance of bifacial irradiation measurements and caution against extrapolating indoor characterizations to outdoor conditions. For instance, [42] focuses on single side measurements and references the standard IEC TS 60904-1-2, which recommends frontal illumination with the rear side covered. This setup was used to quantify reflection effects on bifacial PV modules, highlighting how irradiance non-uniformity impacts fill factor and maximum power. Recommendations from both the standard and the study include using a black backside to minimize reflections.

Outdoor characterization, on the other hand, involves numerous factors such as background variations [53], tilt angle changes [65], and environmental parameters like different irradiances, wind speed, shadowing, and albedo. Consequently, outdoor setups typically incorporate pyranometers for Plane of Array (POA) irradiance measurement, solar monitoring systems, temperature sensors, and data loggers [55, 35].

The aim of this study is to propose a model that accurately represents the behavior of IV curves under both indoor and outdoor conditions, including the maximum power point (MPP) during continuous monitoring in

a vertical E-W configuration. To achieve this goal, indoor and outdoor measurements were conducted. Indoor measurements involved precise IV curve tracing under controlled conditions, ensuring highly reliable data. In contrast, outdoor measurements considered realistic environmental effects, providing a comprehensive assessment of the model's performance. The model integrates irradiance estimation and electrical-thermal modeling to derive IV curves from environmental data. This approach enables the estimation of output power without the need for direct measurement on the studied device, relying instead on data from meteorological stations.

This comprehensive approach ensures thorough characterization under various conditions, enhancing the understanding of bPV module performance across indoor and outdoor environments. The study is structured as follows: first, a review of the state of the art is presented to highlight relevant evidence on bifacial photovoltaic modeling. Next, the proposed model is described, detailing both the electrical and thermal approaches. The methodology section then elaborates on the setup and data processing for both indoor and outdoor measurements. Finally, the results and conclusions are presented, summarizing the findings and implications of the study.

4.2 Bifacial photovoltaic models

4.2.1 Thermal model

Thermal modeling plays a critical role in estimating operational voltages, IV curves, and power outputs of photovoltaic devices. Temperature significantly impacts these parameters, as extensively reviewed in [66]. Accurate temperature estimation is crucial due to factors such as ground reflectivity, temperature, material properties, and installation conditions [24]. Several models have been proposed to address this, including the Sandia model, NOCT model, PVsyst model, Heat transfer models, Empirical formulae, Kutzer model, and Castillo model [56].

[33] introduced a thermal model specifically for bifacial PV devices, requiring inputs of ambient temperature and wind speed. This model, based on an energy balance approach similar to the PVSyst model, incorporates parameters related to both front and rear irradiances, as illustrated in Equation 4.1.

$$U_{\text{bif}}\ (T_{\text{bif}} - T_{\text{amb}}) = \alpha(G_{\text{F}} + G_{\text{R}})(1 - \eta_{\text{bif}}) \tag{4.1}$$

The thermal conductivity values (U_{bif} or U_{mono}) are critical parameters determined by the specific characteristics of the front and rear glass, as well as the module's installation method.

In another significant study, [26] designed an equivalent thermal circuit to represent bPV modules, defining an equivalent thermal resistance for every layer. By solving a system of five equations, showed in Eqs. (4.2) to (4.6), the model calculates the temperatures across these layers using inputs such as front and rear irradiances, as well as ambient temperature.

$$C_{\text{p,g}}\delta_{\text{g}}A\rho_{\text{g}}\frac{dT_{\text{g}}}{dt} = \alpha_{\text{g}}G_{\text{F}}A + \frac{T_{\text{EVA1}} - T_{\text{g}}}{R_{\text{EVA1-g}}} - \frac{T_{\text{g}} - T_{\text{a}}}{R_{\text{conv,g}}} - \frac{T_{\text{g}} - T_{\text{sky}}}{R_{\text{rad,g}}} \tag{4.2}$$

$$C_{\text{p,EVA}}\delta_{\text{EVA}}A\rho_{\text{EVA}}\frac{dT_{\text{EVA1}}}{dt} = \frac{T_{\text{PV}} - T_{\text{EVA1}}}{R_{\text{PV-EVA1}}} - \frac{T_{\text{EVA1}} - T_{\text{g}}}{R_{\text{EVA1-g}}} \tag{4.3}$$

$$C_{\text{p,PV}}\delta_{\text{PV}}A\rho_{\text{PV}}\frac{dT_{\text{PV}}}{dt} = (\tau_{\text{g}}G_{\text{r}}A - P_{\text{PV}}) - \frac{T_{\text{PV}} - T_{\text{EVA1}}}{R_{\text{PV-EVA1}}} - \frac{T_{\text{PV}} - T_{\text{EVA2}}}{R_{\text{PV-EVA2}}} \tag{4.4}$$

$$C_{\text{p,EVA}}\delta_{\text{EVA}}A\rho_{\text{EVA}}\frac{dT_{\text{EVA2}}}{dt} = \frac{T_{\text{PV}} - T_{\text{EVA2}}}{R_{\text{PV-EVA2}}} - \frac{T_{\text{EVA2}} - T_{\text{g}}}{R_{\text{EVA2-g}}} \tag{4.5}$$

$$C_{\text{p,g}}\delta_{\text{g}}A\rho_{\text{g}}\frac{dT_{\text{rg}}}{dt} = \alpha_{\text{g}}G_{\text{R}}A + \frac{T_{\text{EVA2}} - T_{\text{rg}}}{R_{\text{EVA1-rg}}} - \frac{T_{\text{rg}} - T_{\text{a}}}{R_{\text{conv,rg}}} - \frac{T_{\text{rg}} - T_{\text{grd}}}{R_{\text{rad,rg}}} \tag{4.6}$$

The parameters used in the equations are defined as follows: C_p denotes specific heat, δ represents thickness, ρ stands for density, τ signifies transitivity, α indicates absorptivity, G_F and G_R denote front and rear irradiances respectively, G_r represents received irradiance (sum of front and rear irradiances), A denotes area, T stands for temperature, and t represents time.

Subscripts denote specific materials: g refers to glass (front glass as g, rear glass as rg), EVA denotes encapsulant (upper EVA as EVA1, lower EVA as EVA2), and PV corrrespond to photovolaic cells.

Thermal resistances (R) are categorized into radiative, convective, and conductive types. Radiative resistances occur only in external layers, such as glass, and are calculated using Equation 4.7.

$$R_{\mathrm{rad,x}} = \frac{1}{h_{\mathrm{rad,x}} A} \tag{4.7}$$

Here, x can represent g or rg for front and rear glass respectively, where $h_{\mathrm{rad,x}}$ denotes the radiative heat coefficient specific to each surface, as defined by Eqs. (4.8) and (4.9).

$$h_{\mathrm{rad,g}} = \epsilon_\mathrm{g} \sigma (T_{\mathrm{sky}}^2 + T_\mathrm{g}^2)(T_{\mathrm{sky}} + T_\mathrm{g}) \tag{4.8}$$

$$h_{\mathrm{rad,rg}} = \epsilon_\mathrm{g} \sigma (T_{\mathrm{grd}}^2 + T_{\mathrm{rg}}^2)(T_{\mathrm{grd}} + T_{\mathrm{rg}}) \tag{4.9}$$

Convective resistances also occur in external layers and are defined by Eq. (4.10).

$$R_{\mathrm{conv,g}} = R_{\mathrm{conv,rg}} = \frac{1}{h_{\mathrm{conv,x}} A} \tag{4.10}$$

The convective heat transfer coefficient $h_{\mathrm{conv,x}}$ for both front (g) and rear (rg) glasses is given by Eq. (4.11).

$$h_{\mathrm{conv,g}} = h_{\mathrm{conv,rg}} = 2.8 + 3.0u \tag{4.11}$$

Finally, conduction occurs between adjacent layers, resulting in conductive thermal resistances defined by Eq. (4.12).

$$R_{\mathrm{i\text{-}j}} = \frac{\delta_\mathrm{i}}{2\lambda_\mathrm{i} A_\mathrm{i}} + \frac{\delta_\mathrm{j}}{2\lambda_\mathrm{j} A_\mathrm{j}} \tag{4.12}$$

Where subscripts i and j refer to the layers, as exemplified in Eq. (4.2) with $R_{\mathrm{EVA1\text{-}g}}$, representing the thermal resistance between EVA1 and front glass. Here, λ denotes the thermal conductivity of the respective layers.

A widely used thermal model, proposed by Faiman [67], establishes a linear correlation between irradiance and module temperature, expressed in Eq. (4.13).

$$T_{\mathrm{mod}} = T_{\mathrm{amb}} + \frac{G_{\mathrm{POA}}}{U_0 + U_1 \cdot u} \tag{4.13}$$

Where T_{mod} is the module temperature, T_{amb} is the ambient temperature, G_{POA} is the irradiance in the plane of array, U_0 is a constant heat transfer component, U_1 is the convective heat transfer component, and u represents the wind speed.

Studies evaluating Faiman's thermal model in the context of bifacial devices [68, 69] have demonstrated its effectiveness in various applications.

4.2.2 Electrical model

Electrical models for photovoltaic (PV) devices have been extensively developed, primarily for monofacial modules. These models typically include approaches such as the single-diode and double-diode models, both based on equivalent electrical circuits comprising a current source, one or two diodes in parallel (depending on the model), a shunt resistance, and a series resistance. The single-diode model is widely adopted in literature due to its simplicity in parameter estimation, whereas the double-diode model offers improved accuracy, particularly under low irradiance conditions [23].

For bPV devices, researchers have employed various strategies to capture bifacial behavior. A common approach involves integrating two current sources into the base model, one for each side, whether employing a single-diode or double-diode framework [24, 34, 26, 33]. Other representations include dual branches in parallel, often based on the single-diode model [27, 25]. The fundamental equations for both models are presented in Eqs. (4.14) and (4.15).

$$I_{\mathrm{pv}} = I_{\mathrm{ph,f}} + I_{\mathrm{ph,r}} - I_{\mathrm{s}} \left[\exp\left(\frac{V_{\mathrm{pv}} + I_{\mathrm{pv}} \cdot R_{\mathrm{s}}}{N_{\mathrm{s}} \cdot V_{\mathrm{t}} \cdot n} \right) - 1 \right] - \frac{(V_{\mathrm{pv}} + I_{\mathrm{pv}} \cdot R_{\mathrm{s}})}{R_{\mathrm{sh}}} \tag{4.14}$$

$$I_{\mathrm{pv}} = I_{\mathrm{ph,f}} + I_{\mathrm{ph,r}} - I_{\mathrm{s1}} \left[\exp\left(\frac{V_{\mathrm{pv}} + I_{\mathrm{pv}} \cdot R_{\mathrm{s}}}{N_{\mathrm{s}} \cdot V_{\mathrm{t}} \cdot n_1} \right) - 1 \right] - I_{\mathrm{s2}} \left[\exp\left(\frac{V_{\mathrm{pv}} + I_{\mathrm{pv}} \cdot R_{\mathrm{s}}}{N_{\mathrm{s}} \cdot V_{\mathrm{t}} \cdot n_2} \right) - 1 \right] - \frac{V_{\mathrm{pv}} + I_{\mathrm{pv}} \cdot R_{\mathrm{s}}}{R_{\mathrm{sh}}} \tag{4.15}$$

Bifacial electrical modeling has been approached from various angles in research. One perspective involves direct IV curve analysis, as explored by [34]. This study introduces modifications to both single-diode and double-diode models by incorporating a new series resistance scaled by a bifacial factor. The findings suggest that the proposed model enhances accuracy and effectiveness across different operational conditions.

Another significant approach examines bPV performance through power generation analysis, exemplified in [35]. Here, arrays of bifacial modules were evaluated under varying albedos using measurements of climate parameters (solar irradiance, temperature, humidity, wind speed) and electrical parameters (voltage, current). This data facilitated the calculation of DC power output throughout extended periods. Similarly, [53] calculated maximum power considering escalation in irradiance and temperature, described by Eq. (4.16).

$$P_{\mathrm{max}} = P_{\mathrm{max,ref}} \frac{(G_{\mathrm{F}} + \phi G_{\mathrm{R}})}{G_{\mathrm{T,ref}}} [1 + \gamma (T_{\mathrm{c}} - 25)] \tag{4.16}$$

Their evaluation considered various background albedos, concluding that cement can increase production but exhibits poorer performance compared to materials like DQ waterproof roll.

In [33], a comprehensive approach was taken using a double-diode model integrated with optical and thermal models to predict the DC output of bifacial modules. Key inputs to the model include Global Horizontal Irradiance (GHI), Diffuse Horizontal Irradiance (DHI), ambient temperature T_{a}, and wind speed u. To accurately represent the bifacial behavior, the authors proposed an extended parameter set including I_{sc}, I_{s1}, I_{s2} and R_{s}, detailed in Eqs. (4.17) and (4.18).

$$I_{\mathrm{T,sc}} = \frac{I_{\mathrm{F,sc}} G_{\mathrm{F}} + I_{\mathrm{R,sc}} G_{\mathrm{R}}}{G_{\mathrm{STC}}} \tag{4.17}$$

$$X = \frac{X_{\mathrm{F}} G_{\mathrm{F}} + X_{\mathrm{R}} G_{\mathrm{R}}}{G_{\mathrm{F}} + G_{\mathrm{R}}} \tag{4.18}$$

4.3 Proposed model

An electrical and thermal model are employed and optimized to predict the power output of a vertically oriented bifacial module facing east-west. The electrical model's validation includes indoor measurements of IV curves

and its application to calculate the module's power output under real conditions. Meanwhile, the thermal model's accuracy is evaluated through direct comparison with experimental data. Additionally, irradiance estimation is performed using Bifacial Radiance software [70].

4.3.1 Electrical model

Regarding the electrical model, it is based in the single diode model, as shown in Fig. 4.1.

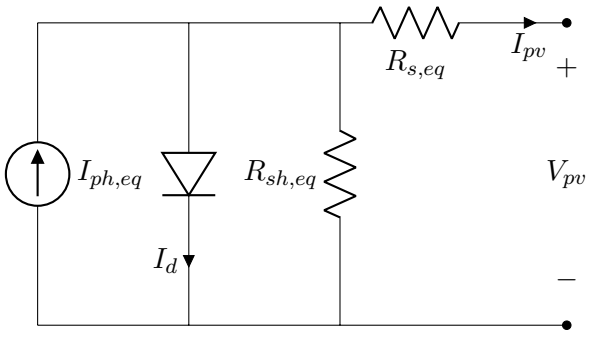

Figure 4.1: Single diode model adapted for bifacial PV devices.

One challenge in applying the electrical bifacial model is accurately estimating its five key parameters: $I_{\mathrm{ph,eq}}$, n, I_{s}, R_{s} and R_{sh}.

To determine these parameters, IV curves are traced under Standard Test Conditions (STC), and four critical points are extracted: I_{sc}, I_{mpp}, V_{oc} and V_{mpp}, for both the front and rear sides of the module. These values serve as input for parameter estimation using a W-Lambert function. The estimation process yields a total of 10 parameters, with 5 corresponding to each side. This approach aims to obtain equivalent parameters required for the model.

$$I_{\mathrm{ph,eq}} = \frac{(I_{\mathrm{ph,f}} \cdot G_{\mathrm{f}} + I_{\mathrm{ph,r}} \cdot G_{\mathrm{r}})}{G_{\mathrm{stc}}} + \frac{\alpha}{100} \cdot (T_{\mathrm{k}} - T_{\mathrm{ref}}) \tag{4.19}$$

$$I_{\mathrm{s,eq}} = \frac{(I_{\mathrm{o,f}} \cdot G_{\mathrm{f}} + I_{\mathrm{o,p}} \cdot G_{\mathrm{p}})}{G_{\mathrm{f}} + G_{\mathrm{p}}} \cdot \left(\frac{Tk}{Tref}\right)^3 \cdot \exp\left(\frac{q \cdot Eg}{k} \cdot \left(\frac{1}{Tref} - \frac{1}{Tk}\right)\right) \tag{4.20}$$

$$R_{\mathrm{s,eq}} = \frac{R_{\mathrm{s,f}} \cdot G_{\mathrm{f}} + R_{\mathrm{s,r}} \cdot G_{\mathrm{p}}}{G_{\mathrm{stc}}} \tag{4.21}$$

$$R_{\mathrm{sh,eq}} = \frac{R_{\mathrm{sh,f}} \cdot G_{\mathrm{f}} + R_{\mathrm{sh,r}} \cdot G_{\mathrm{r}}}{G_{\mathrm{stc}}} \tag{4.22}$$

$$n_{\mathrm{eq}} = \frac{n_{\mathrm{f}} \cdot G_{\mathrm{f}} + n_{\mathrm{p}} \cdot G_{\mathrm{p}}}{G_{\mathrm{f}} + G_{\mathrm{r}}} \tag{4.23}$$

This parameter treatment is derived from proposals by Janssen *et al.* [33] and Gu *et al.* [26]. It involves rescaling parameters as suggested by Janssen *et al.*, along with implementing Gu's temperature correction for I_{s}.

4.3.2 Thermal model

Two thermal models are applied to simulate the temperatures on the module's surface. The first model follows Gu et al.'s formulation, detailed in Eqs. (4.2) to (4.6). Adjustments are made considering the module's orientation and setup, particularly in relation to ground and sky temperatures. Since the module is vertically oriented, both sky and ground temperatures are approximated as ambient temperature, as expressed in Eq. (4.24).

$$T_{\text{sky}} = T_{\text{ground}} = T_{\text{ambient}} \tag{4.24}$$

Because the equations are time-dependent, initial conditions and a stabilization time are required. Given that Bifacial Radiance provides hourly data, initial temperatures at each point are set to the last recorded temperature, with a stabilization time of 3600 seconds.

The second model utilized is Faiman's proposal, as previously defined in Equation 4.13. The coefficients U_0 and U_1 are estimated through empirical linear regression, where the y-axis is $G_{\text{POA}}/(T_{\text{amb}} - T_{\text{mod}})$ and the x-axis is wind speed. Using continuous monitoring data, empirical regression is applied to estimate these coefficients.

Regarding G_{POA}, it is calculated as the sum of frontal and rear irradiances, as described in Eq. (4.13).

$$G_{\text{POA}} = G_{\text{f}} + G_{\text{r}} \tag{4.25}$$

4.4 Methodology

4.4.1 Setup

Two main tests are conducted to evaluate the proposed model. The first test is conducted under indoor conditions using an A+A+A+ Sun Simulator, which enables the tracing of IV curves under controlled irradiance and temperature settings. The second test takes place outdoors using a vertically oriented module facing east-west.

4.4.1.a Bifacial modules

Table 4.1 presents the modules used for indoor and outdoor IV curve tracing. All modules are from PERC+ technology and are evaluated in the indoor setup. Specifically, the Risen module is assessed in both indoor and outdoor environments.

Table 4.1: Modules for indoor IV curve tracing and outdoor monitoring and their respective datasheet parameters.

Manufacturer	Model	Technology	P_{max} (W)	I_{sc} (A)	V_{oc} (V)	I_{mpp} (A)	V_{mpp} (V)	Test
Trina	TSM-DEG18MC.20(II)	PERC+	490	12.05	51.10	11.45	42.80	Indoor
SunPower	SPR-P6-500-COM-S-BF	PERC+	500	14.71	43.20	13.82	36.20	Indoor
Risen	RSM72-6-370-BMDG	PERC+	370	9.90	48.15	9.35	39.60	Indoor Outdoor

4.4.1.b Indoor setup

The IV curves are measured using an A+A+A+ Sun Simulator, as depicted in Fig. 4.2. Bifacial illumination is achieved by employing a 90% reflective film on the rear face of the bifacial module Fig. 4.3.

In this experimental setup, irradiance on both the front and rear sides of a solar module is measured. The frontal irradiance is controlled using the Sun Simulator software and monitored with a dedicated cell. For the rear irradiance, light is reflected off a reflective surface and measured using a reference cell.

The measurement process consists of two stages. In the first stage, irradiance is measured at various points across the module to determine the irradiance non-uniformity. The module's surface is divided into nine sections, with the reference cell positioned in each section to capture variations in irradiance due to the reflected light. This stage helps identify the minimum level of irradiance on the module, which is used to adjust the model applied afterward.

Figure 4.2: A+A+A+ sun simulator used for indoor measurements.

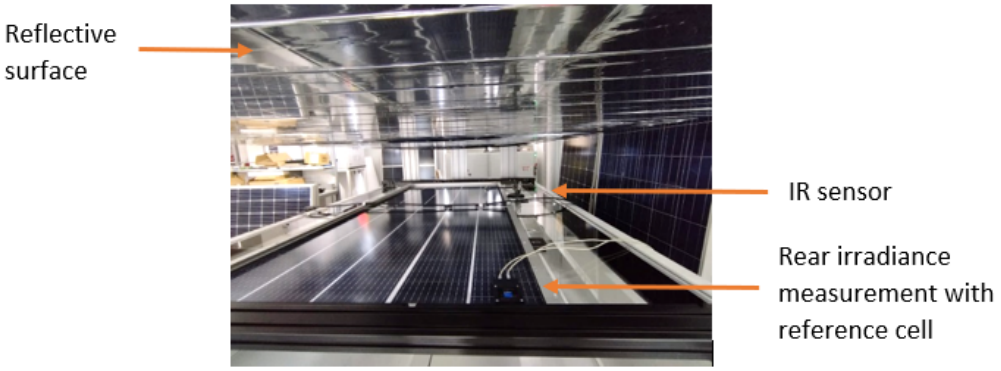

Figure 4.3: Sun simulator with elevated cabin and a reflective film in its surface.

In the second stage, the reference cell is moved outside the module to trace the IV curve. This repositioning helps avoid any shading effects caused by the measurement device. Additionally, temperature is measured using an infrared (IR) sensor to account for its impact on the readings.

4.4.1.c Outdoor setup

In this case the Risen module is installed in a vertical configuration with east-west orientation, as depicted in Fig. 4.4.

Electrical variables and ambient conditions are monitored using a Campbell Granite 6 data logger. Current is measured with a shunt resistor, while voltage is measured using a voltage divider setup, as illustrated in Fig. 4.5. Ambient conditions are monitored with a Campbell Pt-1000 Class A, Back-of-Module Temperature Sensor positioned at the center of the rear surface, with wiring covering less than 10% of the cell area, adhering to recommendations for bifacial modules outlined in the standard IEC 61724-1 [71]. Irradiance levels are measured with four pyranometers positioned at the top and bottom of both frontal and rear surfaces of the module, as depicted in Fig. 4.6. Additionally, a meteorological station located in the same area as the setup registers GHI, DHI, DNI, wind speed, ambient temperature, UVA, and UVB radiations.

The evaluated data spans from January 24th to March 19th, covering a total of eight weeks.

Figure 4.4: Outdoor setup (left) vertical module oriented east-west and (right) close-up of temperature sensor and pyranometers installed on the rear surface.

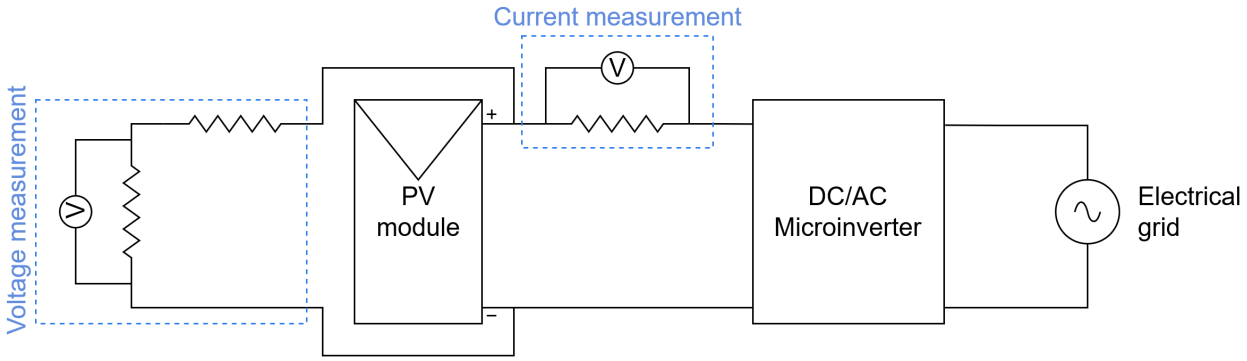

Figure 4.5: Electrical circuit employed to measure voltage and current.

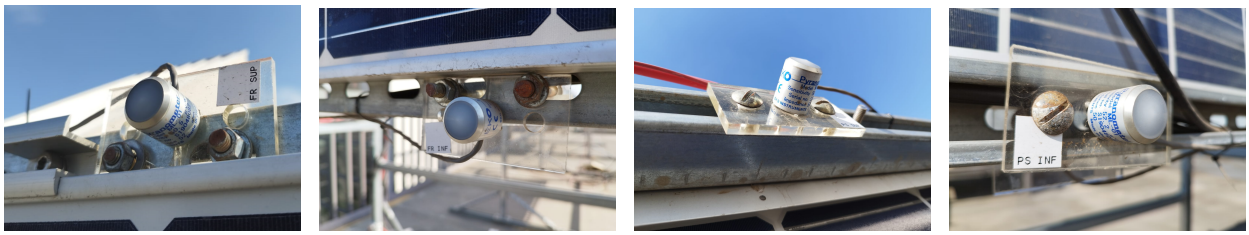

Figure 4.6: Four pyranometers for frontal and rear irradiance measurement.

4.4.2 Data processing

4.4.2.a Indoor measurements

IV curves obtained from the indoor sun simulator under STC conditions for each side of the module are used to extract key values: I_{sc}, V_{oc}, I_{mpp}, and V_{mpp} for both the frontal and rear sides of each module. The same procedure is repeated with the raised cabin setup, illuminating both sides of the module.

Using these key values, the W-Lambert function is applied to estimate parameters for the Single-Diode Model (SDM), resulting in the following data:

- Frontal estimated parameters: $I_{\mathrm{ph,f}}$, $I_{\mathrm{o,f}}$, $R_{\mathrm{s,f}}$, $R_{\mathrm{sh,f}}$, n_{f}
- Rear estimated parameters: $I_{\mathrm{ph,r}}$, $I_{\mathrm{o,r}}$, $R_{\mathrm{s,r}}$, $R_{\mathrm{sh,r}}$, n_{r}
- Bifacial illumination estimated parameters: $I_{\mathrm{ph,b}}$, $I_{\mathrm{o,b}}$, $R_{\mathrm{s,b}}$, $R_{\mathrm{sh,b}}$, n_{b}

Using the data obtained from each side of the module, the proposed model is applied to generate IV curves. These generated IV curves are then compared against IV curves generated using the estimated bifacial parameters and direct experimental IV curves, as depicted in Fig. 4.7.

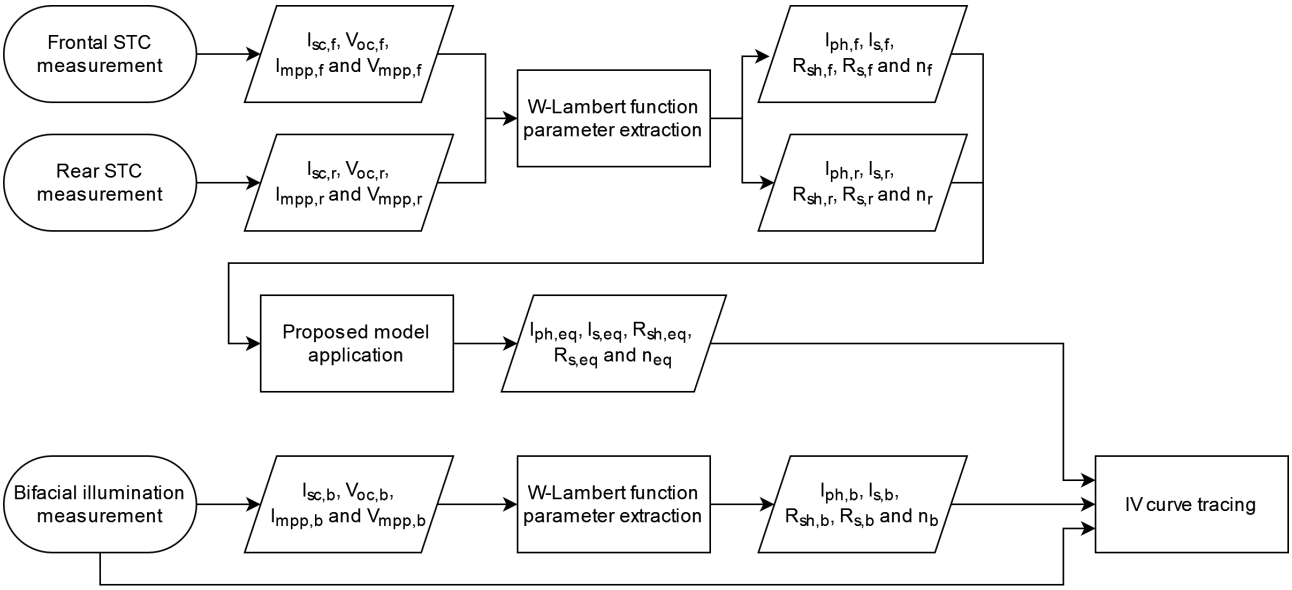

Figure 4.7: Indoor data processing explanation scheme.

4.4.2.b Outdoor measurements

- **Irradiance estimation**

  The first step involves irradiance estimation using Bifacial Radiance [70] software. This software utilizes Typical Meteorological Year (TMY) data along with installation specifics such as module size, orientation, albedo, date, and location coordinates. It calculates the irradiance incident on the module from both the frontal and rear sides at various points across its surface. The data used to recreate the module features are: latitude -33.49, longitude -70.62, 90° inclination, and 90° azimuth.

  The estimated irradiances are compared with experimentally measured irradiances. It was observed that the software tends to underestimate the actual values. Therefore, a correction factor is empirically estimated to achieve more accurate irradiance estimates. This correction factor is determined by minimizing the squared error between the estimated and measured results and is applied to all the data. Since the curves for frontal and rear pyranometers differ, two correction factors are determined to minimize the squared error for each side.

  Estimated irradiances from the software are defined at specific points on the test module. To compare these estimations with real data, the same locations are used, namely, the top and bottom of the module for both the frontal and rear sides, each located at the center of the module.

  Once the estimated irradiances are obtained, the minimum value for each side of the module is used in the thermal and electrical models. This consideration is made because the short circuit current is limited by irradiance.

- **Thermal model**

  The thermal model is applied using two different approaches:

1. Gu's Model: This model utilizes a system of five differential equations to estimate the temperatures in each layer of the module.
2. Faiman's Model: This model employs a linear fit to estimate the temperature.

Both models take ambient temperature, irradiance, and wind speed as inputs. An error analysis is conducted by comparing the estimated temperatures from both models with the actual measured temperatures.

- **Electrical model**

  Finally, the estimated irradiance and temperature are used as inputs to an electrical model. This model also incorporates parameters estimated from indoor Standard Test Condition (STC) characterization. Using this data, the power output is estimated and then compared with the real measured power output.

  All the processes are described in Fig. 4.8.

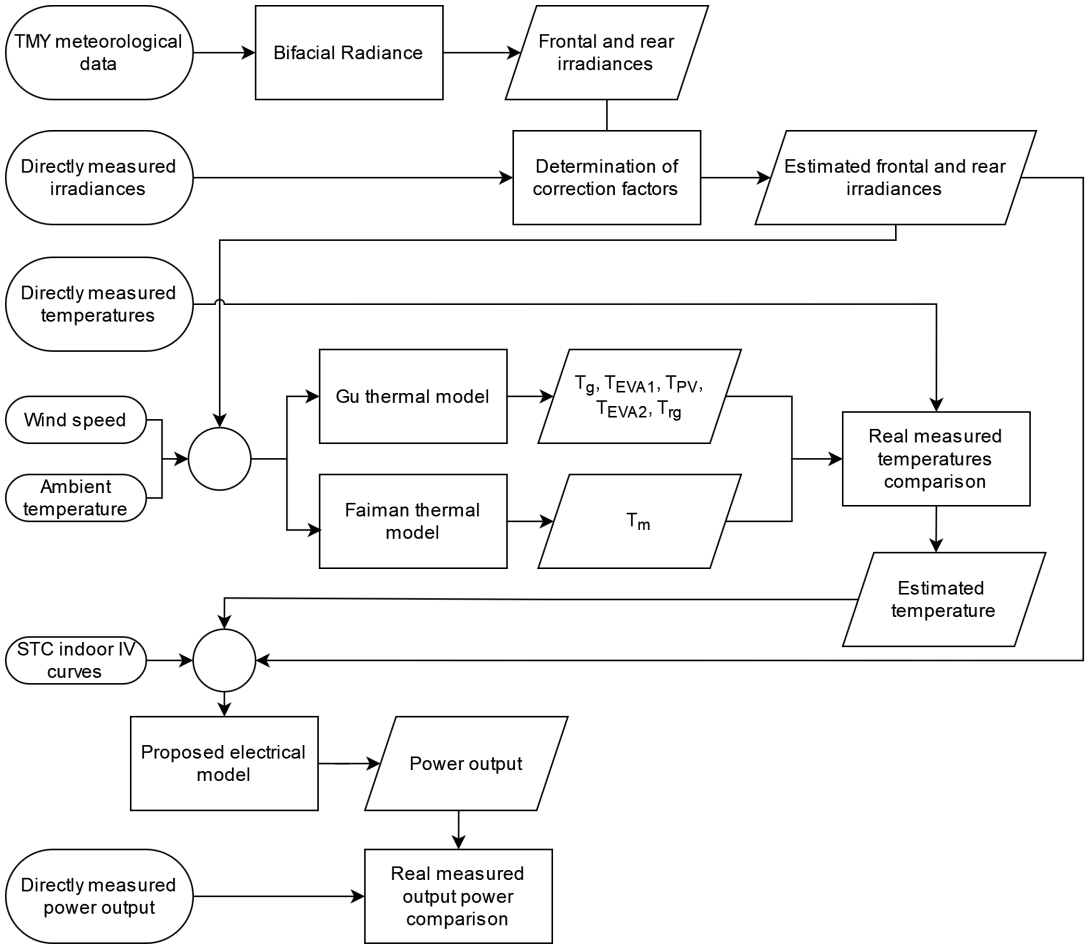

Figure 4.8: Oudoor data processing explanation scheme.

4.5 Results and discussion

4.5.1 Irradiances

Using meteorological data, irradiances are estimated with Bifacial Radiance software, resulting in hourly resolution data. The correction factors, determined as mentioned in Section 4.4.2.b, are 1.16 for the front side and 1.07 for the rear side. These factors are applied to generate Fig. 4.9, which corresponds to the 5th week of

collected data. This specific range is chosen because February 22nd was a rainy day, resulting in significantly lower irradiances compared to the other days under monitoring.

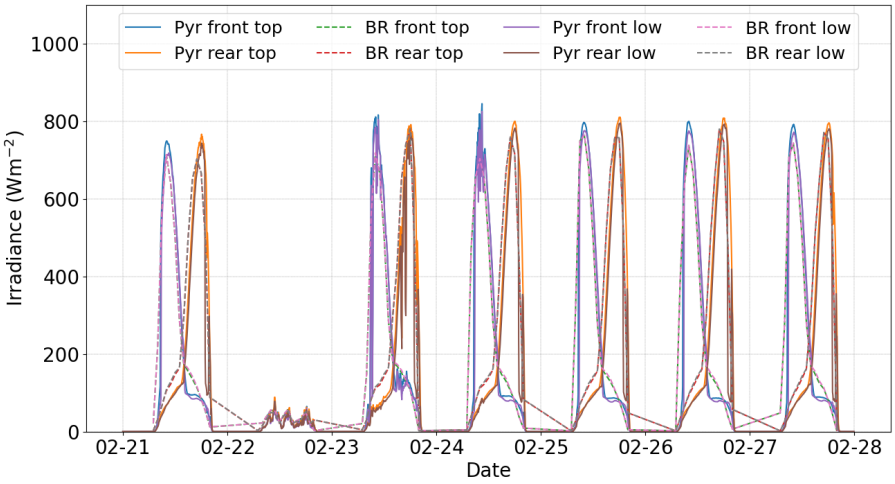

Figure 4.9: Measured and modeled irradiances using Bifacial Radiance after applying the correction factor.

The results clearly demonstrate how irradiance varies on each side of the module based on its orientation. The front side reaches its peak irradiance in the morning, while the rear side peaks in the evening. Around midday, the module experiences the lowest irradiance values on a sunny day.

However, due to the hourly resolution of the data, the model does not capture irradiance variations caused by clouds, like the observed on February 23rd and 24th. This limitation is important to consider when evaluating both electrical and thermal models.

On February 22nd, the irradiance estimation appears to be accurate, indicating no significant issues.

It is important to note that the data only includes sunlight hours, approximately from 7 AM to 9 PM. This is why interpolation lines appear during the night in the irradiance plot, as no data is recorded during these hours.

To analyze the behavior of the module over the complete measurement period, an error analysis is performed. Fig. 4.10 shows the RMSE calculated for each sensor located on the module. The error for frontal and rear irradiances varies depending on the time of day. Frontal irradiance shows higher errors until 12 PM, while rear irradiance shows higher errors from 4 PM onwards. Between 1 PM and 3 PM, the errors are more evenly distributed. During extreme hours, each side of the irradiance estimation tends to have higher RMSE for the lower pyranometer. This behavior could be explained by the overestimation of irradiance at the beginning of the day, as seen in Fig. 4.9, which is primarily affected by the shadowing effect of mountains to the east and west.

4.5.2 Thermal model

Gu and Faiman models are implemented using irradiances, wind speed and ambient temperature as input. The resulting temperatures are shown in Fig. 4.11, which utilizes the same period for estimation as the irradiance model. This allows for an in-depth analysis of its performance, particularly under varying irradiance conditions such as those on rainy days, where irradiance is low.

It has been observed that Gu model tends to underestimate temperatures in these conditions. When irradiance levels are higher, the comparison between models becomes less straightforward. Hence, both models were evaluated against experimental data using RMSE, as depicted in Fig. 4.12. Notably, based on average irradiance levels, Gu model exhibits superior performance at higher irradiances.

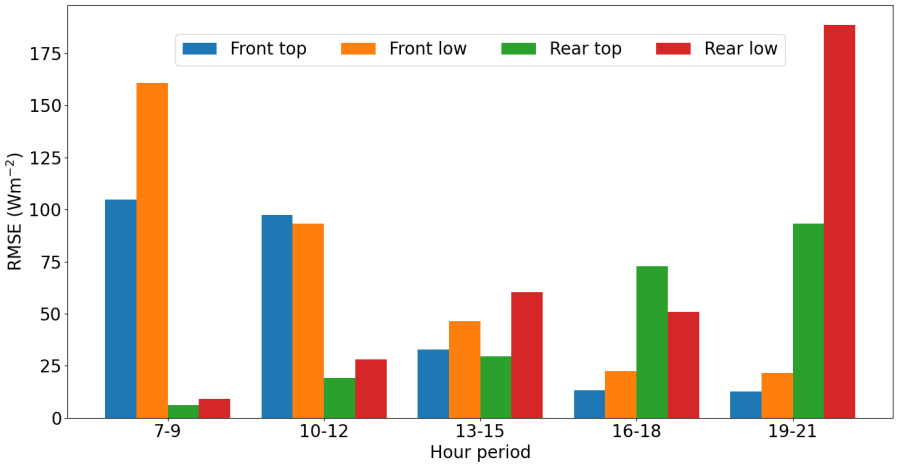

Figure 4.10: RMSE analysis across five time periods each day.

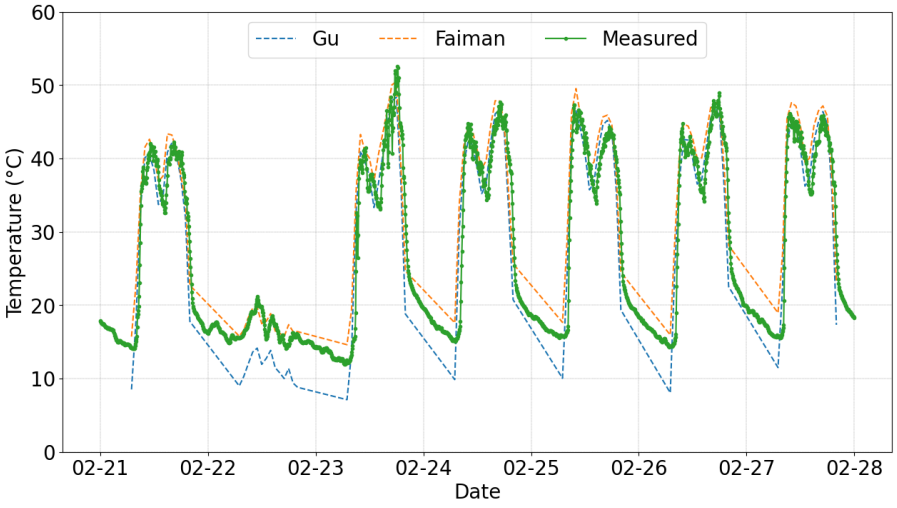

Figure 4.11: Estimated temperatures with Gu and Faiman models.

Since the thermal model utilizes three inputs—ambient temperature, wind speed, and irradiance—the same error analysis performed for irradiance is also conducted for ambient temperature and wind speed, as shown in Figs. 4.13 and 4.14. For ambient temperature, the dependence of RMSE seems to be significant, similar to the results observed with irradiance. However, wind speed does not show a clear correlation with RMSE based on the presented models and is therefore excluded from further analysis.

To determine which variable should be used in the model, a cut-off value for irradiance and temperature is calculated, and for each, the cumulative squared error is obtained. The results show a squared cumulative error of 4532.23 when using irradiance, 6049.04 when using temperature, and 6795.93 when using wind speed. Clearly, the best results are obtained when the cut-off value is applied to irradiance.

Given Gu's superior performance under higher irradiances and Faiman's effectiveness under lower irradiances, a hybrid model is proposed that combines their strengths, as defined in Eq. (4.26).

$$T_{\text{mod}} = \begin{cases} T_{\text{Faiman}}, & \text{if } G_{\text{POA}} < 350 \text{ Wm}^{-2} \\ T_{\text{Gu}}, & \text{if } G_{\text{POA}} \geq 350 \text{ Wm}^{-2} \end{cases} \tag{4.26}$$

The resulting temperatures adjusted accordingly are illustrated in Fig. 4.15.

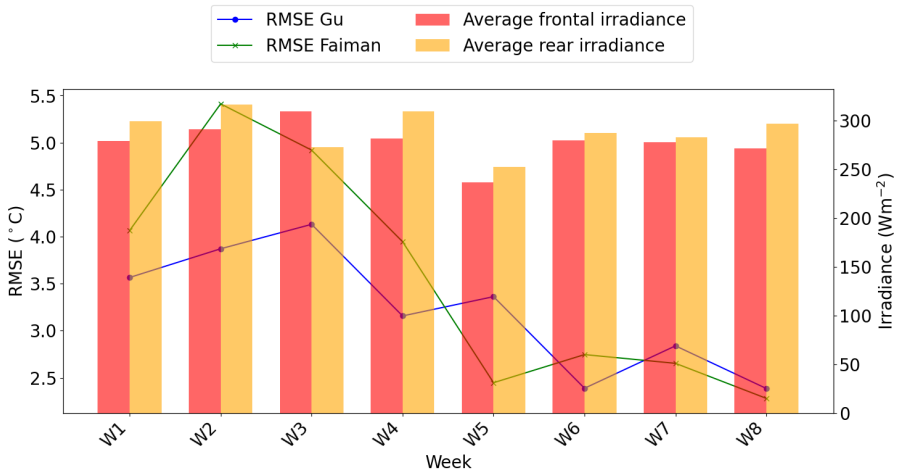

Figure 4.12: Relation between weekly RMSE for thermal model and irradiances.

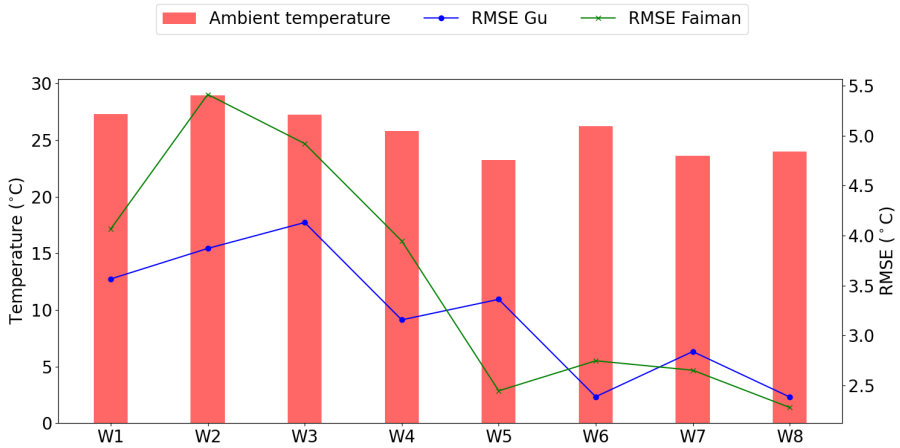

Figure 4.13: Relation between weekly RMSE for thermal model and ambient temperatures.

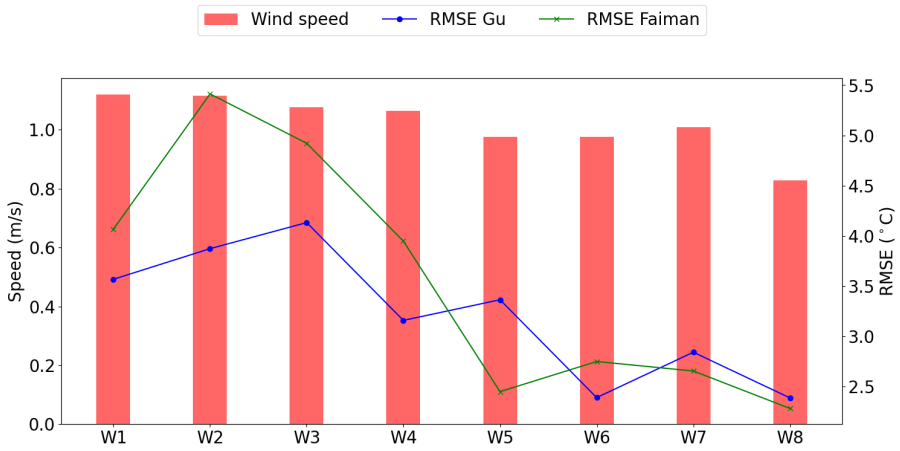

Figure 4.14: Relation between weekly RMSE for thermal model and wind speed.

The application of the hybrid model significantly improves the precision of both high and low estimated temperatures compared to experimental data, and allow to estimate at with the minimum RMSE value, as seen in

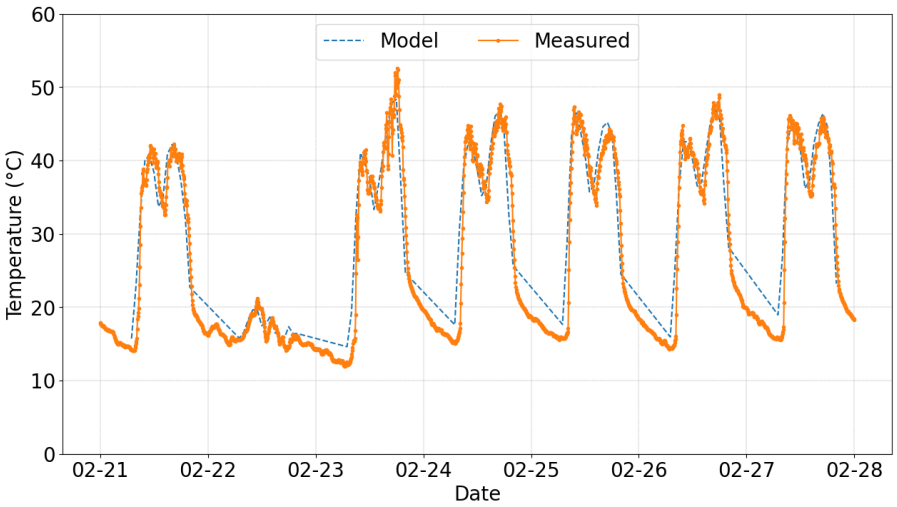

Figure 4.15: Estimated temperatures applying Gu and Faiman models with proposed irradiance criteria.

Fig. 4.10, where the worst case is 4.13°C in the third week using Gu thermal model.

4.5.3 Electrical model

The electrical model is evaluated using two sets of data: the first consists of direct IV curves traced using a sun simulator, while the second involves continuous monitoring of power output.

4.5.3.a Indoor IV curves

Each module listed in Table 4.1 undergoes four parameter estimations: separately for the front and rear sides, for the bifacial configuration, and according to the proposed model. The first three cases involve direct evaluation of experimental IV curves to extract their five SDM parameters. In contrast, the proposed model uses Eqs. (4.19) to (4.23) to estimate equivalent parameters, as detailed in Table 4.2.

Applying the calculated parameters for bifacial direct extraction and the proposed model, IV curves were generated and compared with experimental IV curves, as shown in Figs. 4.16 to 4.18. Analysis of the percent error reveals a slight step in both IV curves due to partial shadowing from frames and junction boxes at the rear of the module. This behavior tends to slightly underestimate the maximum power point, with errors not exceeding 3%. In the open-circuit voltage region, the difference between modeled and experimental values is also minor, with a maximum error of 6%. This is noteworthy considering the steepness of this region, where errors could easily escalate. The SunPower module exhibits the highest error, yet the modeled value approaches zero at the maximum power point.

At this stage, decisions regarding the model's application are crucial. Since the goal of modeling is to estimate module or array production accurately, precise estimation of the maximum power point is important. In this context, all cases demonstrate good performance at this critical point.

4.5.3.b Outdoor power output monitoring

Once the irradiance and thermal models are properly configured, the proposed electrical model utilizes the calculated inputs of irradiance and temperature to predict power output, as illustrated in Fig. 4.19.

The selected dates for demonstration coincide with those used for the irradiance and thermal models, ensuring evaluation during rainy days with low irradiances.

Table 4.2: Estimated parameters for each side of modules at STC conditions, the direct estimation with real IV curve and obtained parameters applying the proposed electrical model.

		I_{ph} (A)	I_o (A)	R_s (Ω)	R_{sh} (Ω)	n (-)
Risen	Frontal side	9.791	9.832e-07	0.1452	inf	1.614
	Rear side	6.537	9.772e-07	0.0000	503.610	1.631
	Bifacial	10.594	8.984e-07	0.1415	inf	1.617
	Proposed	10.635	9.576e-07	0.1452	inf	1.616
SunPower	Frontal side	14.756	1.188e-06	0.0134	inf	1.431
	Rear side	9.526	8.744e-06	0.0000	23.864	1.440
	Bifacial	15.543	1.234e-06	0.0200	inf	1.430
	Proposed	15.594	1.163e-06	0.0133	inf	1.432
Trina	Frontal side	12.102	8.667e-08	0.0746	inf	1.499
	Rear side	8.471	9.017e-08	0.0922	inf	1.501
	Bifacial	12.979	8.508e-08	0.0601	inf	1.500
	Proposed	12.810	8.338e-08	0.0822	inf	1.500

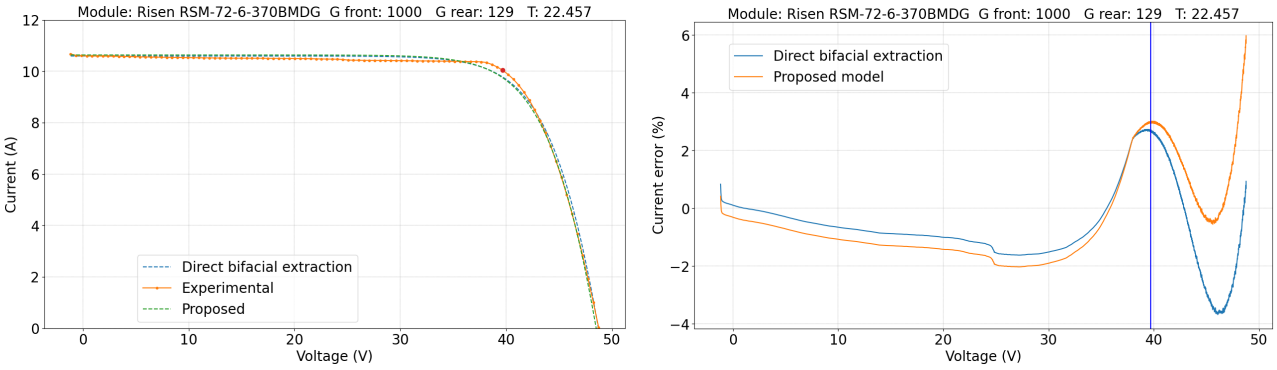

Figure 4.16: (left) IV curves traced in indoor sun simulator, SDM using direct parameter extraction and proposed model for Risen module and (right) percent error for direct parameter extraction and proposed model compared with experimental data. In both cases the maximum power point is indicated.

To see the principal differences between real data and the model, a close up is made in February 27th, as seen in Fig. 4.20

Different behaviors are observed depending on the time of day when the curves are compared. This pattern, as shown in Fig. 4.19, occurs consistently across all days of the week. Therefore, the day is divided into five periods, and the RMSE is evaluated for each period across all the data.

From Fig. 4.10 a pattern can be seen for the first period, from 7 to 9 am. Considering the main error in irradiance estimation, it is coherent that the error appears in the power estimation. However, the periods from 13-15 and 16-18 do not have high errors compared to the irradiance estimation behavior. Due to the composition of the rear side of the module, shadows cast by the frame occur from midday to evening, significantly reducing the effective irradiance reaching the module and thereby limiting power production.

Finally, to avoid the effect of estimation errors, direct measurements of irradiance and temperature are used as inputs, replacing the previously estimated data. This results in the estimated maximum power output depicted in Fig. 4.22. Compared to the previous power estimation, the power in the morning is estimated more accurately,

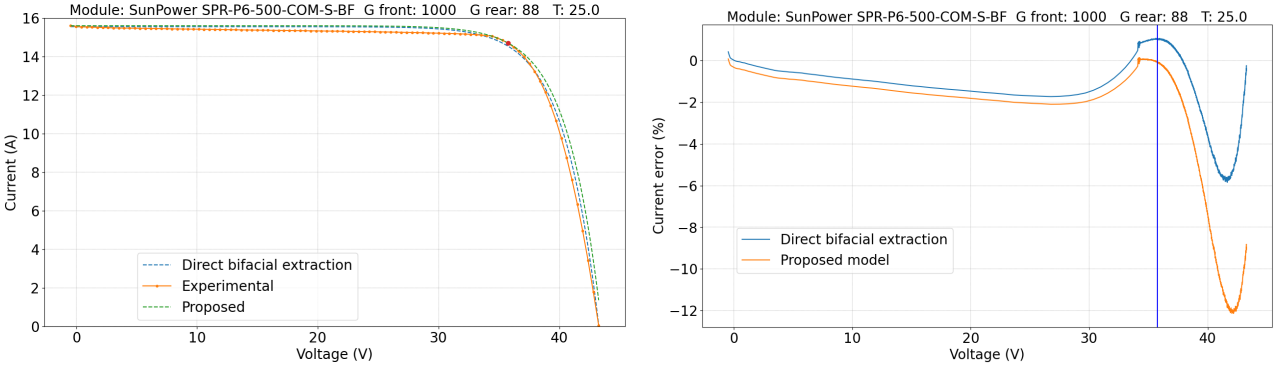

Figure 4.17: (left) IV curves traced in indoor sun simulator, SDM using direct parameter extraction and proposed model for SunPower module and (right) percent error for direct parameter extraction and proposed model compared with experimental data. In both cases the maximum power point is indicated.

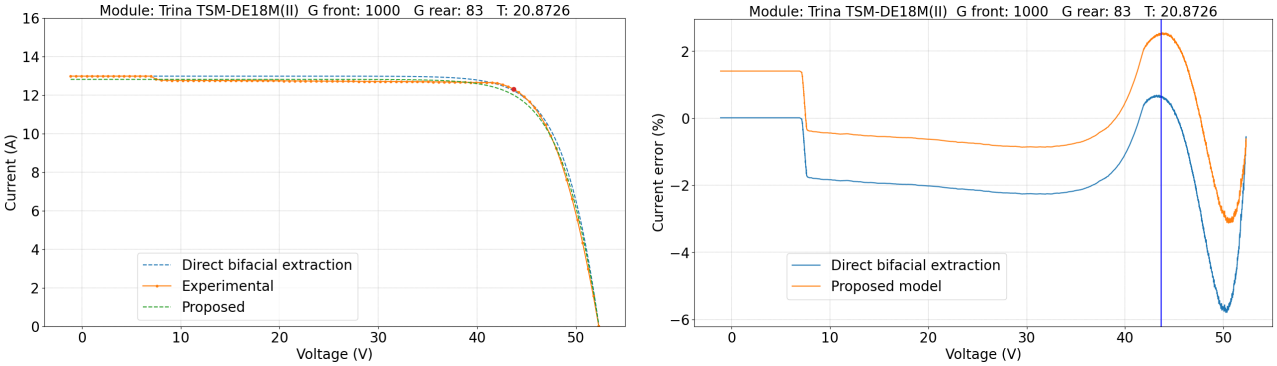

Figure 4.18: (left) IV curves traced in indoor sun simulator, SDM using direct parameter extraction and proposed model for Trina module and (right) percent error for direct parameter extraction and proposed model compared with experimental data. In both cases the maximum power point is indicated.

as evidenced by Fig. 4.23, which shows a decrease in error during the early hours of the day. However, the error in the evening often exceeds the error during the rest of the day, just as it happened before, indicating a behavior related to framing and shadowing effects.

4.6 Conclusions

A methodology for implementing an electrical-thermal model was proposed. This methodology involves using Bifacial Radiance software for estimating irradiances, developing a hybrid thermal model based on two existing literature models, and proposing a new method for bifacial parameter estimation to derive IV curves. With estimated irradiances and temperatures, the electrical model was used to predict power output in a real outdoor configuration.

To evaluate the performance of each estimation, an error analysis was conducted. It was found that the irradiance estimation tends to underestimate the actual values. Therefore, based on empirical data, two correction factors were determined and applied to all data series, even at lower irradiances.

Regarding the thermal model, it was observed that the Gu thermal model performs well under high irradiances but encounters challenges at lower levels. This led to its integration with the Faiman model to form a hybrid

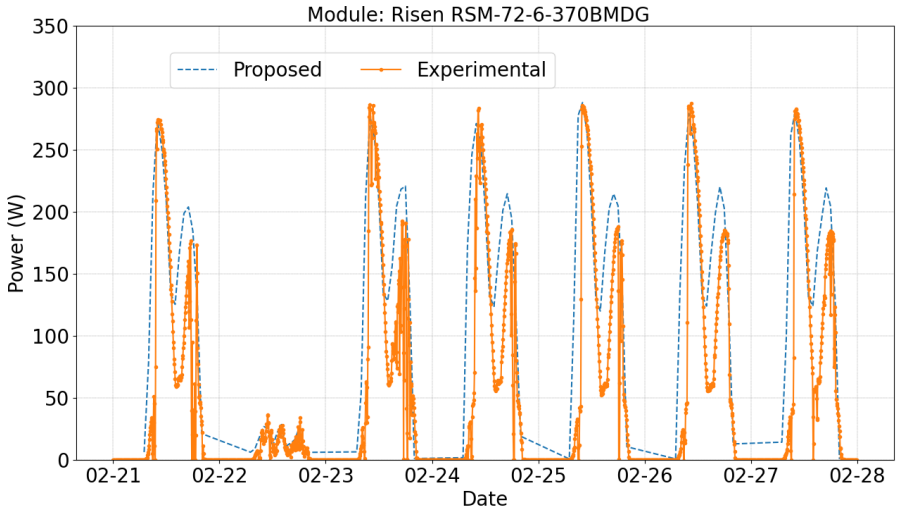

Figure 4.19: Estimated maximum power output applying the proposed model and with estimated irradiances and temperatures as input. The estimation is compared with the real measured power output.

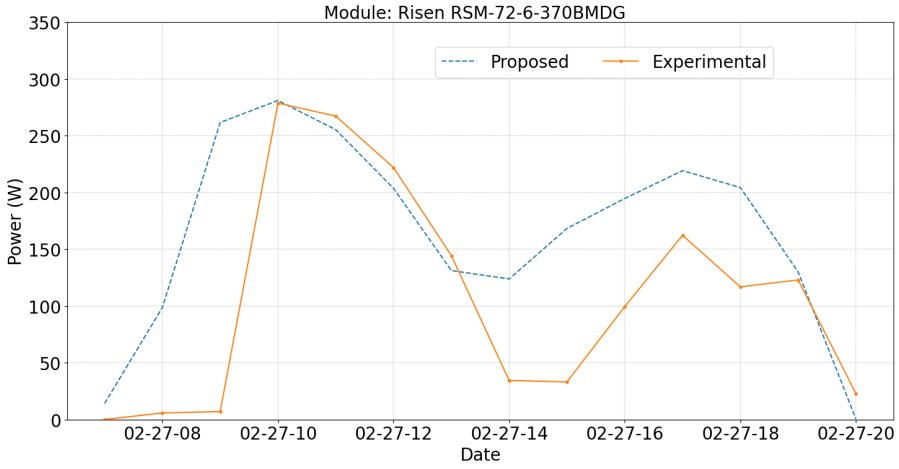

Figure 4.20: Estimated maximum power output for February 27th.

approach. This integration identified an optimal irradiance value of 260 Wm^{-2}, where Faiman model exhibits superior performance. A cumulative squared error analysis revealed that ambient temperature and wind speed do not reduce the error as effectively as irradiance, with the cumulative squared error being 4532.23.

The proposed electrical model demonstrated outstanding accuracy in indoor measurements, with maximum current errors of approximately 3% at the maximum power point, a critical value for outdoor evaluations. However, in real outdoor conditions, various phenomena significantly affect results, including reflections, clouds, and notably, shadows cast by the module frames on the rear side. This effect was confirmed when directly measured irradiances and temperatures were used as input in the electrical model, where the error in power estimation increased during the evenings. This behavior leads to the conclusion that the vertical orientation of the module amplifies the frame's effect.

The proposed model includes three estimations: irradiance, temperature, and power. Irradiance is solely dependent on measured values of ambient conditions, while temperature is influenced by irradiance, ambient temperature, and wind speed. This dependency on irradiance conditions the model, as the estimated irradiance has an hourly resolution. Consequently, the electrical model, which relies on both irradiance and temperature,

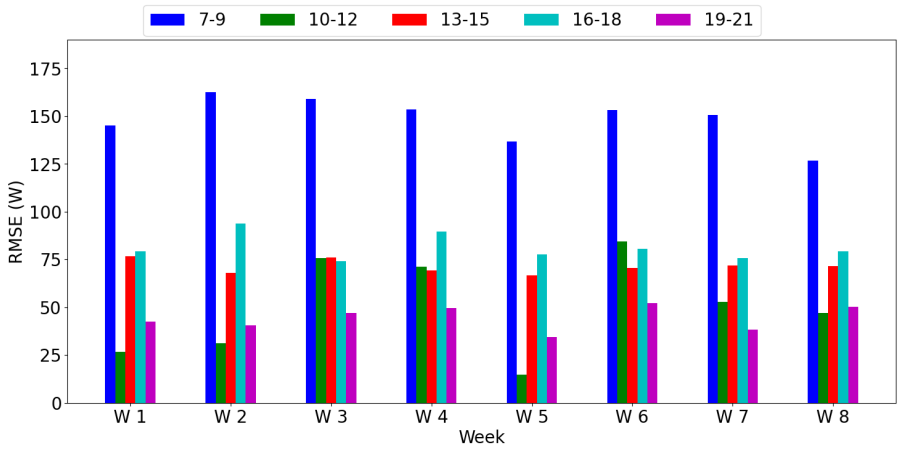

Figure 4.21: RMSE for power estimation in each defined period.

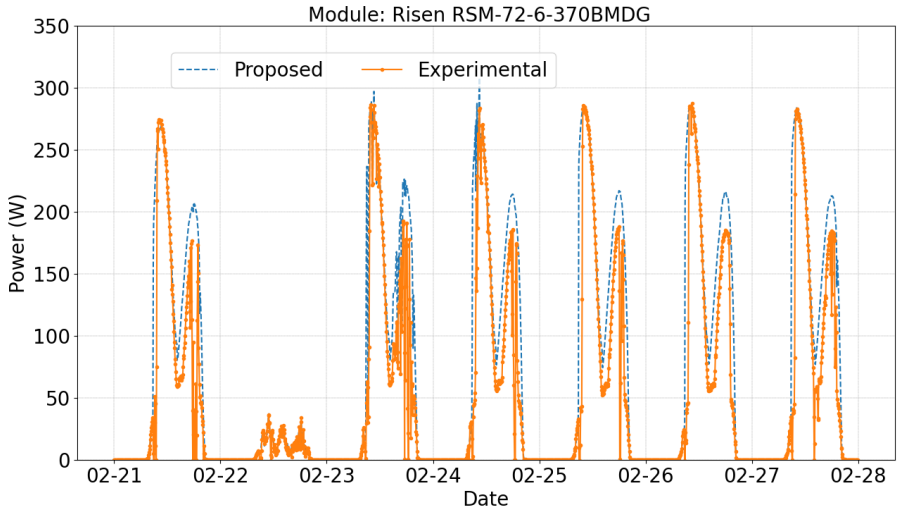

Figure 4.22: Estimated maximum power output applying the proposed model and with measured irradiances and temperatures as input. The estimation is compared with the real measured power output.

also produces power output with an hourly resolution.

This resolution is adequate for estimating peak hours of production but is insufficient for capturing short-term events, such as those occurring on a minute-by-minute basis. Additionally, the model cannot account for certain effects, like shadows during the morning or evening, leading to RMSE values reaching up to 170W in the worst cases.

It is recommended to adjust the model to the specific location, taking into account the effects of buildings and local geography for better results. When the electrical model is applied to the measured irradiance and temperature conditions, the errors are more uniform. The peak production during the morning is well represented, with typical RMSE values around 10-30W for most weeks. The worst case occurred in the 6th week, reaching 75W. In contrast, the evenings consistently show RMSE values exceeding 50W during peak production, an effect attributable to shadowing on the rear side of the module.

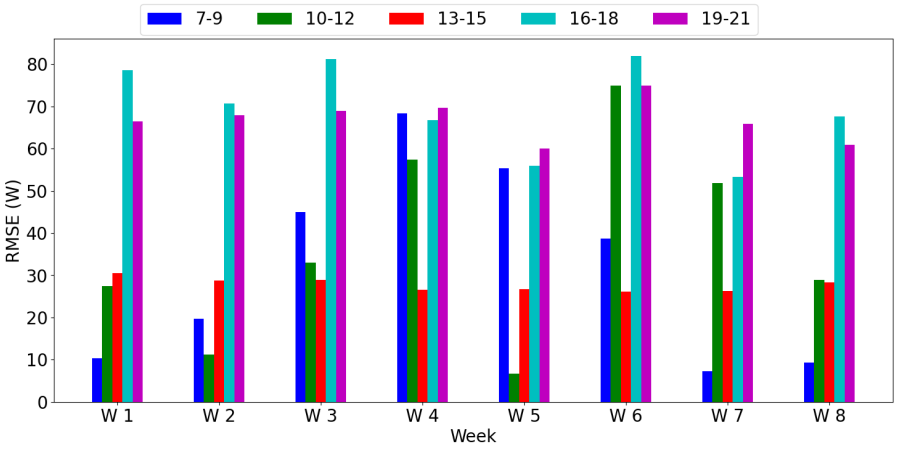

Figure 4.23: RMSE for power estimation in each defined period when measured temperatures and irradiances are used as input.

Chapter 5

General conclusions

The proposed electrical-thermal model for bifacial photovoltaic (bPV) modules followed a structured approach to address the significant research gap in bifacial electrical and thermal modeling. A thorough review of existing literature underscored the insufficient validation methods typically relying on simulations or continuous monitoring data without direct IV curve validation. This review also identified promising proposals from other researchers that could be refined for more accurate estimation errors. Additionally, the review emphasized the importance of characterization, measurement, and validation in the modeling process, as these steps provide critical parameters for subsequent analysis.

The literature review revealed that several electrical characterization methods involve single-sided measurements with the the other side covered. However, some setups illuminate both sides using arrangements that reflect light onto the rear side of the module. Both approaches were employed to obtain IV curves for different analytical purposes and were applied to indoor IV characterization using the TCLF sun simulator.

Single-sided measurements were conducted in a closed cabin to prevent light reflection and rear-side illumination. In contrast, double-sided measurements utilized a raised cabin with reflective paper on the rear side of the module. This method was evaluated by measuring irradiance at various locations on the module's rear side, revealing significant irradiance non-uniformity. Due to the variable irradiance levels observed, it was proposed to use the minimum value because of its dependence on I_{sc}.

Based on the state of the art, two methods were employed to obtain IV curves under controlled indoor conditions. The first method involved single-sided measurements with the other side covered. These measurements allowed for the separate analysis of each side's IV curve, revealing that frames and junction boxes often cause shadowing, which introduces steps in the IV curve. This phenomenon also affects electrical parameters such as V_{oc}; when frame shadowing is more evident, a reduction in this parameters is observed in the rear side IV curve. These single-sided measurements were crucial for extracting key parameters necessary for model estimation, including I_{sc}, V_{oc}, I_{mpp}, and V_{mpp}. Using these experimentally derived parameters significantly minimized estimation errors, offering a more accurate representation than relying solely on datasheet values during the subsequent model evaluation.

The second method involved double-sided measurements, which provided insights into the module's response to light exposure when both sides are illuminated. As expected, this approach increased I_{sc} levels compared to single-sided illumination and also presented the steps previously observed in the rear side's IV curve.

Evaluation of literature models were applied to the IV curves of both types of data, from single and double sided illumination. For double sided illumination, the single diode model proposed by Gu *et al.* performed most effectively for all the studied modules, with current errors near to 20% in the worst case, whereas the parallel single diode model proposed by Bhang *et al.* exhibited poorer performance, reaching errors reaching 140% in the worst case, showing that this model can not estimate maximum power point or V_{oc} correctly. The double diode model by Janssen *et al.* showed challenges in accurate estimation, particularly affecting the open circuit voltage estimation. The principal issues with this method are the forcing of some parameters as ideality coefficients.

Based on insights from Gu and Janssen's electrical model proposals, an approximation was developed that integrated Janssen's rescaling concept with Gu's correction to the diode saturation current. This hybrid model was applied to indoor IV curves under double-sided illumination and an outdoor arrangement consisting of a vertical bPV module with an east-west orientation.

Hybrid thermal models were also proposed and applied in the context of continuous outdoor monitoring. These models combine the strengths of two existing models to address varying irradiance levels. Specifically, the integration of Gu and Faiman models showed that Gu's model was more effective under irradiances exceeding 260 W/m^2.

Additionally, irradiance estimation was performed using Bifacial Radiance software, which was evaluated with outdoor data using meteorological inputs. Error analysis revealed issues with irradiance estimation during morning and evening hours, likely due to shadowing effects impacting the installation. This, in turn, affected electrical estimations during continuous monitoring.

When the electrical model was evaluated solely with measured data, higher estimation errors were observed after midday, indicating that the effect of frame shadowing significantly impacts power production. This comprehensive analysis underscores the importance of accounting for various environmental and structural factors to improve the accuracy of bPV module performance models.

Bibliography

[1] P. Valdivia Lefort, V. Gonzalez, and R. Barraza. "Characterization of the Electrical Behavior of Bifacial Photovoltaic Solar Modules Obtained Through Static And Transient Analyses". In: *AIP Conference Proceedings - 8th World Conference on Photovoltaic Energy Conversion*. 2022, pp. 462–469. DOI: 10.4229/WCPEC-82022-2BV.2.59.

[2] Izumi Kaizuka Gaëtan Masson. *PVPS 2022: Trends in Photovoltaic Applications*. IEA, 2022.

[3] *Reporte Anual de Desempeño del SEN (Art. 72°-15)*. Coordinador Eléctrico Nacional, 2021. URL: https://www.coordinador.cl/reportes/documentos/reporte-anual-de-desempeno-del-sen/.

[4] Ministerio de Energía. *Explorador Solar*. URL: https://solar.minenergia.cl/inicio.

[5] Shashwata Chattopadhyay et al. "Visual Degradation in Field-Aged Crystalline Silicon PV Modules in India and Correlation With Electrical Degradation". In: *IEEE Journal of Photovoltaics* 4.6 (2014), pp. 1470–1476. DOI: 10.1109/JPHOTOV.2014.2356717.

[6] M.A. Quintana et al. "Commonly observed degradation in field-aged photovoltaic modules". In: *Conference Record of the Twenty-Ninth IEEE Photovoltaic Specialists Conference, 2002.* 2002, pp. 1436–1439. DOI: 10.1109/PVSC.2002.1190879.

[7] *High Performance Monocrystalline PERC Module*. RSM72-6-360M-380M. Risen. 2019.

[8] *Standard Tables for Reference Solar Spectral Irradiances*. Standard. ASTM International, 2020.

[9] *Photovoltaic (PV) systems - Requirements for testing, documentation and maintenance - Part 1: Grid connected systems - Documentation, commissioning tests and inspection*. Standard. International Electrotechnical Commission, 2016.

[10] *Photovoltaic devices - Part 13: Electroluminescence of photovoltaic modules*. Standard. International Electrotechnical Commission, 2018.

[11] Elmehdi Mouhib et al. "Overview of the Fundamentals and Applications of Bifacial Photovoltaic Technology: Agrivoltaics and Aquavoltaics". In: *Energies* 15.23 (2022). ISSN: 1996-1073. DOI: 10.3390/en15238777. URL: https://www.mdpi.com/1996-1073/15/23/8777.

[12] A. Cuevas et al. "50 Per cent more output power from an albedo-collecting flat panel using bifacial solar cells". In: *Solar Energy* 29.5 (1982), pp. 419–420. ISSN: 0038-092X. DOI: https://doi.org/10.1016/0038-092X(82)90078-0. URL: https://www.sciencedirect.com/science/article/pii/0038092X82900780.

[13] Naftali Paul Eisenberg et al. "Experimental Analysis of the Increases in Energy Generation of Bifacial Over Mono-Facial PV Modules". In: 2011. URL: https://api.semanticscholar.org/CorpusID:111056678.

[14] Giuseppe Marco Tina et al. "Comparative analysis of monofacial and bifacial photovoltaic modules for floating power plants". In: *Applied Energy* 281 (2021), p. 116084. ISSN: 0306-2619. DOI: https://doi.org/10.1016/j.apenergy.2020.116084. URL: https://www.sciencedirect.com/science/article/pii/S0306261920315117.

[15] Carlos D. Rodríguez-Gallegos et al. "Monofacial vs bifacial Si-based PV modules: Which one is more cost-effective?" In: *Solar Energy* 176 (2018), pp. 412–438. ISSN: 0038-092X. DOI: https://doi.org/10.1016/j.solener.2018.10.012. URL: https://www.sciencedirect.com/science/article/pii/S0038092X18309915.

[16] Furqan Tahir, Ahmer A.B. Baloch, and Sami G. Al-Ghamdi. "Impact of climate change on solar monofacial and bifacial Photovoltaics (PV) potential in Qatar". In: *Energy Reports* 8 (2022). ICPE 2021 - The 2nd International Conference on Power Engineering, pp. 518–522. ISSN: 2352-4847. DOI: https://doi.org/10.1016/j.egyr.2022.02.197. URL: https://www.sciencedirect.com/science/article/pii/S2352484722004449.

[17] Abdelkader Abbassi et al. "Improved Arithmetic Optimization Algorithm for Parameters Extraction of Photovoltaic Solar Cell Single-Diode Model". In: *Arabian Journal for Science and Engineering* 47 (2022), pp. 10435–10451. ISSN: 2191-4281. DOI: 10.1007/s13369-022-06605-y. URL: https://link.springer.com/article/10.1007/s13369-022-06605-y.

[18] Shigeomi Hara. "Parameter Extraction of Single-Diode Model From Module Datasheet Information Using Temperature Coefficients". In: *IEEE Journal of Photovoltaics* 11.1 (2021), pp. 213–218. DOI: 10.1109/JPHOTOV.2020.3035116.

[19] M. Piliougine et al. "Parameters extraction of single diode model for degraded photovoltaic modules". In: *Renewable Energy* 164 (2021), pp. 674–686. ISSN: 0960-1481. DOI: https://doi.org/10.1016/j.renene.2020.09.035. URL: https://www.sciencedirect.com/science/article/pii/S0960148120314555.

[20] Mohammed Rasheed, Osama Alabdali, and Suha Shihab. "A New Technique for Solar Cell Parameters Estimation of The Single-Diode Model". In: *Journal of Physics: Conference Series* 1879.3 (2021), p. 032120. DOI: 10.1088/1742-6596/1879/3/032120. URL: https://dx.doi.org/10.1088/1742-6596/1879/3/032120.

[21] Mohammed Rasheed et al. "Parameters Extraction of a Single-Diode Model of Photovoltaic Cell Using False Position Iterative Method". In: *Journal of Physics: Conference Series* 1879.3 (2021), p. 032113. DOI: 10.1088/1742-6596/1879/3/032113. URL: https://dx.doi.org/10.1088/1742-6596/1879/3/032113.

[22] Zhaoxu Song et al. "An Effective Method to Accurately Extract the Parameters of Single Diode Model of Solar Cells". In: *Nanomaterials* 11.10 (2021). ISSN: 2079-4991. DOI: 10.3390/nano11102615. URL: https://www.mdpi.com/2079-4991/11/10/2615.

[23] Giovanni Petrone, Carlos Andres Ramos-Paja, and Giovanni Spagnuolo. *Photovoltaic Sources Modeling*. Wiley & Sons, 2017.

[24] Gautam Raina and Sunanda Sinha. "A holistic review approach of design considerations, modelling, challenges and future applications for bifacial photovoltaics". In: *Energy Conversion and Management* 271 (2022), p. 116290. ISSN: 0196-8904. DOI: https://doi.org/10.1016/j.enconman.2022.116290. URL: https://www.sciencedirect.com/science/article/pii/S0196890422010676.

[25] J. Louw. "Modelling and simulation of bifacial PV modules by implementing the ray tracing technique". Available at https://scholar.sun.ac.za/items/54d3a241-43d1-4654-a4ce-94a7603d132a. Master's thesis. Stellenboch: Stellenboch University, 2020.

[26] Wenbo Gu et al. "A coupled optical-electrical-thermal model of the bifacial photovoltaic module". In: *Applied Energy* 258 (2020), p. 114075. ISSN: 0306-2619. DOI: https://doi.org/10.1016/j.apenergy.2019.114075. URL: https://www.sciencedirect.com/science/article/pii/S0306261919317623.

[27] Byeong Gwan Bhang et al. "Power Performance of Bifacial c-Si PV Modules With Different Shading Ratios". In: *IEEE Journal of Photovoltaics* 9.5 (2019), pp. 1413–1420. DOI: 10.1109/JPHOTOV.2019.2928461.

[28] Silvano Vergura. "Simulink model of a bifacial PV module based on the manufacturer datasheet". In: *Renewable Energy and Power Quality Journal* 18 (June 2020), pp. 637–641. DOI: 10.24084/repqj18.456.

[29] Abdelkader Abbassi et al. "Parameterization of photovoltaic solar cell double-diode model based on improved arithmetic optimization algorithm". In: *Optik* 253 (2022), p. 168600. ISSN: 0030-4026. DOI: https://doi.org/10.1016/j.ijleo.2022.168600. URL: https://www.sciencedirect.com/science/article/pii/S0030402622000286.

[30] Mohammad Hejri et al. "On the Parameter Extraction of a Five-Parameter Double-Diode Model of Photovoltaic Cells and Modules". In: *IEEE Journal of Photovoltaics* 4.3 (2014), pp. 915–923. DOI: 10.1109/JPHOTOV.2014.2307161.

[31] Silvano Ortiz et al. "Evaluación del desempeño de los modelos de un diodo y dos diodos para módulos fotovoltaicos". In: *Revista Espacios* 41 (Sept. 2020), pp. 152–170. ISSN: 0798-1015.

[32] Nahla Mohamed Abd Alrahim Shannan, Nor Zaihar Yahaya, and Balbir Singh. "Single-diode model and two-diode model of PV modules: A comparison". In: *2013 IEEE International Conference on Control System, Computing and Engineering*. 2013, pp. 210–214. DOI: 10.1109/ICCSCE.2013.6719960.

[33] Gaby Janssen et al. "Outdoor Performance of Bifacial Modules by Measurements and Modelling". In: *Energy Procedia* 77 (Aug. 2015), pp. 364–373. DOI: 10.1016/j.egypro.2015.07.051.

[34] Emad M. Ahmed et al. "An Accurate Model for Bifacial Photovoltaic Panels". In: *Sustainability* 15.1 (2023). ISSN: 2071-1050. DOI: 10.3390/su15010509. URL: https://www.mdpi.com/2071-1050/15/1/509.

[35] Salim Bouchakour et al. "Modelling and Simulation of Bifacial PV Production Using Monofacial Electrical Models". In: *Energies* 14.14 (2021). ISSN: 1996-1073. DOI: 10.3390/en14144224. URL: https://www.mdpi.com/1996-1073/14/14/4224.

[36] Eduardo Ortiz-Rivera and Fang Peng. "Analytical Model for a Photovoltaic Module using the Electrical Characteristics provided by the Manufacturer Data Sheet". In: vol. 2005. July 2005, pp. 2087–2091. DOI: 10.1109/PESC.2005.1581920.

[37] D King, J Kratochvil, and W Boyson. "Photovoltaic Array Performance Model". PhD thesis. Jan. 2004. DOI: 10.2172/919131.

[38] N. Lindsay et al. "Errors in PV power modelling due to the lack of spectral and angular details of solar irradiance inputs". In: *Solar Energy* 197 (2020), pp. 266–278. ISSN: 0038-092X. DOI: https://doi.org/10.1016/j.solener.2019.12.042. URL: https://www.sciencedirect.com/science/article/pii/S0038092X19312563.

[39] J. Antonanzas et al. "Review of photovoltaic power forecasting". In: *Solar Energy* 136 (2016), pp. 78–111. ISSN: 0038-092X. DOI: https://doi.org/10.1016/j.solener.2016.06.069. URL: https://www.sciencedirect.com/science/article/pii/S0038092X1630250X.

[40] Tian Shen Liang et al. “A review of crystalline silicon bifacial photovoltaic performance characterisation and simulation”. In: *Energy Environ. Sci.* 12 (1 2019), pp. 116–148. DOI: 10.1039/C8EE02184H. URL: http://dx.doi.org/10.1039/C8EE02184H.

[41] *Photovoltaic devices - Part 1-2: Measurement of current-voltage characteristics of bifacial photovoltaic (PV) devices*. en. Technical Specification. International Electrotechnical Commision, 2019. URL: https://webstore.iec.ch/publication/34357.

[42] Tian Shen Liang, Daren Poh, and Mauro Pravettoni. “Challenges in the pre-normative characterization of bifacial photovoltaic modules”. In: *Energy Procedia* 150 (2018). Proceedings of the 12th International Photovoltaic Power Generation and Smart Energy Conference & Exhibition (SNEC2018), pp. 66–73. ISSN: 1876-6102. DOI: https://doi.org/10.1016/j.egypro.2018.09.006. URL: https://www.sciencedirect.com/science/article/pii/S1876610218305460.

[43] Guillaume Razongles et al. “Bifacial Photovoltaic Modules: Measurement Challenges”. In: *Energy Procedia* 92 (2016). Proceedings of the 6th International Conference on Crystalline Silicon Photovoltaics (SiliconPV 2016), pp. 188–198. ISSN: 1876-6102. DOI: 10.1016/j.egypro.2016.07.056. URL: https://www.sciencedirect.com/science/article/pii/S1876610216304830.

[44] AR Lagunas et al. “Design of a Special Set-Up for the I-V Characterization of Bifacial Photovoltaic Solar Cells”. In: 2008. DOI: 10.4229/23rdEUPVSEC2008-2CV.4.67.

[45] Yating Zhang et al. “Comparison of Double-Side and Equivalent Single-Side Illumination Methods for Measuring the I–V Characteristics of Bifacial Photovoltaic Devices”. In: *IEEE Journal of Photovoltaics* 8 (Mar. 2018), pp. 1–7. DOI: 10.1109/JPHOTOV.2017.2778226.

[46] B. Chitti Babu and Suresh Gurjar. “A Novel Simplified Two-Diode Model of Photovoltaic (PV) Module”. In: *IEEE Journal of Photovoltaics* 4.4 (2014), pp. 1156–1161. DOI: 10.1109/JPHOTOV.2014.2316371.

[47] Gautam Raina and Sunanda Sinha. “A comprehensive assessment of electrical performance and mismatch losses in bifacial PV module under different front and rear side shading scenarios”. In: *Energy Conversion and Management* 261 (2022), p. 115668. ISSN: 0196-8904. DOI: https://doi.org/10.1016/j.enconman.2022.115668. URL: https://www.sciencedirect.com/science/article/pii/S0196890422004642.

[48] Marzia Alam, Mehreen Saleem Gul, and Tariq Muneer. “Performance analysis and comparison between bifacial and monofacial solar photovoltaic at various ground albedo conditions”. In: *Renewable Energy Focus* 44 (2023), pp. 295–316. ISSN: 1755-0084. DOI: https://doi.org/10.1016/j.ref.2023.01.005. URL: https://www.sciencedirect.com/science/article/pii/S1755008423000066.

[49] Jianmei Zhong et al. “Development and challenges of bifacial photovoltaic technology and application in buildings: A review”. In: *Renewable and Sustainable Energy Reviews* 187 (2023), p. 113706. ISSN: 1364-0321. DOI: https://doi.org/10.1016/j.rser.2023.113706. URL: https://www.sciencedirect.com/science/article/pii/S1364032123005634.

[50] Ahmer A.B. Baloch et al. “In-field characterization of key performance parameters for bifacial photovoltaic installation in a desert climate”. In: *Renewable Energy* 159 (2020), pp. 50–63. ISSN: 0960-1481. DOI: https://doi.org/10.1016/j.renene.2020.05.174. URL: https://www.sciencedirect.com/science/article/pii/S096014812030879X.

[51] Gautam Raina, Rohit Vijay, and Sunanda Sinha. "Study on the optimum orientation of bifacial photovoltaic module". In: *International Journal of Energy Research* 46.4 (2022), pp. 4247–4266. DOI: https://doi.org/10.1002/er.7423. eprint: https://onlinelibrary.wiley.com/doi/pdf/10.1002/er.7423. URL: https://onlinelibrary.wiley.com/doi/abs/10.1002/er.7423.

[52] Stanley Wang et al. "Bifacial Photovoltaic Systems Energy Yield Modelling". In: *Energy Procedia* 77 (2015). 5th International Conference on Silicon Photovoltaics, SiliconPV 2015, pp. 428–433. ISSN: 1876-6102. DOI: https://doi.org/10.1016/j.egypro.2015.07.060. URL: https://www.sciencedirect.com/science/article/pii/S1876610215008280.

[53] Wei Lu. "Power generation characteristics of bifacial photovoltaic modules under different backgrounds". In: *2021 IEEE International Conference on Artificial Intelligence and Computer Applications (ICAICA)*. 2021, pp. 470–473. DOI: 10.1109/ICAICA52286.2021.9498001.

[54] Joshua S. Stein et al. "Outdoor Field Performance from Bifacial Photovoltaic Modules and Systems". In: *2017 IEEE 44th Photovoltaic Specialist Conference (PVSC)*. 2017, pp. 3184–3189. DOI: 10.1109/PVSC.2017.8366042.

[55] Wenbo Gu et al. "Experimental investigation of the bifacial photovoltaic module under real conditions". en. In: *Renewable Energy* 173 (Aug. 2021), pp. 1111–1122. ISSN: 09601481. DOI: 10.1016/j.renene.2020.12.024. URL: https://linkinghub.elsevier.com/retrieve/pii/S0960148120319509 (visited on 07/17/2023).

[56] Wenbo Gu et al. "A comprehensive review and outlook of bifacial photovoltaic (bPV) technology". In: *Energy Conversion and Management* 223 (2020), p. 113283. ISSN: 0196-8904. DOI: https://doi.org/10.1016/j.enconman.2020.113283. URL: https://www.sciencedirect.com/science/article/pii/S0196890420308220.

[57] Ismail Shoukry et al. "Modelling of Bifacial Gain for Stand-alone and in-field Installed Bifacial PV Modules". In: *Energy Procedia* 92 (2016). Proceedings of the 6th International Conference on Crystalline Silicon Photovoltaics (SiliconPV 2016), pp. 600–608. ISSN: 1876-6102. DOI: https://doi.org/10.1016/j.egypro.2016.07.025. URL: https://www.sciencedirect.com/science/article/pii/S1876610216304520.

[58] Eduardo Lorenzo. "On the historical origins of bifacial PV modelling". In: *Solar Energy* 218 (2021), pp. 587–595. ISSN: 0038-092X. DOI: https://doi.org/10.1016/j.solener.2021.03.006. URL: https://www.sciencedirect.com/science/article/pii/S0038092X21001869.

[59] LBNL. *Radiance*. Version 5.4. May 2023. URL: https://floyd.lbl.gov/radiance/framed.html.

[60] Lambda Research Corporation. *TracePro*. URL: https://lambdares.com/tracepro.

[61] COMSOL. *RayOptics*. URL: https://www.comsol.com/ray-optics-module.

[62] Marco Leonardi et al. "The Effects of Module Temperature on the Energy Yield of Bifacial Photovoltaics: Data and Model". In: *Energies* 15.1 (2022). ISSN: 1996-1073. DOI: 10.3390/en15010022. URL: https://www.mdpi.com/1996-1073/15/1/22.

[63] Shahzada Pamir Aly et al. "A thermal model for bifacial PV panels". In: *2022 IEEE 49th Photovoltaics Specialists Conference (PVSC)*. 2022, pp. 0457–0459. DOI: 10.1109/PVSC48317.2022.9938549.

[64] Oussama Hachana et al. “Photovoltaic mono and bifacial module/string electrical model parameters identification and validation based on a new differential evolution bee colony optimizer”. In: *Energy Conversion and Management* 248 (2021), p. 114667. ISSN: 0196-8904. DOI: https://doi.org/10.1016/j.enconman.2021.114667. URL: https://www.sciencedirect.com/science/article/pii/S0196890421008438.

[65] Th. Katsaounis et al. “Performance assessment of bifacial c-Si PV modules through device simulations and outdoor measurements”. In: *Renewable Energy* 143 (2019), pp. 1285–1298. ISSN: 0960-1481. DOI: https://doi.org/10.1016/j.renene.2019.05.057. URL: https://www.sciencedirect.com/science/article/pii/S0960148119307177.

[66] E. Skoplaki and J.A. Palyvos. “On the temperature dependence of photovoltaic module electrical performance: A review of efficiency/power correlations”. In: *Solar Energy* 83.5 (2009), pp. 614–624. ISSN: 0038-092X. DOI: https://doi.org/10.1016/j.solener.2008.10.008. URL: https://www.sciencedirect.com/science/article/pii/S0038092X08002788.

[67] David Faiman. “Assessing the outdoor operating temperature of photovoltaic modules”. In: *Progress in Photovoltaics: Research and Applications* 16.4 (2008), pp. 307–315. DOI: https://doi.org/10.1002/pip.813. eprint: https://onlinelibrary.wiley.com/doi/pdf/10.1002/pip.813. URL: https://onlinelibrary.wiley.com/doi/abs/10.1002/pip.813.

[68] Francisco Araya Rojas. “Predictive modelling of bifacial PV plants performance and diagnostic”. Theses. Université Grenoble Alpes [2020-....], June 2022. URL: https://theses.hal.science/tel-03828423.

[69] Malte Ruben Vogt et al. “Developing an energy rating for bifacial photovoltaic modules”. In: *Progress in Photovoltaics: Research and Applications* 31.12 (2023), pp. 1466–1477. DOI: https://doi.org/10.1002/pip.3678. eprint: https://onlinelibrary.wiley.com/doi/pdf/10.1002/pip.3678. URL: https://onlinelibrary.wiley.com/doi/abs/10.1002/pip.3678.

[70] Silvana Ayala Pelaez and Chris Deline. “bifacial_radiance: a python package for modeling bifacial solar photovoltaic systems”. In: *Journal of Open Source Software* 5.50 (2020), p. 1865. DOI: 10.21105/joss.01865. URL: https://doi.org/10.21105/joss.01865.

[71] *Photovoltaic system performance. Monitoring*. Standard. International Electrical Commission, Sept. 2021.